Simulating Chemical Dynamics on Analog Quantum Computers

Vanessa Carolina Olaya Agudelo

A thesis submitted to fulfill requirements for the degree of

Doctor of Philosophy

The University of Sydney

School of Chemistry

2026

Abstract

Accurately simulating the evolution of molecules during chemical reactions is one of the most enduring challenges in computational chemistry. These processes are inherently quantum mechanical: they involve the coupled dynamics of electronic states and nuclear motion leading to non-adiabatic effects. Capturing such effects exactly requires a fully quantum treatment, yet the computational cost of these simulations can scale exponentially with system size. Even with state-of-the-art supercomputers, the storage of a molecular wavefunction can become intractable for large systems, limiting our ability to explore fully quantum chemical dynamics.

Quantum simulation offers a promising route to overcome this bottleneck by using controllable quantum systems to directly reproduce the dynamics of molecular processes. However, the leading approach—digital quantum computing with qubits and gates—remains far from practical utility in this context. Current devices are limited in qubit number, coherence times, and gate fidelities, all of which prevent the simulation of even modestly sized molecular systems. As a result, fully digital approaches are unlikely to deliver near-term advances for problems in quantum chemistry. This motivates the exploration of alternative architectures that can harness quantum resources more efficiently.

In this thesis, we demonstrate how mixed-qudit-boson (MQB) quantum simulators provide a practical and resource-efficient platform for simulating chemical dynamics in the quantum regime. MQB devices exploit the natural structure of trapped-ion and circuit quantum electrodynamics architectures: discrete multilevel systems (qudits) encode electronic states, while bosonic modes represent vibrational degrees of freedom. This direct mapping circumvents the costly process of encoding vibrations into qubits and allows bosonic excitations to be treated natively. The result is a substantial reduction in quantum resource requirements compared to qubit-only simulators, making MQB devices especially well suited for near-term applications in chemistry.

Building on this framework, the thesis presents three major contributions. First, we report the direct observation of geometric-phase interference in non-adiabatic chemical dynamics, achieved through an MQB simulation of the Jahn–Teller model. Using wavepacket reconstruction techniques, we resolve the destructive interference pattern arising from geometric-phase accumulation. This establishes MQB simulators as a powerful tool for revealing quantum phenomena inaccessible for direct measurement.

Second, we extend the MQB framework to simulate open-system chemical dynamics, which are crucial for modelling realistic environments where dissipation and decoherence play central roles. By leveraging both intrinsic and engineered dissipation within the quantum simulator, we develop a programmable platform capable of reproducing Lindblad-type dynamics, including electronic and vibrational dephasing and population decay. This extension significantly broadens

the applicability of MQB simulators to condensed-phase chemistry, where environmental effects are indispensable.

Finally, we present a systematic resource comparison between MQB simulators and qubit-only digital approaches. By quantifying requirements such as qubit number, gate depth, and simulation time, we show that MQB devices can reduce resource costs by orders of magnitude—often five or more—for achieving the same simulation accuracy. This efficiency highlights the potential of MQB architectures to deliver genuine quantum advantage in chemical dynamics well before universal fault-tolerant quantum computers become available.

Together, these results position MQB simulators as a uniquely promising route to tackle chemical dynamics problems that have long been considered computationally intractable. Beyond demonstrating specific phenomena, the thesis establishes a general framework for extending MQB methods to both closed and open molecular systems, providing a foundation for future studies of complex chemical processes such as exciton dissociation, energy transfer, and nuclear tunnelling. In doing so, it advances the broader goal of using quantum technologies not only to reproduce known physics but also to uncover new mechanisms at the heart of chemical reactivity.

Statement of Originality

This thesis is composed of my original work and contains no previously published or written material, except where appropriately referenced in the text. I have clearly acknowledged the contributions of others to the jointly authored works included in my thesis. This thesis has not been submitted for any other degree or purpose.

I certify that the intellectual content of this thesis is the product of my own work, and that all assistance received in preparing this thesis and all sources have been acknowledged.

Vanessa Carolina Olaya Agudelo
02 February 2026

Acknowledgments

Firstly, I would like to thank my supervisor, Ivan Kassal, for your invaluable guidance, encouragement, and support throughout these years. Thanks for your patience, for always taking the time to read my work, and for sitting through my talks again and again. Thanks for your pep talks, and for trying to read my mind (you did pretty well) when I couldn't quite put it into words. Thank you for creating such a welcoming and nice environment to work in, and for always being so approachable and supportive.

I would also like to thank all the present and former members of the Kassal group whom I had the opportunity to meet over the past years. Many thanks to Ryan and Henry for generously sharing your knowledge, for taking the time to teach me new topics, and for supporting me during our projects together.

I would like to thank all the experimentalists in the Quantum Control Laboratory. You made the beautiful experiments included in this thesis possible. Chris and Ting Rei, I am especially thankful for your generosity, for patiently explaining everything about ion traps to me, and for answering all my silly questions.

To my friends and familia, thank you for the encouragement and for helping me keep my life in balance during the more difficult times of this journey. Gracias ma y pa por siempre creer en mi y apoyarme sin cuestionarme. Fausto, albricias!

Finally, thank you to my partner—for moving countries twice, for starting over with me, for your endless understanding and support, and for sharing the PhD journey with me from the other side of the world. Gracias.

Author Contribution Statement

Chapter 2 of this thesis has been published as:

C. H. Valahu*, **V. C. Olaya-Agudelo***, R. J. MacDonell, T. Navickas, A. D. Rao, M. J. Millican, J. B. Pérez-Sánchez, J. Yuen-Zhou, M. J. Biercuk, C. Hempel, T. R. Tan and I. Kassal, "Direct observation of geometric-phase interference in dynamics around a conical intersection", *Nat. Chem.* **15**, 1503–1508 (2023).

*These authors contributed equally.

Contributor	Statement of contribution	%
C. H. Valahu	Experimental implementation Data analysis and interpretation Preparation of figures Writing	30
V.C. Olaya-Agudelo	Literature search Mathematical and computational modelling Theoretical method development Data analysis and interpretation Preparation of figures Writing	30
R. J. MacDonell	Conception and design Method development Data analysis and interpretation Editing	10
T. Navickas	Experimental implementation	5
A. D. Rao	Experimental implementation	3
M. J. Millican	Experimental implementation	3
J. B. Pérez-Sánchez	Method development	2
J. Yuen-Zhou	Method development	2
M. J. Biercuk	Experimental implementation	2
C. Hempel	Conception and design	3
T. R. Tan	Conception and design Experimental implementation Editing Project supervision	5
I. Kassal	Conception and design Method development Editing Project supervision	5

In Chapter 2, my contributions included the literature review and computational simulations

for the implementation of the theoretical model (the Jahn–Teller model), the molecule–simulator mapping, and the mathematical methods required to reconstruct the molecular wavefunction from the simulator dynamics. I analysed and interpreted the simulation data and compared the results with experimental observations. I prepared the initial versions of the figures and wrote the introduction, model, and discussion sections of the manuscript, and contributed to editing the full manuscript.

Chapter 3 of this thesis has been published as:

Vanessa C. Olaya-Agudelo*, Ben Stewart*, Christophe H. Valahu, Ryan J. MacDonell, Maverick J. Millican, Vassili G. Matsos, Frank Scuccimarra, Ting Rei Tan and Ivan Kassal, "Simulating open-system molecular dynamics on analog quantum computers", *Phys. Rev. Research* **7**, 023215 (2025).

*These authors contributed equally.

Contributor	Statement of contribution	%
Vanessa C. Olaya-Agudelo	Conception and design Method development Data analysis and interpretation Preparation of figures Writing	35
Ben Stewart	Conception and design Method development Data analysis and interpretation Preparation of figures Writing	35
Christophe. H. Valahu	Method development Data analysis and interpretation Writing	10
Ryan J. MacDonell	Conception and design Method development	5
Maverick J. Millican	Method development	1.6
Vassili G. Matsos	Method development	1.6
Frank Scuccimarra	Method development	1.6
Ting Rei Tan	Conception and design Method development Editing Project supervision	5
Ivan Kassal	Conception and design Method development Editing Project supervision	5

In Chapter 3, I contributed to the initial conception and design of all dissipation channels implemented in the trapped-ion simulator. I carried out the literature review, developed the theoretical models, performed the numerical simulations, and derived and evaluated the dissipation rates for the case studies presented, including the analysis and interpretation of all results. I developed the theoretical framework for radiative electronic relaxation and for vibrational heating and cooling processes, and provided feedback on the methods used for pure electronic and vibrational dephasing. I also established the general framework for extending analog quantum simulations to open-system dynamics. In addition, I prepared Figure 3.1 and the final versions of Figures 3.2 and 3.3, took a leading role in writing the manuscript, and contributed to editing the full manuscript.

Chapter 4 of this thesis has been published as:

Tomas Navickas, Ryan J. MacDonell, Christophe H. Valahu, **Vanessa C. Olaya-Agudelo**, Frank Scuccimarra, Maverick J. Millican, Vassili G. Matsos, Henry L. Nourse, Arjun D. Rao, Michael J. Biercuk, Cornelius Hempel, Ivan Kassal and Ting Rei Tan, "Experimental Quantum Simulation of Chemical Dynamics", *J. Am. Chem. Soc.* **147**, 23566–23573 (2025).

Contributor	Statement of contribution	%
Tomas Navickas	Experimental implementation	25
Ryan J. MacDonell	Conception and design Method development Data analysis and interpretation Editing	15
Christophe H. Valahu	Experimental implementation Data analysis and interpretation Preparation of figures Writing	15
Vanessa C. Olaya-Agudelo	Method development Theoretical modelling Data analysis and interpretation Editing	15
Frank Scuccimarra	Preparation of figures	5
Maverick J. Millican	Experimental implementation	2
Vassili G. Matsos	Experimental implementation	2
Henry L. Nourse	Method development	5
Arjun D. Rao	Experimental implementation	2
Michael J. Biercuk	Experimental implementation	2
Cornelius Hempel	Conception and design	2
Ivan Kassal	Conception and design Method development Editing Project supervision	5
Ting Rei Tan	Conception and design Experimental implementation Editing Project supervision	5

In Chapter 4, I contributed to the theoretical effort by independently verifying the numerical modelling and simulator mapping, and to the data analysis by interpreting the results. I also contributed to the editing of the manuscript.

Chapter 5 of this thesis has been published as:

Henry L. Nourse*, **Vanessa C. Olaya-Agudelo*** and Ivan Kassal, "Using bosons to improve resource efficiency of quantum simulation of vibronic molecular dynamics", *arXiv* 2512.20828 (2025).

*These authors contributed equally.

Contributor	Statement of contribution	%
Henry L. Nourse	Conception and design Method development Theoretical modelling Data analysis and interpretation Preparation of figures Writing	42.5
Vanessa C. Olaya-Agudelo	Conception and design Method development Theoretical modelling Data analysis and interpretation Preparation of figures Writing	42.5
Ivan Kassal	Conception and design Method development Writing Project supervision	15

In Chapter 5, I contributed to the conception, design, and method development of the resource estimation framework. I conducted the literature review, developed the theoretical modelling, and performed numerical simulations for the extension to open quantum systems. I analysed and interpreted the results and prepared Figures 5.1-5.3. I co-wrote the initial draft of the manuscript and contributed to editing the final version.

In addition to the authorship attribution statements above, in cases where I am not the corresponding author of a published item, permission to include the published material has been granted by the corresponding author.

Vanessa Carolina Olaya Agudelo
2 February 2026

As supervisor for the candidature upon which this thesis is based, I can confirm that the authorship attribution statements above are correct.

Ivan Kassal
2 February 2026

Use of Artificial Intelligence

I used ChatGPT for copyediting. The use of this generative AI tool includes spelling corrections, minor sentence restructuring, and clarity enhancements. I confirm that where the text was modified by generative AI, the content was reviewed for possible errors, inaccuracies, and bias. I take full responsibility for the submitted thesis, confirm the work is my own, and have used generative AI in accordance with University guidelines and policies.

Financial Support

This research was supported by The Sydney Quantum Academy Postgraduate Scholarship hosted by The University of Sydney, by the Australian Research Council (FT230100653), by the United States Office of Naval Research Global (N62909-20-1-2047), by the Wellcome Leap Quantum for Bio program, and by computational resources from the Sydney Informatics Hub.

Contents

Chapter 1: Introduction

Accurately simulating chemical dynamics is one of the most challenging problems in computational chemistry. These simulations usually require a full quantum-mechanical treatment of both electronic and nuclear degrees of freedom, particularly when strong coupling makes simpler approximations unreliable. On classical computers, solving the time evolution of these systems becomes intractable—even for small molecules—because the memory requirements quickly exceed available resources. Quantum processors, in principle, offer a way around this classical bottleneck, but current devices remain too noisy and limited in scale to provide a practical alternative. Yet the ability to track chemical processes at the quantum level would offer new insights into reaction mechanisms, energy transfer, and environmental effects that are inaccessible to experiments, especially at ultrafast timescales. This thesis explores an alternative near-term solution: the mixed-qudit-boson (MQB) framework, which uses qudits to represent electronic states and bosonic modes to encode nuclear motion. By exploiting this natural mapping, MQB simulators provide a resource-efficient platform for capturing the essential quantum dynamics of molecular systems, bridging the gap between the limitations of classical computation and the hardware constrains of qubit-only quantum processors.

This introductory chapter sets the stage for the thesis by outlining the central challenges and motivations behind simulating chemical dynamics. We begin by emphasising the importance of chemical dynamics, both as a fundamental tool in chemistry and as a pathway to practical applications. We then examine why the accurate simulation of chemical dynamics is such an outstanding problem: the need for a full quantum-mechanical treatment of electronic and nuclear degrees of freedom, combined with the exponential scaling of Hilbert space, renders exact solutions on classical computers intractable. To provide context, the chapter introduces the main theoretical models that underpin chemical simulation, before reviewing the classical computational methods that have been developed to approximate these dynamics and their limitations. We then turn to quantum simulation, first discussing qubit-only approaches and their susceptibility to external noise, and finally introducing the MQB framework as a promising alternative that overcomes these barriers.

1.1 Chemical dynamics

Chemical dynamics describe the time evolution of chemical processes, which can be probed through measurable quantities, or observables, at any point in time. By accessing these observables, one can extract valuable information—such as reaction mechanisms and kinetics, pathways of energy absorption, transfer, and dissipation, as well as the influence of the surrounding environment—that deepens our understanding of molecular processes. Such insights are not only of fundamental interest but also have broad practical implications, from the rational design of more efficient catalysts for industrial applications, to the development of advanced energy materials for solar energy conversion, and the optimisation of molecular pathways for faster and more effective drug delivery.

Simulating chemical dynamics provides access to observables that are otherwise inaccessible experimentally, where only limited quantities—such as spectra or scattering cross-sections—can be measured. In contrast, simulations allow us to resolve the full microscopic dynamics of a system, tracking in detail how a process unfolds at the atomic and molecular levels. For example, one can focus on a specific aspect of the reaction, such as the breaking of a chemical bond, the vibration of atoms, or the transfer of energy between molecular subunits. By following these targeted dynamics, simulations of chemical processes become an indispensable complement to experiments for developing a predictive understanding of chemical reactivity.

Among the most difficult problems to simulate are those that involve non-adiabatic dynamics, such as radiationless transitions, photochemical reactions, electron and energy transfer, proton-coupled electron transfer, zero-point motion, and tunnelling, all of which involve strong coupling between electronic and nuclear degrees of freedom. The Born–Oppenheimer approximation—often an excellent starting point in chemical dynamics—breaks down when electronic potential-energy surfaces approach one another. In these regimes, dynamics are steered by conical intersections (points where the potential energy surfaces have the same energy) [1–3], enabling ultrafast population transfer and shaping photochemical outcomes. Non-adiabatic effects are ubiquitous and play a central role in chemistry, yet capturing them accurately remains challenging.

A canonical illustration of non-adiabatic effects is the primary event in vision: the *cis–trans* photoisomerisation of retinal in the protein rhodopsin [4]. Following photoabsorption, this ultrafast reaction occurs on the femtosecond timescale, converting the retinal chromophore from its 11-*cis* to all-*trans* configuration (see fig. 1.1a), is mediated by a conical intersection between the ground and excited electronic states (see fig. 1.1b). Furthermore, the surrounding protein environment accelerates the isomerisation and ensures its high efficiency [4], compared to the same process in solution. This example highlights several recurring features of photochemical

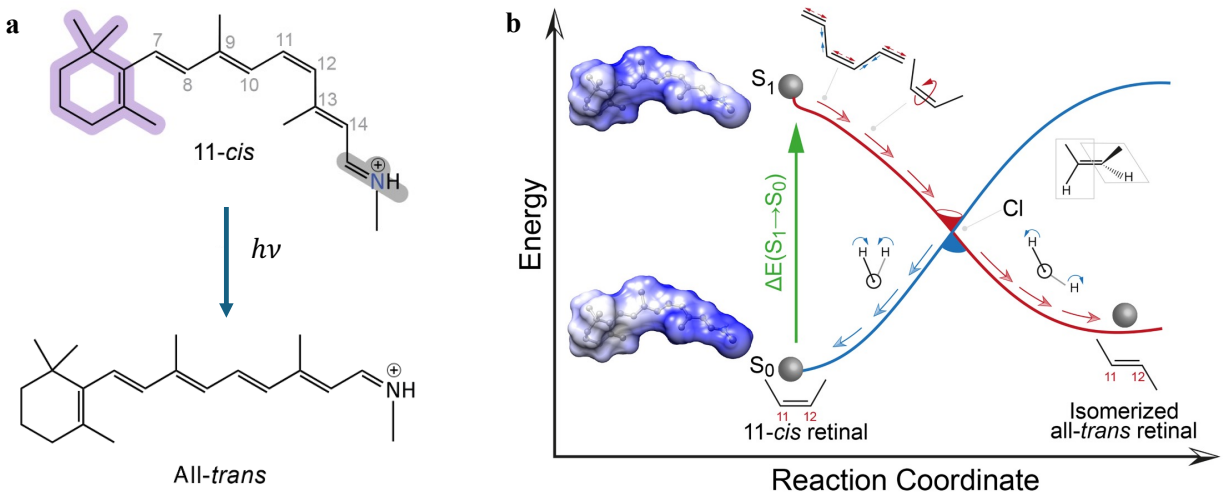

Figure 1.1: First step in the vision process as an example of non-adiabatic dynamics: photoisomerisation of retinal from 11-*cis* to all-*trans* mediated by a conical intersection between the ground and excited states. **a.** The retinal molecule is initially in the 11-*cis* configuration; after photoexcitation it isomerises to an all-*trans* configuration on an ultrafast timescale. **b.** Representation of the same process using electronic potentials as a function of the reaction coordinate. Photoabsorption promotes the molecule from the S_0 to the S_1 state. The reaction coordinate contains contributions from several modes [4], and the completed isomerisation is mediated by a conical intersection (a geometry point where electronic states are degenerate). Figure modified from [4].

dynamics: their ultrafast timescales, their reliance on non-adiabatic pathways through conical intersections, and the profound influence of the molecular environment.

The simulation of such processes is challenging because it requires a fully quantum-mechanical description of both electronic and nuclear degrees of freedom. The presence of conical intersections breaks down the Born–Oppenheimer approximation. Furthermore, environmental effects, such as those provided by the protein scaffold in rhodopsin, are even harder to capture with classical approaches. These factors makes photochemical reactions and non-adiabatic dynamics a testing ground for new computational strategies, motivating the exploration of alternative quantum simulation methods.

1.2 Why is it so difficult to simulate chemical dynamics?

The starting point for simulating chemical processes governed by quantum mechanics is the time-dependent Schrödinger equation,

$$i\hbar \frac{d\,|\psi\rangle}{dt} = H\,|\psi\rangle\,, \tag{1.1}$$

which describes the time evolution of a molecular system through its state vector $|\psi\rangle$ under the influence of the Hamiltonian H. At any given time, the state can be expressed as a linear

superposition of the elements of a complete basis set $\{|\psi_i\rangle\}$—such as eigenstates of H, electronic configurations, or spatial grids—

$$|\psi\rangle = \sum_i c_i |\psi_i\rangle , \tag{1.2}$$

where $|c_i|^2$ gives the probability of finding the system in state $|\psi_i\rangle$, with normalisation $\sum_i |c_i|^2 = 1$.

Directly solving eq. (1.1) on classical computers for realistic molecular systems rapidly becomes intractable as the system size increases. At each time step, the system's state must be represented by storing the coefficients c_i. If each degree of freedom is represented by a basis set of size b, then increasing the number of degrees of freedom f causes the dimension of the state vector—and thus the number of coefficients—to scale as b^f. This problem is particularly acute when representing continuous variables on classical computers. Quantities such as nuclear positions and electronic coordinates must be discretised into basis functions or grid points. For an accurate simulation, the grid spacing must be fine, which means that each degree of freedom requires a large number of points. As an illustrative example, even a relatively small molecule with 24 nuclear degrees of freedom (10 atoms), each represented with a spatial grid basis of size $b = 10$, would require tracking 10^{24} coefficients at all times, which already surpasses any available computational capability [5–8].

Consequently, the exponential scaling with the number of degrees of freedom is even more severe for the discretisation of continuous variables. Even modest molecular systems therefore demand prohibitively large memory and computational resources.

The challenge is exacerbated for open quantum systems, where environmental interactions must also be modelled. In these cases, the molecular system is described not by a single wavefunction, but by a statistical ensemble of states eq. (1.2), represented by a density matrix,

$$\rho = \sum_{i,j} p_{ij} |\psi_i\rangle \langle\psi_j| , \tag{1.3}$$

where the diagonal elements p_{ii} give the probability of the system being in state $|\psi_i\rangle$, and the off-diagonal elements encode quantum coherences. The computational cost of simulating molecular systems interacting with their environments increases dramatically, since the density matrix contains N^2 elements, where N is the dimension of the Hilbert space spanned by the states $|\psi_i\rangle$. This quadratic scaling in memory makes open-system simulations even more demanding than closed-system ones.

In practice, one resorts to truncations, such as limiting the number of active electronic states or vibrational modes, but these inevitably reduce accuracy. Even with modern supercomputers, fully quantum simulations quickly exceed feasible computational capabilities once the system extends beyond only a few atoms. To address these limitations, a variety of approximate models

and computational methods have been developed. All these are discussed in the following sections.

1.3 Models used for simulating chemical dynamics

Having introduced the motivation for simulating chemical dynamics and the computational challenges involved, here we establish the theoretical models that underlie most approaches to chemical dynamics simulation. These models provide the essential bridge between the exact, but intractable, fully quantum-mechanical description of a molecule and the practical approximations needed for classical and quantum computational methods. By making physically motivated simplifications, they allow us to capture key aspects of electronic and nuclear dynamics while reducing the complexity of the underlying equations.

Among the most widely used are the Born–Oppenheimer approximation, the adiabatic and diabatic representations, and the vibronic coupling model. Together, these form the conceptual foundation for describing electronic–nuclear interactions and for developing trajectory-based or wavefunction-based methods in computational chemistry. Despite their utility, each carries intrinsic limitations. For instance, the Born–Oppenheimer approximation neglects strong non-adiabatic couplings and fails near conical intersections, while diabatic and vibronic coupling models usually require Hamiltonian truncations, introducing further approximations whose accuracy depends on the system under study. These caveats are central to both classical and quantum simulations, as they dictate the conditions under which a given computational approach is valid.

Finally, the master equation formalism provides a framework to go beyond isolated systems and describe the dynamics of molecules in realistic environments, where dissipation and decoherence play central roles. This formalism is particularly important for quantum simulation in the MQB framework, as it enables the inclusion of open-system effects that are challenging to treat classically. In this way, the master equation extends the reach of molecular simulations to the condensed-phase regime, where environmental interactions often determine chemical reactivity and reaction mechanism.

In what follows, we outline these well-establish models, emphasising not only their role in enabling simulations of chemical processes, but also how they set the stage for the MQB approach explored in this thesis.

1.3.1 Born-Oppenheimer (adiabatic) approximation

In chemical dynamics, a well-known approach is to treat electronic and nuclear motion separately. This relies on the large difference between nuclear and electronic masses, which leads to different characteristic timescales of motion. First introduced by Born and Oppenheimer [9], the approximation allows the molecular wavefunction to be expanded in terms of electronic eigenfunctions that depend parametrically on the nuclear coordinates. In the exact treatment, the Schrödinger equation generates non-diagonal terms that couple nuclear and electronic states. However, at low energies, for small-amplitude nuclear vibrations, and in the absence of electronic degeneracies, these couplings can be safely neglected. Under these conditions, the dynamics can be effectively restricted to a single electronic state, providing a practical framework for simulating molecular processes.

We start by describing the Hamiltonian of a general molecular system [2, 10],

$$H = T_e + T_N + U(\mathbf{r}, \mathbf{Q}), \tag{1.4}$$

where T_e and T_N are kinetic energy operators of the electrons and nuclei, respectively, and $U(\mathbf{r}, \mathbf{Q})$ is the potential energy of all particles. Here, $\mathbf{r} = (r_1, r_2, \ldots, r_j)$ denotes the electronic coordinates and $\mathbf{Q} = (Q_1, Q_2, \ldots, Q_M)$ the nuclear coordinates.

The central idea is to describe the electronic and nuclear motions separately. For the electronic motion, we fix the nuclei in space so that $T_N = 0$, and defined the eigensystem of the electronic Hamiltonian,

$$H_e \Phi_n(\mathbf{r}, \mathbf{Q}) = V_n(\mathbf{Q}) \Phi_n(\mathbf{r}, \mathbf{Q}), \tag{1.5}$$

where $H_e = T_e + U(\mathbf{r}, \mathbf{Q})$, $\Phi_n(\mathbf{r}, \mathbf{Q})$ are the adiabatic electronic states and $V_n(\mathbf{Q})$ are the electronic energies at nuclear geometry $\mathbf{Q}$, also known as *potential energy surfaces* (PESs).

For the nuclear motion, the total molecular wavefunction can be expanded in the adiabatic basis as

$$\Psi(\mathbf{r}, \mathbf{Q}) = \sum_n \chi_n(\mathbf{Q}) \Phi_n(\mathbf{r}, \mathbf{Q}), \tag{1.6}$$

where $\chi_n(\mathbf{Q})$ are nuclear wavefunctions associated with each electronic state.

Substituting this ansatz into the molecular Schrödinger equation,

$$(H - E)\Psi(\mathbf{r}, \mathbf{Q}) = 0, \tag{1.7}$$

and projecting onto the state $\Phi_n(\mathbf{r}, \mathbf{Q})$ yields a set of coupled equations for the nuclear wavefunctions,

$$\left[T_N + V_n(\mathbf{Q}) - E\right] \chi_n(\mathbf{Q}) = \sum_m \Lambda_{nm} \chi_m(\mathbf{Q}), \tag{1.8}$$

where the non-adiabatic couplings are

$$\Lambda_{nm} = -\int d\mathbf{r}\Phi_n^* \left[T_n, \Phi_m\right]. \tag{1.9}$$

The operator T_n acts on the nuclear dependence of the electronic states, and thus Λ_{nm} represents couplings between different adiabatic electronic states mediated by nuclear motion. Since the electronic energies are typically much larger than the nuclear kinetic energy, these terms are often a small perturbation and can be neglected. This leads to the *Born–Oppenheimer adiabatic approximation*, in which the total wavefunction reduces to a single product state,

$$\Psi(\mathbf{r}, \mathbf{Q}) \approx \chi_n(\mathbf{Q})\Phi_n(\mathbf{r}, \mathbf{Q}). \tag{1.10}$$

The nuclei are evolving on a single PES $V_n(\mathbf{Q})$, while the electrons are assumed to adjust instantaneously to their motion. This separation of time-scales underpins much of computational chemistry, as it reduces the full electron–nuclear dynamics to nuclear motion on pre-computed electronic landscapes.

Despite the usefulness of this approximation, it may fail in many important cases—particularly when potential energy surfaces of different electronic states come close in energy. In such regions, the non-adiabatic operators Λ_{nm} cannot be neglected for those electronic indices n and m that belong to the manifold of nearly degenerate states. Their non-trivial effects mediate ultrafast population transfer between adiabatic electronic states, especially in near-degenerate regions. As a result, solving the Schrödinger equation becomes considerably more complicated, and perturbative approaches generally fall short. This breakdown of the Born–Oppenheimer approximation highlights the need for alternative representations—such as diabatic states or vibronic coupling models—that can explicitly incorporate these strong non-adiabatic effects.

1.3.2 Diabatic representation

While the Born–Oppenheimer approximation and the adiabatic representation provide a convenient starting point for molecular simulations, they become inadequate when describing processes such as radiationless transitions and photoinduced electron or energy transfer. In these cases, the potential energy surfaces are nearly degenerate (or exactly degenerate), and the electronic states change character rapidly as a function of nuclear coordinates. This gives rise to large non-adiabatic couplings, with derivative terms that can even diverge near intersections of potential energy surfaces. Such behaviour makes quantum dynamical treatments in the adiabatic basis particularly challenging.

The diabatic representation [2, 10] offers an alternative perspective. Instead of using electronic states that diagonalise the electronic Hamiltonian at each nuclear geometry, diabatic states are defined to vary smoothly with nuclear coordinates. This basis is obtained through

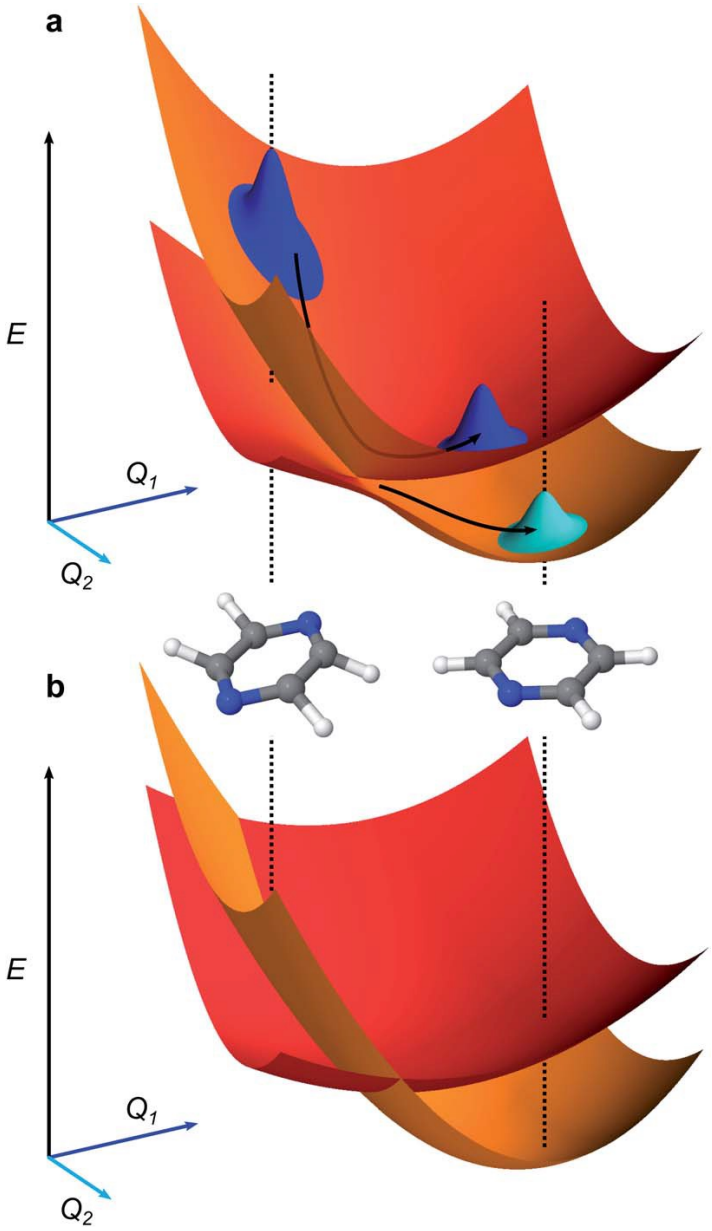

Figure 1.2: Adiabatic and diabatic potential surfaces of the first excited electronic states of pyrazine. **a.** Adiabatic potential surface as a function of the relevant nuclear coordinates Q_1 and Q_2. The evolution of nuclear wavepacket along the surfaces is also shown, and each electronic state is associated with a distinct molecular geometry. **b.** Diabatic states (without the interstate coupling) transformed from a. Figure from [11].

an orthogonal transformation of a subset of adiabatic states, which eliminates most of the problematic derivative couplings that complicate the adiabatic description. The small residual couplings that remain can often be neglected in practice. As a result, the complexity of the problem is shifted into off-diagonal elements of the electronic Hamiltonian. The resulting diabatic states are smoother and often provide a more intuitive physical picture of the interactions between states.

To illustrate this smooth behaviour, fig. 1.2 compares the excited adiabatic electronic states of pyrazine [11] with the diabatic representation. The excited-state dynamics of this molecule are well known for the conical intersection between the first excited states, which leads to strong

couplings and ultrafast dynamics. Figure 1.2a shows the adiabatic potential energy surfaces along different nuclear coordinates, where each electronic state reflects a different molecular configuration. Figure 1.2b depicts the corresponding diabatic representation, which remains smooth near the conical intersection (with diabatic couplings not included).

The diabatic representation has proven indispensable for both classical computational methods and quantum simulations, despite its theoretical and computational limitations [2]. It is neither unique nor exact: many different unitary transformations can generate distinct sets of diabatic states, and practical methods to construct them often involve approximations or system-specific criteria, each associated with particular computational limitations. Nevertheless, the diabatic framework greatly simplifies the construction of model Hamiltonians for quantum dynamics. By focusing on a small set of diabatic states and their couplings, one can capture the essential physics of complex processes such as charge transfer, proton-coupled electron transfer, or exciton dynamics in molecular aggregates.

Finally, the diabatic picture is particularly valuable for vibronic coupling models, where both electronic and vibrational degrees of freedom are retained in a manageable form. Its natural mapping of electronic states onto discrete levels and vibrational modes onto bosonic degrees of freedom makes it especially well suited MQB simulation of chemical dynamics.

1.3.3 Vibronic coupling models

Assuming a diabatic representation, where electronic states are chosen to vary smoothly with nuclear coordinates, one can develop simplified Hamiltonians that capture the essential interactions between a small set of electronic states and the vibrational modes of the molecule. This leads to the vibronic coupling model [2, 10], which is a widely used framework for describing non-adiabatic dynamics. In this approach, the molecular Hamiltonian is expressed in terms of a diabatic electronic basis, with vibrational degrees of freedom explicitly retained. The potential energy surfaces are then expanded as a Taylor series around a chosen reference geometry, typically the equilibrium configuration of the ground state. This expansion naturally introduces couplings between electronic and vibrational modes, allowing a compact and systematic description of processes such as internal conversion, conical intersections, and ultrafast photodynamics.

An essential step in constructing vibronic model Hamiltonians is the choice of nuclear coordinates. The form of both the kinetic- and potential-energy operators depends on this choice, and selecting a convenient coordinate system can greatly simplify the representation of the dynamics. In quantum treatments, where the cost of computation grows rapidly with dimensionality, it is standard practice to eliminate overall translation and rotation and to describe vibrations in terms of dimensionless normal coordinates [2]. These coordinates are defined with respect to a chosen reference geometry, typically the equilibrium geometry of the

electronic ground state. Assuming small displacements about this point simplifies both the kinetic- and potential-energy operators, as the normal modes then represent small-amplitude vibrations relative to the equilibrium structure.

Expanding the potential-energy surfaces as a Taylor series in these coordinates provides a natural and systematic way to include vibrational couplings, while the kinetic-energy operator takes a simple form that is well suited to quantum dynamical calculations. In this way, the vibronic Hamiltonian can be expressed as the sum of the nuclear kinetic-energy operator and a reference harmonic potential, together with perturbative coupling terms that account for the influence of vibrational displacements on the electronic states. The operators for the nuclear kinetic and harmonic potential energies are given by [2]

$$T_N = -\frac{1}{2}\sum_i \hbar\omega_i \frac{\partial^2}{\partial Q_i^2}, \tag{1.11}$$

$$V_0 = \frac{1}{2}\sum_i \hbar\omega_i Q_i^2. \tag{1.12}$$

where Q_i is the dimensionless normal coordinate and ω_i is the harmonic vibrational frequency of the ith mode.

The total Hamiltonian can be written as,

$$H_{\mathrm{VC}} = T_N + V_0 + \mathbf{W}, \tag{1.13}$$

where $\mathbf{W}$ describes deviations of the potential energy from the reference harmonic PES for small displacements. The matrix elements of $\mathbf{W}$ in the diabatic basis $\{n\}$ are expressed as [2]

$$W_{nn}(Q) = E_n + \sum_i \kappa_i^{(n)} Q_i + \sum_{i,j} \gamma_{i,j}^{(n)} Q_i Q_j + \ldots, \tag{1.14}$$

$$W_{nn'}(Q) = \sum_i \lambda_i^{(nn')} Q_i + \sum_{i,j} \mu_{ij}^{(nn')} Q_i Q_j + \ldots, \quad (n \neq n'). \tag{1.15}$$

where E_n is the vertical excitation energy of the nth electronic state, and the coefficients κ_i, $\gamma_{ij}^{(n)}$, $\lambda_i^{(nn')}$, etc. are electronic-vibrational coupling constants. They are defined as [2]

$$\kappa_i^{(n)} = \left(\frac{\partial W_{nn}}{\partial Q_i}\right)_0, \tag{1.16}$$

$$\lambda_i^{(nn')} = \left(\frac{\partial W_{nn'}}{\partial Q_i}\right)_0, \tag{1.17}$$

$$\gamma_{ij}^{(n)} = \frac{1}{2}\left[\left(\frac{\partial^2 W_{nn}}{\partial Q_i \partial Q_j}\right)_0 - \hbar\omega_i \delta_{ij}\right]. \tag{1.18}$$

with the derivatives evaluated at the reference ground-state geometry.

Here, $\kappa_i^{(n)}$ are the first-order intra-state coupling constants, describing how the nth electronic state is perturbed by nuclear displacements. The $\lambda_i^{(nn')}$ are the first-order inter-state coupling

constant, responsible for vibronic mixing between different electronic states. The quadratic terms $\gamma_{ij}^{(n)}$ describe changes in vibrational modes upon excitation and are related to the Duschinsky rotation [12] of normal modes in the excited state.

In practice, ultrafast dynamics in non-adiabatic processes can often be described accurately by retaining only the leading-order terms in the vibronic expansion, corresponding to the first-order coupling between electronic states and nuclear vibrations [13–15]. This leads to the linear vibronic coupling (LVC) Hamiltonian, which includes only the terms linear in the nuclear displacements Q_j within the diabatic potential-energy matrix elements $W_{nn'}$,

$$H_{\mathrm{LVC}} = \frac{1}{2}\sum_j \hbar\omega_j \left(Q_j^2 + P_j^2\right) + \sum_n E_n \left|n\right\rangle \left\langle n\right| + \sum_n \sum_i \kappa_i^{(n)} Q_i \left|n\right\rangle \left\langle n\right| + \sum_{n,n'} \sum_i \lambda_i^{(nn')} Q_i \left|n\right\rangle \left\langle n'\right|, \tag{1.19}$$

where the diabatic basis has been written in ket notation for convenience.

The vibronic coupling Hamiltonian provides a compact yet flexible description of the essential interactions between electronic and vibrational degrees of freedom, and is particularly well suited to MQB simulation. Importantly, it can also be used within open quantum system frameworks, where environmental effects such as dissipation and decoherence are incorporated through additional terms in the master equation, as we explore next.

1.3.4 Master equations for open quantum systems

Up to this point, we have considered mainly models for isolated molecular dynamics. However, most realistic chemical processes occur in complex environments, where interactions with the surroundings can play a decisive role in determining the outcome of the reaction. These environmental effects are not merely minor perturbations: they govern essential processes such as electronic and vibrational relaxation, dephasing, and energy dissipation, all of which strongly influence reactivity and photodynamics in condensed-phase chemistry and biology. To capture such effects, one must move beyond a closed-system description and adopt an open quantum systems framework.

In an open system, the state of the molecule and its bath together is described by the density operator $\rho(t) = \left|\psi(t)\right\rangle \left\langle\psi(t)\right|$, where $\left|\psi(t)\right\rangle$ is the combined state vector of the system and bath. The time evolution of $\rho(t)$ follows the Liouville–von Neumann equation [16],

$$\frac{d}{dt}\rho(t) = -\frac{i}{\hbar}[H, \rho(t)], \tag{1.20}$$

which generalises the Schrödinger equation to density matrices. However, in practice one is usually interested in the reduced state of the system alone, obtained by tracing over the bath degrees of freedom. To render this problem tractable, we introduce physically motivated approximations that are valid when the system–bath coupling is sufficiently weak. These

approximations lead to effective master equations describing the dynamics of open quantum systems.

We begin by partitioning the Hamiltonian of the full molecule–bath system as

$$H = H_S + H_B + H_{SB}, \tag{1.21}$$

where H_S and H_B are the free Hamiltonians of the system and bath, respectively, and H_{SB} describes their interaction.

The derivation of master equations is most conveniently carried out in the interaction picture [16], in which eq. (1.20) becomes

$$\frac{d}{dt}\rho^{(I)}(t) = -\frac{i}{\hbar}[H_{SB}^{(I)}(t), \rho^{(I)}(t)], \tag{1.22}$$

which can be integrated to yield

$$\rho^{(I)}(t) = \rho^{(I)}(0) - \frac{i}{\hbar}\int_0^t d\tau [H_{SB}^{(I)}(\tau), \rho^{(I)}(\tau)]. \tag{1.23}$$

This result can be substituted back into eq. (1.22) to give

$$\frac{d}{dt}\rho_S^{(I)}(t) = -\frac{1}{\hbar^2}\int_0^t d\tau \ \mathrm{Tr}_B \left[H_{SB}^{(I)}(t), \left[H_{SB}^{(I)}(\tau), \rho^{(I)}(\tau)\right]\right], \tag{1.24}$$

where we have traced over the bath. The term $\left[H_{SB}^{(I)}(t), \rho^{(I)}(0)\right]$ is an energy shift in the system and was set to zero without affecting the dynamics [16]. Equation (1.24) already scales quadratically with the system-bath interaction Hamiltonian. For weak system–bath coupling, no further substitutions are required, since the resulting higher-order terms (scaling as $\mathcal{O}\left((H_{SB}^{(I)})^3\right)$) are small and can safely be ignored.

At this point, the dynamics remain intractable because the full system–bath density matrix still appears. To proceed, the Born approximation is introduced (valid for a weak system–bath coupling), in which the system-bath state is always separable. For a large bath, its state is negligibly disturbed by its interaction with the system; therefore, at any time t, the joint state can be factorised as $\rho^{(I)}(t) \approx \rho_S^{(I)}(t) \otimes \rho_B$, where ρ_B is the equilibrium bath state [16]. Substituting into eq. (1.24) gives,

$$\frac{d}{dt}\rho_S^{(I)}(t) = -\frac{1}{\hbar^2}\int_0^t dt' \ \mathrm{Tr}_B \left[H_{SB}^{(I)}(t), \left[H_{SB}^{(I)}(t-t'), \rho_S^{(I)}(t-t') \otimes \rho_B\right]\right], \tag{1.25}$$

where we made the substitution $t' = t - \tau$. The resulting eq. (1.25) is more tractable but still retains a dependence on the past system state, reflecting memory effects in the bath.

Eliminating this memory leads to the Markov approximation. If bath correlations decay on a timescale τ_B much shorter than the system's evolution timescale τ_S, then the bath has effectively no memory of past interactions, and the system's evolution depends only on its

present state. Under this assumption, $\rho^{(I)}(t-t') \approx \rho^{(I)}(t)$, and the upper integration limit may be extended to infinity [16],

$$\frac{d}{dt}\rho_S^{(I)}(t) = -\frac{1}{\hbar^2}\int_0^\infty dt' \ \mathrm{Tr}_B \left[H_{SB}^{(I)}(t), \left[H_{SB}^{(I)}(t-t'), \rho_S^{(I)}(t)\otimes\rho_B\right]\right]. \tag{1.26}$$

Together, the Born and Markov approximations lead to the Redfield eq. (1.26), which is widely used in molecular dynamics [17]. However, the Redfield generator does not guarantee completely positive evolution of $\rho_S(t)$, so in some cases it can predict unphysical negative probabilities [16, 17].

To restore positivity, one can average over rapidly oscillating terms in the master equation 1.26, known as the secular approximation. To make this oscillation evident, we start by decomposing the system–bath interaction Hamiltonian (in the Schrödinger representation) into,

$$H_{SB} = \sum_\alpha A_\alpha \otimes B_\alpha \tag{1.27}$$

where the operator A_α acts on the system and B_α on the bath. Assuming that the spectrum of H_S is discrete, we define the operator $\Pi(\varepsilon)$ as the projector onto the eigenspace of the the eigenvalue ε, so that A_α^ω can be defined as [16]

$$A_\alpha^\omega \equiv \sum_{\varepsilon'-\varepsilon=\omega} \Pi(\varepsilon) A_\alpha \Pi(\varepsilon'). \tag{1.28}$$

The system's operator A_α can be written in terms of A_α^ω by summing eq. (1.28) over ω,

$$A_\alpha = \sum_\omega A_\alpha^\omega. \tag{1.29}$$

Replacing this in eq. (1.27), the system-bath interaction Hamiltonian is now written as as spectral decomposition of the system's Hamiltonian,

$$H_{SB} = \sum_{\alpha,\omega} A_\alpha^\omega \otimes B_\alpha. \tag{1.30}$$

We aim to write the interaction Hamiltonian H_{SB} into the interaction picture $H_{SB}^{(I)}(t)$

$$H_{SB}^{(I)}(t) = \sum_{\alpha,\omega} A_\alpha^\omega(t) \otimes B_\alpha(t), \tag{1.31}$$

where $A_\alpha^\omega(t) = e^{-i\omega t}A_\alpha^\omega$ and $B_\alpha(t) = e^{iH_B t}B_\alpha e^{-iH_B t}$ are the corresponding interaction picture operators. Replacing eq. (1.31) into eq. (1.26), neglecting oscillating cross-terms ($\omega \neq \omega'$), and restoring the Schrödinger picture, the Redfield equation reduces to the Lindblad master equation [16],

$$\frac{d\rho_S}{dt} = -\frac{i}{\hbar}\left[H_S + H_{LS}, \rho_S\right] + \sum_i \gamma_i \left(L_i \rho_S L_i^\dagger - \tfrac{1}{2}L_i^\dagger L_i, \rho_S\right). \tag{1.32}$$

Here the L_i are Lindblad jump operators, γ_i are corresponding rates determined by bath correlation functions, and H_{LS} is the Lamb-shift Hamiltonian, which is usually omitted in the weak-Markovian regime because it is a small, model-dependent, can be absorbed into the system Hamiltonian and does not affect dissipative dynamics [16].

This final form ensures that the reduced density matrix evolves through a completely positive, trace-preserving map, making the Lindblad equation a practical tool for modelling open quantum dynamics. Within the regime of validity—weak system–bath coupling and Markovian environments—it allows one to classify dissipation in molecular systems into population relaxation and pure dephasing [17]. Indeed, Lindblad-type equations have been applied successfully to electron transfer [18], vibrational relaxation in solvated molecules [19–21], and environment-assisted energy transport in molecular aggregates [22]. Moreover, their operator-sum structure makes them particularly suitable for analog quantum simulation, where engineered dissipation can be introduced to mimic realistic condensed-phase environments.

It is worth noting, however, that when the coupling to the bath is not weak, or when memory effects become significant, more sophisticated non-Markovian master equations are required [23, 24]. Such approaches go beyond the Born–Markov framework, retaining environmental correlations and enabling the description of strong-coupling and long-time dynamics [23, 24], albeit at the cost of greater mathematical and computational complexity. In this thesis, we focus on the weak-coupling regime, which is most relevant to the physical scenarios considered, while acknowledging that non-Markovian extensions remain an important direction for future research.

1.4 Classical computational methods for chemical dynamics simulation

As discussed in the previous sections, a full quantum-mechanical treatment of chemical dynamics quickly becomes computationally intractable due to the exponential growth of the Hilbert space with system size. At the same time, many processes of central importance in chemistry—such as photochemical reactions, ultrafast processes, and charge or energy transfer—cannot be described accurately without explicitly accounting for quantum effects. This tension between the need for quantum accuracy and the practical limitations of classical computation has motivated the development of a wide range of approximate methods.

These methods typically combine quantum and classical treatments, using classical mechanics for the nuclear motion while retaining a quantum description of the electronic subsystem.

Among the most widely used methods are trajectory-based approaches, such as Ehrenfest

dynamics and surface hopping, which treat nuclear motion along classical trajectories coupled to quantum electronic states. Similarly, ab initio multiple spawning (AIMS) method, dynamically refines the nuclear wavefunction into trajectory "spawns" near regions of strong non-adiabatic coupling. Exact methods, including the split-operator method, only works for small molecular systems. More advanced formulations, such as the Multi-Configuration Time-Dependent Hartree (MCTDH) method, retain a fully quantum description of the nuclear wavefunction but employ efficient, adaptive basis representations to reduce computational cost. These approaches form the foundation of modern computational strategies for simulating non-adiabatic chemical dynamics, each offering a different balance between accuracy, computational efficiency, and applicability to complex molecular systems.

In the following, these approaches are briefly explained, outlining their theoretical foundations and the trade-off that determine their suitability for specific types of non-adiabatic chemical dynamics problems.

1.4.1 Trajectory-based methods

An inexpensive class of approaches for simulation non-adiabatic chemical dynamics are mixed quantum–classical dynamics methods, in which the nuclei are treated classically while the electrons are described quantum mechanically. The interaction between the two types of degrees of freedom is treated self-consistently, so that the quantum subsystem responds to the influence of the classical nuclei and vice versa. A central example is the mean-field Ehrenfest method [25–27], where the electronic wavefunction evolves according to the time-dependent Schrödinger equation and the nuclei follow Newton's equations of motion under forces derived from the gradient of the expectation value of the electronic Hamiltonian. This mean-field treatment effectively averages over multiple electronic states simultaneously. The Ehrenfest approach is representation-invariant (adiabatic or diabatic), conserves total energy, and is computationally inexpensive, making it appealing for exploratory studies. However, because all trajectories evolve on a mean-field potential, the method fails to capture quantum–classical correlations accurately, particularly in situations where populations should branch between distinct potential energy surfaces. As a result, it tends to overestimate coherence, fails to capture trajectory branching for systems involving strong non-adiabatic effects or complex potential energy landscape [26], which limits its predictive accuracy in strongly non-adiabatic regimes.

To overcome the inability of mean-field dynamics to capture branching between electronic states, trajectory-based alternatives such as surface hopping were developed [28]. Similarly to the Ehrenfest method, surface hopping adopts a mixed quantum–classical framework in which the nuclei are treated as classical particles evolving (classical trajectories) along adiabatic potential energy surfaces, while the electronic degrees of freedom are described quantum mechanically [28].

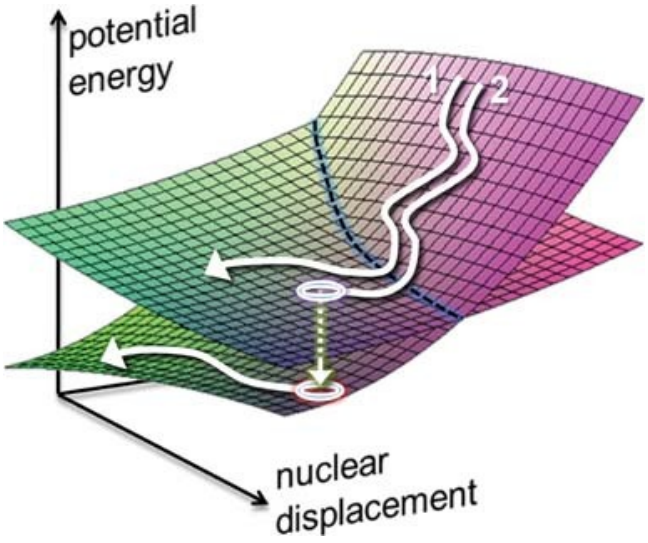

Figure 1.3: Representation of trajectory surface hoping (TSH). It depicts the wavepacket branching in a region with strong non-adiabatic couplings, each wavepacket trajectory are stochastically distributed among the coupled surfaces. This efficient method was proposed more than 50 years ago to overcome the limitation of previous trajectory-based methods [28]. Figure from the graphical abstract of [29].

In this approach, each trajectory follows a single potential energy surface until regions of strong non-adiabatic coupling are encountered, where stochastic 'hops' between surfaces can occur, allowing for the branching of nuclear trajectories into different electronic states. The potential energy surfaces and couplings are typically evaluated 'on the fly' as the nuclei move, which enables the simulation of relatively large molecular systems and long timescales with more favourable scaling than fully ab initio quantum dynamics [30]. However, because surface hopping is not rigorously derived from the time-dependent Schrödinger equation [31], the results are not exact and in some cases can lack predictive reliability. In addition, the method is not invariant under different choices of electronic basis, which restricts its applicability to certain problems. Overall, surface hopping provides a practical and computationally efficient tool for exploring non-adiabatic molecular dynamics, Yet, because it is not rigorously derived from the time-dependent Schrödinger equation and is basis-dependent, its results can be unreliable for problems requiring quantitative accuracy.

Among trajectory-based methods, the ab initio multiple spawning (AIMS) approach provides a more systematic quantum-mechanical treatment of nuclear motion compared to surface hopping [32, 33]. In AIMS, the molecular wavefunction is expanded in terms of Gaussian basis functions—so-called trajectory basis functions (TBF)—that evolve along classical trajectories on adiabatic potential energy surfaces. Crucially, when the system enters regions of strong non-adiabatic coupling, new basis functions are 'spawned' onto different electronic states, allowing the method to naturally capture branching of the nuclear wavepacket and maintain quantum coherence between pathways. This mechanism overcomes one of the major shortcomings of surface hopping, where coherence is often artificially lost. At the same time, AIMS retains

the practical advantage of on-the-fly ab initio electronic structure calculations, avoiding the need for global potential energy surfaces [31]. However, despite these advances, AIMS still faces significant limitations. The number of Gaussian basis functions can grow rapidly in complex dynamics, leading to steep computational costs, and accuracy depends sensitively on the choice of Gaussian widths and spawning criteria [32, 33]. Moreover, the description of nuclear motion remains approximate, and long-time coherence or strongly coupled multidimensional dynamics can be difficult to converge.

1.4.2 Split-operator method

A fully quantum nuclear movement is provided by the split-operator method, a widely used approach for numerical propagation of the time-dependent Schrödinger equation [34, 35]. Its central idea is to take advantage of the fact that the Hamiltonian of a molecular system can often be written as the sum of a kinetic energy operator, T, and a potential energy operator, V. Since T and V are diagonal in complementary representations (momentum and coordinate space, respectively), the time evolution operator for a short time step Δt can be approximated using the second-order Trotter expansion [36–38],

$$e^{-iH\Delta t/\hbar} \approx e^{-iV\Delta t/(2\hbar)} e^{-iT\Delta t/\hbar} e^{-iV\Delta t/(2\hbar)}. \tag{1.33}$$

This factorisation makes it efficient to alternate between position- and momentum-space representations of the wavefunction using fast Fourier transforms (FFTs) [39]. In practice, the split-operator method allows direct grid-based propagation of the nuclear wavepacket, giving numerically exact results for relatively small systems and short timescales [35]. However, for larger molecular systems, the method becomes prohibitively expensive, since the grid size grows exponentially with the number of degrees of freedom, making both the memory requirements and computational cost intractable.

1.4.3 MCTDH

To reduce the computational cost of grid-based methods while retaining a fully quantum description, the Multi-Configuration Time-Dependent Hartree (MCTDH) approach stands out as one of the most versatile and accurate techniques [40–42]. By employing a more manageable basis, MCTDH enables exact simulations that would otherwise be intractable with direct-product grids. It provides a fully quantum-mechanical description of nuclear motion by solving the time-dependent Schrödinger equation (TDSE) for multiple degrees of freedom simultaneously. The method is particularly effective for systems described by vibronic coupling models or involving conical intersections, where strong non-adiabatic effects are present. The method expands the

nuclear wavefunction as a linear combination of time-dependent products of single-particle functions (SPFs) [43]:

$$\Psi(q_1, q_1, ..., q_f, t) = \sum_{j_1=1}^{n_1} ... \sum_{j_f=1}^{n_f} A_{j_1 ... j_f}(t) \prod_{k=1}^{f} \varphi_{j_k}^{(k)}(q_k, t), \tag{1.34}$$

where q_k are the nuclear coordinates, $A_{j_1 ... j_f}(t)$ are the time-dependent extension coefficients, and $\varphi_{j_k}^{(k)}(q_k, t)$ are the SPFs associated with each degree of freedom. Inserting this ansatz into the Dirac–Frenkel variational principle yields coupled equations of motion for both the coefficients and the SPFs. The use of time-dependent SPFs greatly reduces its computational cost compared with exact methods (such as split-operator method), making MCTDH particularly efficient for multidimensional problems while retaining a high degree of accuracy.

MCTDH has become a standard tool for simulating non-adiabatic molecular dynamics, providing numerically exact results for small systems with up to approximately ten degrees of freedom [44–46], and high-precision results for larger systems [47]. However, these simulations are typically limited to short time scales and require pre-computed electronic potential energy surfaces. While these surfaces accurately represent short-time dynamics, their reliability decreases as the nuclear wavepacket evolves far from the initially sampled configurations. To address some of these limitations, the multi-layer extension of MCTDH (ML-MCTDH) [48, 49] allows hierarchical coupling of SPFs, enabling efficient and accurate simulations of larger systems. Nevertheless, the method remains computationally demanding, the optimal wavefunction form cannot be predicted *a priori*, and as a fully quantum treatment methods on classical computers, it has a worst-case exponential-resource scaling with system size. Thus, despite being highly accurate for small to medium systems, its exponential scaling prevents its use for realistic large-scale chemical dynamics.

1.5 Quantum simulation of chemical dynamics

The limitations of classical methods make it clear that capturing the full complexity of non-adiabatic chemical dynamics requires new strategies. Rather than approximating quantum behaviour with classical resources, quantum simulation offers a different path: it employs a controllable quantum device to reproduce the dynamics of the quantum system directly [6–8, 17, 50], taking advantage of the same quantum mechanical principles that govern the quantum simulator itself. This idea was proposed by Richard Feynman [7] and is particularly useful for chemical problems whose fully quantum description can demand exponential scaling, making accurate classical simulations intractable.

Quantum simulation can be broadly divided into two paradigms: digital and analog. Digital, or qubit-only, approaches encode the molecular degrees of freedom into qubits and reproduce

their dynamics through sequences of quantum gates [5, 8]. While this strategy is universal—any system can be simulated given an algorithm—and ultimately compatible with fault-tolerant quantum computing, present-day devices remain constrained by limited qubit numbers, gate errors, and short coherence times, restricting applications to proof-of-principle studies of small systems. By contrast, analog simulation reproduces the molecular dynamics directly by using the native degrees of freedom of the hardware. Specifically, the MQB approach [11] employs qudits (d-level system) to represent electronic states and bosonic modes to encode vibrations, thereby avoiding the costly mapping of vibrational degrees of freedom onto qubits ($d = 2$). This resource efficiency makes the MQB approach especially well suited for simulating non-adiabatic molecular dynamics.

In the following, we discuss these two paradigms in more detail. First, we review qubit-only methods, previous attempts to simulate chemical dynamics, and the challenges that currently prevent them from scaling. We then introduce the MQB approach, with a focus on trapped-ion architectures, which are used for experimental realisations in this thesis.

1.5.1 Digital simulation

Digital quantum simulation is the most widely developed approach to quantum simulation [5, 6, 8, 50–52]. As in classical computers, most quantum simulation approaches are built from basic memory units–quantum bits, or qubits. Unlike a classical bit, which can only take the values 0 or 1, representing the qubit states $|0\rangle$ and $|1\rangle$, respectively. A general qubit state can exist in a superposition of both states,

$$|\psi\rangle_q = c_0 |0\rangle + c_1 |1\rangle , \tag{1.35}$$

with $|c_0|^2 + |c_1|^2 = 1$. A quantum processor with n qubits can therefore represent 2^n basis states simultaneously [5], reducing the exponential memory requirements on classical computers to a linear scaling with qubit number.

In this approach, the simulator encodes the degrees of freedom of a target system into registers of qubits and reproduces its dynamics through sequences of elementary quantum gates [5]. Because qubits can be manipulated using a universal set of single- and two-qubit operations, any physical system can in principle be simulated with arbitrary accuracy, provided that a suitable algorithm is devised and sufficient resources are available. This universality makes digital simulation a cornerstone of long-term visions for quantum computing, including applications in chemistry.

A variety of algorithms have been proposed for quantum chemistry on digital quantum computers, although most efforts have focused on electronic structure problems involving time-independent variables. Examples include quantum phase estimation (QPE) [53–55] and the

variational quantum eigensolver (VQE) [56–58], both of which have been applied to ground-state energy estimation. Despite their favourable scaling—linear in the number of qubits and polynomial in the number of gate operations with system size [53]—these methods have so far been restricted to very small molecules, such as H_2 [53, 56, 58], LiH [54, 56], BeH_2 [57] and H_2O [54], owing to current device limitations in qubit counts and coherence times. The largest chemistry calculation to date, using a state-of-the-art superconducting processor assisted by a supercomputer, has simulated the ground-state dissociation of N_2 as well as the ground-state properties of $[2\,\mathrm{Fe}-2\,\mathrm{S}]$ and $[4\,\mathrm{Fe}-4\,\mathrm{S}]$, employing 77 qubits and $10,570$ gates [59].

Quantum computers offer efficient simulation alternatives. Qubit-only simulators have universal applicability, since any quantum system can be simulated efficiently on a quantum computer [8, 60]. However, applying them to molecular dynamics involves continuous variables that must be discretized and encoded into qubits [61–66]. This mapping introduces substantial overhead in the number of qubits and the circuit size of quantum simulations. Nevertheless, qubit-only platforms carry the long-term prospect of fault-tolerant implementation because error-corrected qubits can execute deep circuits with controlled accuracy.

Quantum algorithms for the simulation of chemical dynamics provide numerically exact results with polynomial resource scaling [61–64]. However, the number of qubits and quantum gates required per time step to outperform classical methods already exceeds the capabilities of state-of-the-art devices [61–63], restricting these algorithms to small molecules. Recent estimates for chemical dynamics of a four-state model of an anthracene–fullerene interface indicate the need for 117 qubits and 1.5×10^7 Toffoli gates [66], even after reducing the dimensionality to 11 vibrational modes. These results showcase the potential of digital methods, but also highlight the steep resource gap between today's noisy intermediate-scale quantum (NISQ) hardware and the fault-tolerant quantum computers required for chemically realistic simulations.

Ultimately, fault tolerance is essential for the scalability of digital quantum simulation [5]. By encoding logical qubits into error-correcting codes, it becomes possible to suppress decoherence and gate errors to arbitrarily low levels, at the cost of significant hardware overhead [67, 68]. Estimates suggest that millions of physical qubits may be required to perform accurate digital simulations of medium-sized molecules under fault-tolerant protocols [69]. While this goal remains distant, digital simulation continues to provide a crucial theoretical framework, guiding algorithmic development and resource estimation for the future of quantum chemistry.

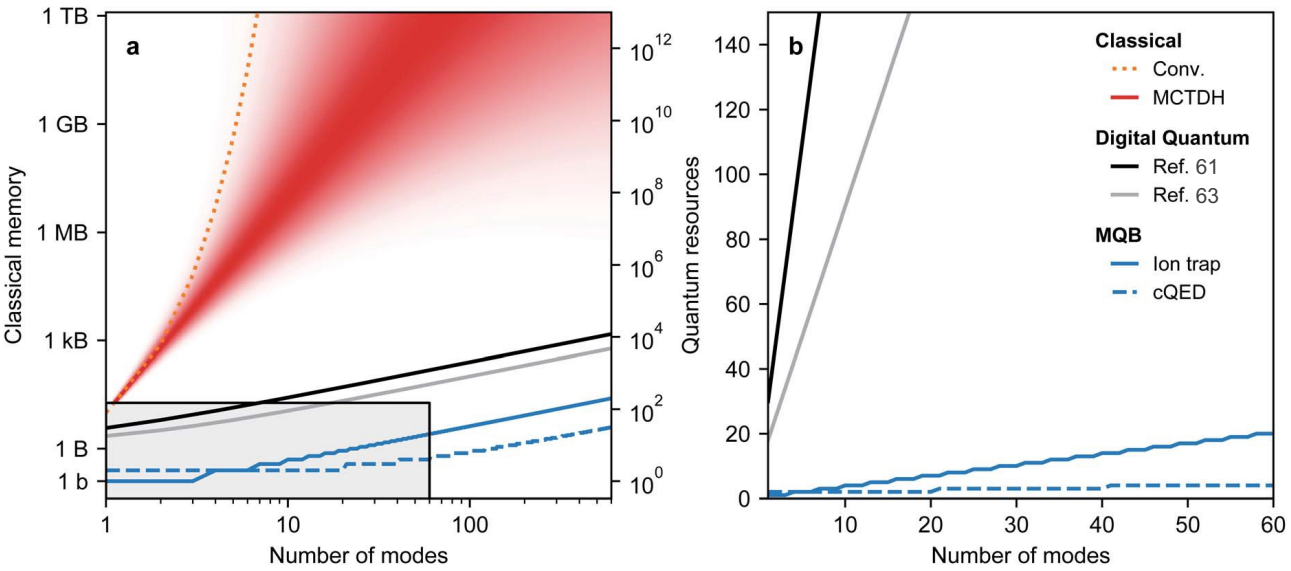

Figure 1.4: Resource requirements as a function of molecular size (number of vibrational modes) for simulating vibronic Hamiltonian dynamics using classical and quantum approaches. **a.** Memory requirements for classical methods and quantum simulation, shown in bits (b), bytes (B = 8b), and quantum resources (qubits). **b.** Qubits requirements for quantum approaches (zoom-in of the grey box in panel a), illustrating their linear scaling. Figure modified from [11].

1.5.2 Analog simulation using the mixed-qudit-boson approach

Analog quantum simulators [50, 70–72] provide an alternative to universal, gate-based quantum computation. Instead of decomposing molecular dynamics into a sequence of qubit gates, an analog simulator is constructed so that its Hamiltonian matches that of the system of interest. Once this mapping is established, the simulator naturally evolves in time in the same way as the target system, and molecular observables can be retrieved directly from measurements of the simulator. This direct correspondence between Hamiltonians as already been successfully applied in qubit-based simulators for spin models [73, 74] and in ultracold atom platforms for simplified molecular systems [75].

For chemical applications, bosonic degrees of freedom are particularly valuable because they provide a natural representation of molecular vibrations. Architectures such as photonic chips, microwave resonators, and trapped ions natively host bosonic modes, avoiding the costly qubit overhead required to encode oscillators digitally. The mixed-qudit–boson (MQB) framework [11] takes advantage of this for chemical dynamics simulation; it maps electronic states onto qudits and vibrational modes onto bosonic modes, providing a resource-efficient representation of vibronic coupling Hamiltonians. Indeed, bosonic simulators have already been applied to vibrational dynamics [76, 77] and Franck–Condon spectra [78–80], while approaches entangling bosonic modes with discrete states enable the simulation of more complex processes, including electron–nuclear dynamics, charge transfer, and exciton transport [81–83].

The formal basis for this mapping can be seen by comparing the vibronic coupling Hamiltonian of eq. (1.13) with the MQB Hamiltonian. Usually, MQB architectures use a combination of light-matter interactions to achieve full control over their devices, making it common to describe their Hamiltonian in the interaction picture. To make the molecule-MQB mapping evident, we start by expressing the simplest VC Hamiltonian (LVC model eq. (1.19)) in the interaction picture [11],

$$H_{\mathrm{LVC}}^{\mathrm{I}} = \sum_{n,m}^{d} \sum_{j=1}^{N} \frac{c_j^{(nm)}}{\sqrt{2}} |n\rangle \langle m| \left(a_j^\dagger e^{i\omega_j t} + \mathrm{h.c.} \right) + \sum_n E_n |n\rangle \langle n| . \tag{1.36}$$

Here, bosonic operators satisfy $Q_j = (a_j^\dagger + a_j)/\sqrt{2}$ and

$$c_j^{(nm)} = \begin{cases} \lambda_j^{(nm)} & \text{if } n \neq m, \\ \kappa_j^{(n)} & \text{if } n = m. \end{cases}$$

The system is composed of d electronic states coupled to N vibrational modes.

Several physical architectures can be used to implement MQB simulations, provided they supply qudit states, bosonic modes, and controllable couplings between them. Examples of such systems are circuit quantum electrodynamics (cQED) [84–86], and trapped ions [87–91]. Trapped-ion systems support multiple motional modes that naturally map onto vibrational coordinates, while the ion's internal electronic states provide qudits. Likewise, cQED architectures—usually superconducting circuits coupled to microwave resonators—allow microwave resonators to host many bosonic modes, enabling simulations of molecules with a large number of vibrational degrees of freedom. An MQB analog simulator can implement an equivalent Hamiltonian to eq. (1.36) [11],

$$H_{\mathrm{MQB}} = \sum_{n \neq m} \sum_{j=1} \Omega_{n,m,j} |n\rangle \langle m| \left(a_j^\dagger e^{i\delta_j t} + \mathrm{h.c.} \right) + \sum_n \sum_{k=1} \Theta_{n,k} |n\rangle \langle n| \left(a_k^\dagger e^{i\delta_k t} + \mathrm{h.c.} \right) + \sum_n \chi_n |n\rangle \langle n| , \tag{1.37}$$

where each parameter $\{\Omega_{n,m,j}, \Theta_{n,k}, \chi_n\}$ corresponds to a physically tunable interaction in the simulator. The structural similarity of the two Hamiltonians means that MQB simulators can reproduce vibronic dynamics directly, with tunable parameters allowing flexible modelling of a broad range of molecular systems.

The efficiency of MQB simulators compared to both classical and digital approaches, is reflected in their scaling properties. The number of qudit states and bosonic modes required scales linearly with the number of electronic states and vibrational modes in the target molecule [11]. This linear scaling contrasts with the exponential scaling of classical simulations and a the steeper scaling of digital quantum approaches [11]. As shown in fig. 1.4, simulating a molecular system with ten vibrational modes would require approximately 80 qubits and complex interactions between them in a digital approach, whereas an MQB simulator would need only four ions

in a trapped-ion architecture and a single microwave resonator in cQED. Importantly, the experimental difficulty of implementing a controllable bosonic mode is often comparable to that of a qubit, making bosons a cost-effective resource.

In the following, we describe the trapped-ion architecture in detail, highlighting how its physical degrees of freedom and control toolbox naturally implement the MQB framework and make it a particularly powerful platform for simulating chemical dynamics.

Trapped-ion architectures

Trapped ions represent one of the most mature and versatile architectures for quantum computing [51, 70, 92], with applications ranging from universal digital simulation based on qubits and gate operations to analog simulation frameworks that exploit qudits and bosonic modes.

The description presented here is tailored to the requirements of trapped-ion platforms for MQB simulation of chemical dynamics. It outlines how trapped-ion systems encode electronic and vibrational degrees of freedom and how sideband couplings simulate the essential electron–vibration interactions found in molecular systems. The subsequent chapters of this thesis, including both experimental demonstrations and theoretical proposals, are built upon this architecture.

Internal degrees of freedom as qudits

The internal degrees of freedom of a trapped ion correspond to its electronic structure, which is naturally quantised into discrete energy levels. These levels vary depending on the element and isotope, and provide the basis for trapped-ion quantum information processing. By selecting and controlling transitions between suitable levels, one can encode quantum information and use ions as carriers of qubits or more general multilevel qudits.

In the simplest case, a two-level system (a qubit) is defined by choosing two long-lived electronic states to represent the logical $|0\rangle$ and $|1\rangle$. Different trapped-ion species offer distinct physical realisations of such states. For instance, in $^{171}\mathrm{Yb}^{+}$ (see fig. 1.5d), hyperfine levels within the $^{2}\mathrm{S}_{1/2}$ ground state are used: the $|0\rangle = |^{2}S_{1/2}, F = 0\rangle$ and $|1\rangle = |^{2}S_{1/2}, F = 1\rangle$ states form a robust qubit basis, with coherence times on the order of seconds [93–95]. By contrast, in ions such as $^{40}\mathrm{Ca}^{+}$, an optical qubit is implemented using a transition between the ground state $^{2}\mathrm{S}_{1/2}$ and a metastable excited state $^{2}\mathrm{D}_{5/2}$ [96, 97]. These optical qubits allow fast gate operations but typically require more demanding laser stability.

For simulation of molecular systems, it is often useful to extend beyond two levels. Trapped ions can support qudits, where multiple internal states are employed to represent the electronic structure of a molecule. In $^{171}\mathrm{Yb}^{+}$, for example, several hyperfine and Zeeman sublevels, such as $|^{2}S_{1/2}, F = 1, M_F = \pm 1\rangle$ can be accessed and coherently manipulated with microwave or laser

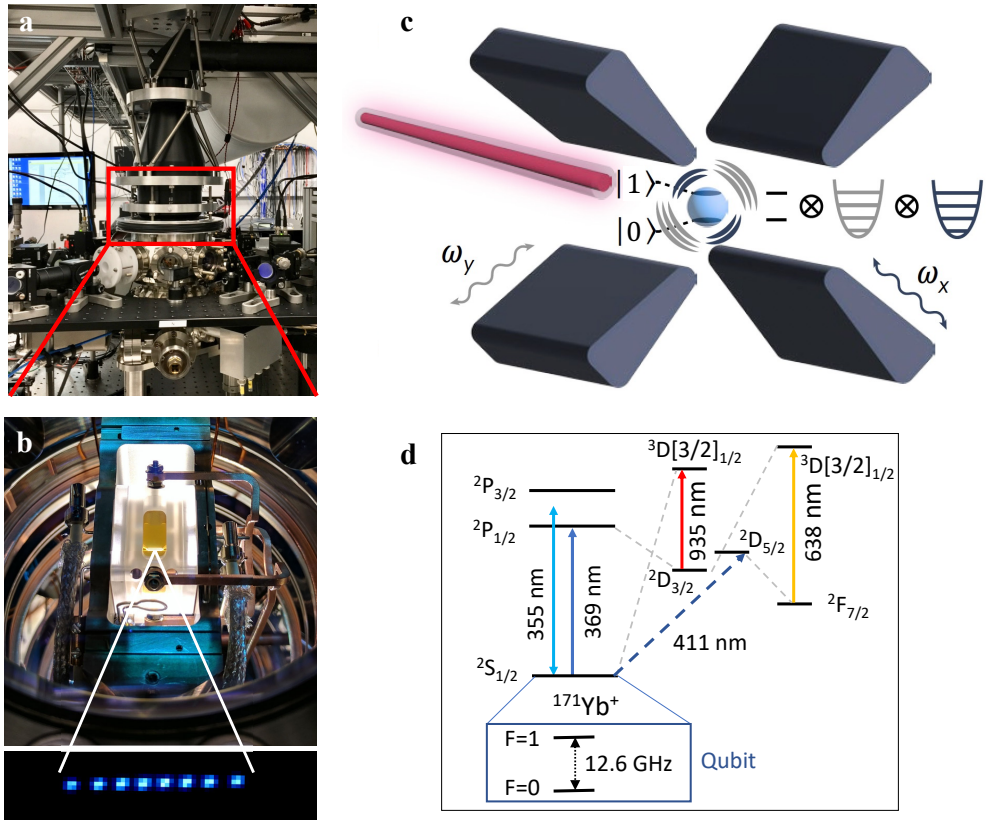

Figure 1.5: Paul trap experimental set-up and electronic structure of the trapped ion $^{171}Yb^+$ at the Quantum Control Laboratory, University of Sydney. **a.** External view of the linear ion trap. The red rectangle indicates the region shown in **b.** Top view of the trap, where ions are confined using a combination of AC and DC electric fields. **c.** Schematic representation of the interior of the trap, showing the blades (electrodes) that create the trapping potential along the x- and y-axes. The internal transition highlighted corresponds to the qubit system for this ion species. **d.** Internal electronic structure of the ion $^{171}Yb^+$, showing the hyperfine levels employed for the qubit system and other auxiliary states used to drive carrier and sideband transitions. Images (a) and (b) courtesy of the Quantum Control Laboratory, University of Sydney. Panel (c) modified from [99].

fields [88, 98], enabling a direct mapping between the ion's internal states and the diabatic electronic states of a molecular Hamiltonian.

Motional degrees of freedom as bosonic modes

In a trapped-ion quantum simulator, the motional degrees of freedom correspond to the quantised motion of ions confined by electric fields. In the experiments presented in this thesis, confinement is achieved with a Paul (linear) trap, which combines static and oscillating electric fields to create an effective three-dimensional potential [88].

A Paul trap employs four cylindrical electrodes arranged radially (see fig. 1.5c), together with two electrodes aligned along the axis of the trap. A DC voltage applied to the axial electrodes generates a static harmonic potential that confines the ion along the z-direction. Radial confinement is realised by applying a radio-frequency (RF) voltage to a pair of diagonally opposite blades, while grounding the other pair. The superposition of the DC and RF fields produces a

time-averaged pseudopotential: near the trap centre this potential is well approximated by a harmonic oscillator along each direction, so that the ion undergoes harmonic motion in three dimensions [87, 88, 90, 100].

By laser cooling [101–103], the ions can be brought close to their motional ground state, at which point their motion is accurately described by the quantum harmonic oscillator model [101–103]. Excitations are quantised into phonons, with Fock states $|n\rangle$ in each mode, corresponding to discrete vibrational quanta. This establishes the ion's motion as a bosonic degree of freedom, which can be exploited to encode molecular vibrations.

When multiple ions are trapped in a chain, they no longer oscillate independently but share collective normal modes of motion. A chain of N ions supports $3N$ such modes: N axial and $2N$ radial. Radial modes generally experience tighter confinement (smaller trapping frequencies) than axial modes, which means that the coupling to the internal degrees of freedom can be tuned with higher accuracy [104]. This is crucial for the manipulation and measurement of the ions. Thus, radial modes are typically preferred for simulating molecular vibrations [105–107].

This architecture provides a natural mapping between the motional modes of trapped ions and the vibrational modes of a molecule. In practice, a molecule with N vibrational modes can be represented by a linear chain of $N/2$ trapped ions, with the radial modes mapping the molecular vibrations.

Couplings between qudits and bosonic modes

The full power of trapped-ion platforms for quantum simulation arises from the ability to couple the ions' internal electronic states (qudits) to their quantised motional modes (bosons). This coupling is achieved through the interaction of the trapped ions with external laser fields. In this sense, the light–matter interaction in trapped ions provides a close analog to the vibronic coupling in molecular systems, where electronic and vibrational degrees of freedom are strongly correlated.

For simplicity, we first consider the interaction of a single trapped ion and one of its motional modes with an external laser field, which is near resonant to an internal transition of the ion. The internal states are usually represented with a qubit system $|0\rangle$ and $|1\rangle$. We will follow the description provided in ref. [56].

The Hamiltonian of the free ion is

$$H_0 = \frac{\hbar\omega_t}{2}\sigma_z + \hbar\omega_t\left(a^\dagger a + \frac{1}{2}\right), \tag{1.38}$$

where $\hbar\omega_0$ is the energy splitting of the internal transition, $\sigma_z = |0\rangle\langle 0| - |1\rangle\langle 1|$ is the Pauli z-operator, and ω_t is the ion's motional frequency in the trapping potential. The natural linewidth of the internal transition must satisfy $\Gamma \ll \omega_t$ to ensure that the motional sidebands are spectrally resolved.

The interaction Hamiltonian between the ion and the laser is

$$H_{\text{ion-laser}}(t) = \frac{\hbar\Omega}{2}(\sigma_+ + \sigma_-)\left(e^{i\eta(a+a^\dagger)}e^{-i(\omega_l t-\phi_l)} + e^{-i\eta(a+a^\dagger)}e^{i(\omega_l t-\phi_l)}\right), \tag{1.39}$$

where Ω is the Rabi frequency (with $\Omega \ll \omega_t$, operating in the resolved-sideband limit), ω_l and ϕ_l are the laser frequency and phase, and $\sigma_\pm$ are the raising and lowering operators of the qubit. The parameter

$$\eta = k\sqrt{\frac{\hbar}{2m\omega_t}}\,\cos\theta \tag{1.40}$$

is the Lamb-Dicke factor, defined as the ratio between the ground-state wavepacket size of the ion and the laser wavelength $\lambda = 2\pi/k$; here, θ is the angle between the laser wave-vector and the ion's direction of motion.

To simplify eq. (1.39), we transform it to the interaction picture with respect to H_0, in which rapidly oscillating terms can be neglected. We also make the Lamb–Dicke approximation, $\eta^2(2\bar{n}+1) \ll 1$, where $\bar{n}$ is the mean phonon number in the harmonic oscillator and $\eta \ll 1$, meaning the ion's motion is much smaller than the laser wavelength. Typically $\bar{n} < 20$, thus terms of order $\mathcal{O}(\eta^2)$ or higher can be neglected in the Taylor expansion of $e^{i\eta(a+a^\dagger)}$. This yields

$$H_{\text{int}}(t) = \frac{\hbar\Omega(n)}{2}\left(e^{-i(\Delta t-\phi_l)}\sigma_+\left\{\mathbf{1} + i\eta\left(ae^{-i\omega_t t} + a^\dagger e^{i\omega_t t}\right)\right\} + \text{h.c.}\right), \tag{1.41}$$

where $\Delta = \omega_l - \omega_0$ is the laser detuning and the Rabi frequency now have frequency components $\Omega(n)$ depending on the motional state n [56]. Applying a second rotating-wave approximation (removing terms oscillating at ω_t) leaves three relevant cases:

- **Carrier transition:** $\Delta = 0$. The laser drives the internal transition without changing the motional state.
- **Red sideband:** $\Delta = -\omega_t$. The laser couples $|0,n\rangle \leftrightarrow |1,n-1\rangle$, simultaneously exciting the internal state and removing one phonon.
- **Blue sideband:** $\Delta = \omega_t$. The laser couples $|0,n\rangle \leftrightarrow |1,n+1\rangle$, simultaneously exciting the internal state and creating one phonon.

Therefore, by tuning the laser frequency to the carrier, red or blue sidebands, one can induce transitions that change both the ion's internal state and its motional state. These interactions give rise to the terms in eq. (1.37), for example, $\Omega_{n,m,j} = \eta\Omega(n)/2$ is the light-matter coupling strength produced when the red and blue sidebands are applied simultaneously. Similarly, $\Theta_{n,k} = \eta\Omega(n)/2$ when the laser is tuned near the motional frequency, and $\chi_n = (1-\eta^2)\Omega(n)/2$ is the light-matter coupling of the carrier transition. These expressions may become more complicated if additional laser tones are required to drive the system near the qubit transition, as is the case for hyperfine qubits (see [91]). Therefore, these interactions are the fundamental mechanisms for reproducing electron–vibration interactions within the trapped-ion system.

In practice, more advanced laser configurations such as Mølmer–Sørensen interactions [89, 108, 109] allow two-qubit entangling operations. These interactions are produced with an acoustic-optical modulator (AOM), driving many transitions simultaneously, and creating couplings of multiple ions and modes. This enables the implementation of collective Hamiltonians relevant to multi-state, multi-mode molecules. This versatility makes the trapped-ion platform particularly powerful for simulating vibronic coupling Hamiltonians.

Thus, the coupling between internal and motional degrees of freedom provides the essential link that allows trapped ions to function as MQB simulators. Molecular electronic states are encoded in the ion's qudit levels, vibrational modes are mapped to phonons, and their coupling is mediated by laser-driven sideband transitions. This mapping realises the core of the MQB framework used in this thesis.

1.6 Thesis outline

The goal of this thesis is to overcome the main challenges that have so far prevented the adoption of MQB simulation as a standard method for simulating non-adiabatic dynamics. First, no previous simulation had addressed a chemically meaningful problem. Second, the main limitation of MQB simulation lies in the accumulation of errors due to dissipation and its restriction to closed-system dynamics. Third, because MQB simulators are purpose-built devices, they may appear to be restricted to a narrow class of molecular processes. Fourth, the claim that MQB simulators require fewer quantum resources than qubit-only approaches had not previously been quantified beyond simple degree-of-freedom counting.

The following chapters address these limitations in turn. Chapter 2 demonstrates the practical utility of MQB simulators through the first application to a chemically relevant non-adiabatic process. Chapter 3 extends the framework to open-system dynamics, showing how intrinsic noise can be harnessed as a resource and enabling longer simulations under realistic environmental conditions. Chapter 4 shows the programmability of MQB devices, where coherent and dissipative processes in photochemistry are included for multiple molecular systems. Finally, Chapter 5 quantifies the resource efficiency of MQB simulators compared with qubit-only approaches, introducing a systematic framework to evaluate memory requirements, gate operations, and error accumulation. Together, these results transform MQB simulation from a theoretical proposal into a validated, programmable, and resource-efficient platform for quantum simulation of chemical dynamics.

In Chapter 2, we establish the viability of the MQB approach through a proof-of-principle experiment that addresses a long-standing challenge in chemical dynamics: the first direct observation of geometric-phase interference in a quantum system. Molecular dynamics evolving

around conical intersections can experience quantum interference between wavepackets due to geometric-phase accumulation, affecting reaction outcomes. Indirect signatures of this interference have been measured, but its unambiguous detection has remained elusive. Using a trapped-ion device, we engineered the Jahn–Teller Hamiltonian, leveraging the electronic and motional degrees of freedom to reproduce the characteristic conical intersection of this model. By allowing the system to evolve around the intersection and applying a full wavepacket reconstruction technique, we directly observed the destructive self-interference pattern in the probability density. This experiment highlights the utility of MQB platforms in providing practical insights into complex chemical systems.

In Chapter 3, we propose a framework that uses the intrinsic noise of the simulator as a resource for simulation of open-system molecular dynamics. This is a fundamental step toward modelling realistic chemical environments where dissipation and decoherence play a central role. Building on the closed-system framework explained in the previous section, we extend the MQB approach to include open-system dynamics, by leveraging the native dissipation of the simulator as a useful resource, we show that longer simulation times can be reached compared to closed-system implementations. Additionally, we propose to inject controllable dissipation—implemented with minimal additional resources—to further enhance the flexibility of the platform. The system dynamics are described within the Lindblad formalism, incorporating the most relevant dissipative processes found in chemical systems: pure electronic and vibrational dephasing as well as electronic and vibrational population decay. This framework significantly broadens the range of chemical environments that can be explored, enabling simulations of a wide variety of condensed-phase processes.

In Chapter 4, we demonstrate that MQB simulators provide a viable near-term platform for quantum simulation by carrying out the first programmable quantum simulations of chemical dynamics on a MQB device. Our platform captures the strongly non-adiabatic dynamics that remain among the most challenging for classical computation. We establish the versatility of this approach by simulating the dynamics of multiple molecular systems—including conical-intersection models and photochemical processes—as well as extending to open-system dynamics through engineered dissipation. These results highlight the ability of MQB devices to reproduce both coherent and dissipative chemical phenomena within a single experimental framework, marking a step toward quantum simulators capable of addressing problems inaccessible to either classical methods or qubit-only quantum simulation.

In Chapter 5, we rigorously demonstrate the exceptional resource efficiency of the MQB approach, which is likely to achieve quantum advantage in the simulation of chemical dynamics sooner than qubit-only methods. To quantify this efficiency, we developed a systematic framework that evaluates the quantum resource requirements for both qubit-only and MQB-based

simulations to reach a target fixed accuracy when simulating non-adiabatic dynamics. This framework considers two factors: the memory needed to encode quantum information and the simulation time needed to perform operations on the respective platforms. We find that MQB simulations require at least five orders of magnitude fewer entangling operations for closed-system dynamics, and a million-fold improvement for open systems. These results make evident the efficiency of MQB approach when simulating bosonic degrees of freedoms compared to qubit-only methods.

Chapter 6 concludes by situating these advances within the broader trajectory of MQB simulation. We discuss the remaining challenges, particularly scalability and sensitivity to noise, while highlighting how the progress reported in this thesis overcomes the most immediate barriers to demonstrating the value of MQB simulators for chemistry.

Chapter 2: Direct observation of geometric-phase interference in dynamics around a conical intersection

This chapter is a reformatted version of the publication:
C. H. Valahu, V. C. Olaya-Agudelo, R. J. MacDonell, T. Navickas, A. D. Rao, M. J. Millican, J. B. Pérez-Sánchez, J. Yuen-Zhou, M. J. Biercuk, C. Hempel, T. R. Tan and I. Kassal, "Direct observation of geometric-phase interference in dynamics around a conical intersection", *Nat. Chem.* **15**, 1503–1508 (2023).

Abstract

Conical intersections are ubiquitous in chemistry and physics, often governing processes such as light harvesting, vision, photocatalysis, and chemical reactivity. They act as funnels between electronic states of molecules, allowing rapid and efficient relaxation during chemical dynamics. In addition, when a reaction path encircles a conical intersection, the molecular wavefunction experiences a geometric phase, which can affect the outcome of the reaction through quantum-mechanical interference. Past experiments have measured indirect signatures of geometric phases in scattering patterns and spectroscopic observables, but there has been no direct observation of the underlying wavepacket interference. Here, we experimentally observe geometric-phase interference in the dynamics of a wavepacket travelling around an engineered conical intersection in a programmable trapped-ion quantum simulator. To achieve this, we develop a new technique to reconstruct the two-dimensional wavepacket densities of a trapped ion. Experiments agree with the theoretical model, demonstrating the ability of analog quantum simulators—such as those realised using trapped ions—to accurately describe nuclear quantum effects. These results demonstrate a path to deploying analog quantum simulators for addressing some of the most difficult problems in chemical dynamics.

2.1 Introduction

Light drives molecular processes as important as photosynthesis, photocatalysis, and vision. Absorbing a photon promotes a molecule to an excited electronic state, triggering chemical dynamics and reactivity. The molecule will eventually return to the ground state; often, this relaxation happens on ultrafast (fs–ps) timescales at molecular geometries where two electronic energy surfaces have the same energy, known as conical intersections [1, 2, 110]. By acting as funnels between electronic states for the molecular wavefunction, conical intersections enable rapid non-radiative electronic transitions and have a decisive role in chemical dynamics, from charge-transfer processes to photochemical reactions [111].

The path taken during molecular dynamics involving conical intersections can profoundly alter chemical reaction outcomes. In particular, a geometric phase [112] causes quantum interference of wavepackets encircling a conical intersection [13, 113–115]. Accounting for geometric phase is necessary in quantum chemistry calculations because the resulting interference changes the ratio of reactive and non-reactive outcomes in scattering cross-sections [116–119] and alters vibrational spectra [120–122]. Indeed, recent experiments have detected indirect signatures of geometric phase in reactive scattering [123, 124]. An elegant proposal for revealing spectroscopic signatures of geometric phase involves interference signals from pairs of excitation pulses [125–127], but it remains unimplemented due to challenging state preparation.

Conical intersections and the associated geometric phase are general phenomena that also appear in other branches of physics [110]. In general, a conical intersection can form in any parameter-dependent quantum system where two energy surfaces cross. In molecules, the parameters are usually the normal modes of nuclear motion, but, in condensed-phase systems, conical intersections commonly arise as Dirac cones in reciprocal (momentum) space [110]. These include the Dirac cones in graphene [128], in superconductors [129], and in the Rashba [130] and Dresselhaus [131] treatments of spin-orbit coupling.

An unambiguous observation of geometric-phase interference in wavepacket dynamics around a conical intersection remains an outstanding challenge. In a molecular or solid-state system, it would require a full reconstruction of the wavepacket dynamics on ultrafast timescales, which is possible in small molecules [132], but has never been used to characterise geometric phase.

Analog quantum simulators present a new opportunity to access quantum dynamics on laboratory-accessible timescales [50, 71, 133–135]. In such systems, a one-to-one correspondence between the degrees of freedom of the chemical or physical system and those of the simulator makes it possible to replicate the target dynamics in a controllable and measurable manner, as well as explore new parameter regimes in a controllable fashion.

Several controllable quantum systems have been proposed to engineer conical intersections

and study signatures of geometric phase. Most of these quantum simulations have been performed in reciprocal space to simulate solid-state systems, including geometric phases around Dirac points [110, 136, 137]. Theoretical proposals for simulating molecular conical intersections have included using trapped Rydberg ions to simulate electronic populations [138], circuit quantum electrodynamics to simulate emission spectra [139], and cavity quantum electrodynamics to simulate collapse-revival characteristics of a spreading wavepacket [140]. To date, the only experimental quantum simulation of a chemical conical intersection demonstrated branching between different photochemical reaction products with strong dissipation [141].

Here, we present the first observation of the destructive interference caused by geometric phase during dynamics of a wavepacket around a conical intersection. We implement a controllable conical intersection by engineering a Jahn-Teller Hamiltonian in a trapped-ion quantum simulator that employs a mixed-qudit-boson (MQB) encoding in which both the ion's electronic and motional degrees of freedom are used [11]. This work is not merely a simulation of geometric phase: the ion is a real, observable, and measurable quantum system that undergoes conical-intersection dynamics, allowing us to directly observe the geometric-phase interference of its motional wavepacket. To this end, our experiment introduces a resource-efficient reconstruction method to image the wavepacket's probability density, directly showing the destructive self-interference as the wavepacket encircles a conical intersection. Experimental measurements match theoretical predictions, demonstrating the utility of quantum simulators to give insights into properties that have otherwise been impossible to measure directly for chemical systems.

2.2 Model

In an MQB simulator [11], the electronic and vibrational degrees of freedom that are to be simulated are represented in a qudit and a set of bosonic modes. We realise a conical intersection using an $^{171}Yb^{+}$ ion confined in a Paul trap, where two vibrations are encoded directly in the ion's transverse vibrational modes (B_1 and B_2), while two electronic states are encoded in the ion's qubit (qudit with $d = 2$) states comprising the two hyperfine levels of the $^2S_{1/2}$ ground state (detailed in Methods). This approach has recently been employed to predict molecular spectra using time-domain simulations [106], and provides resource-scaling advantages relative to conventional methods of quantum simulation [11].

To demonstrate geometric-phase interference, we implement the $E\otimes e$ Jahn-Teller model [113], a standard model of geometric-phase effects in molecules [115, 142]. It consists of two electronic states coupled with two vibrational modes, described by the potential energy

$$V^{\mathrm{JT}} = \frac{\omega}{2}(Q_1^2 + Q_2^2) + \kappa(\sigma_z Q_1 + \sigma_x Q_2), \tag{2.1}$$

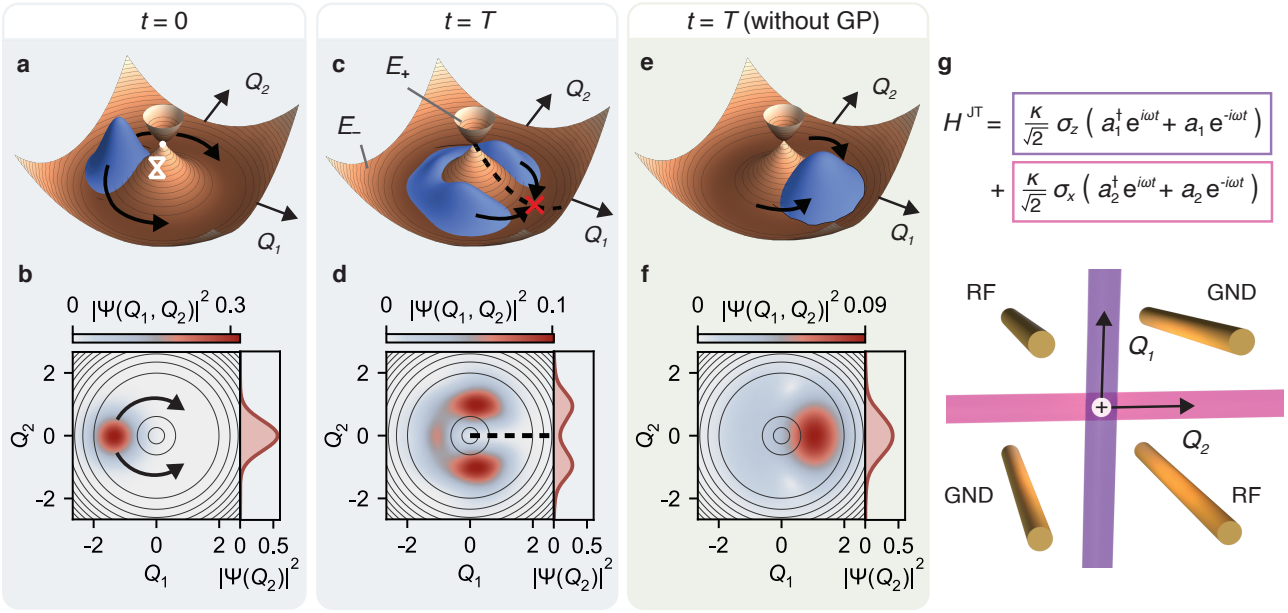

Figure 2.1: **Directly detecting a geometric phase through wavepacket interference. a**, A motional wavepacket is initially displaced to the minimum of the potential energy surface, after which it begins to encircle the conical intersection, denoted ⧖. **b**, Initial wavepacket density in 2D (left), and integrated over Q_1 (right). **c**, After sufficient time evolution, the two components of the wavepacket destructively interfere due to geometric phase, giving a nodal line along $Q_2 = 0$ (dotted line). **d**, Motional wavepacket density at the maximum interference time T. **e**, If the geometric phase were neglected, the two wavepacket components would interfere constructively. **f**, Density at $t = T$ with geometric phase neglected. Contours in b, d, and f correspond to the potential energy surface E_-. **g**, The Jahn-Teller Hamiltonian H^{JT} is engineered in an ion-trap quantum simulator with a single $^{171}\mathrm{Yb}^+$ ion. The ion (white sphere) is confined in a Paul trap and H^{JT} is realised using two simultaneous laser-induced interactions (purple and pink, corresponding to colour-coded terms in H^{JT}).

where σ_x and σ_z are the Pauli matrices acting on the electronic states and $Q_j = (a_j^\dagger + a_j)/\sqrt{2}$ is the dimensionless position coordinate for the jth vibrational mode, with creation and annihilation operators $a_j^\dagger$ and a_j.

κ is the vibronic coupling strength, and ω is the frequency of both vibrational modes. The Jahn-Teller Hamiltonian is given by $H^{\mathrm{JT}} = \omega(P_1^2 + P_2^2)/2 + V^{JT}$, where P_j is the conjugate momentum of Q_j. We set $\hbar = 1$ throughout.

Diagonalisation of V^{JT} in the electronic basis leads to cylindrically symmetric potential energy surfaces along Q_1 and Q_2, with energies $E_\pm = \omega(Q_1^2 + Q_2^2)/2 \pm \kappa\sqrt{Q_1^2 + Q_2^2}$ (see fig. 2.1). The conical intersection is present at the point of highest symmetry ($Q_1 = Q_2 = 0$), where the two potential energy surfaces are degenerate. The minimum of E_- occurs where $Q_1^2 + Q_2^2 = (\kappa/\omega)^2$.

The effects of geometric phase on dynamics around a conical intersection can be directly observed from the motional probability density, fig. 2.1a–d. As the initial wavepacket, we choose the ground state of the non-interacting vibrational Hamiltonian, $H_0 = \omega(a_1^\dagger a_1 + a_2^\dagger a_2)$, displaced to the potential-energy minimum at $Q_1 = -\kappa/\omega$, $Q_2 = 0$ (fig. 2.1a–b). During the time evolution, the wavepacket splits into two components evolving in opposite directions around

the conical intersection. The two components overlap at $Q_1 > 0$, causing destructive interference at the nodal line $Q_2 = 0$, where their equal and opposite geometric phases lead to a vanishing density (fig. 2.1c–d). By contrast, if geometric phase were disregarded, the two wavepacket fragments would interfere constructively, reaching maximum amplitude at $Q_2 = 0$ (fig. 2.1e–f).

2.3 Results

To map the Jahn-Teller model onto the MQB simulator, we rewrite H^{JT} in the interaction picture with respect to H_0,

$$H_{\mathrm{I}}^{\mathrm{JT}} = \frac{\kappa}{\sqrt{2}}\sigma_z(a_1^\dagger e^{i\omega t} + a_1 e^{-i\omega t}) + \frac{\kappa}{\sqrt{2}}\sigma_x(a_2^\dagger e^{i\omega t} + a_2 e^{-i\omega t}), \tag{2.2}$$

which can be implemented using tunable light-atom interactions to enact qubit-boson couplings. We achieve this implementation using a coherent state-dependent force (SDF) enacted by stimulated Raman transitions driven with a 355 nm pulsed laser [143, 144]. Driving transitions near bosonic mode j leads to the Hamiltonian

$$H_{j,\phi_s}^{\mathrm{SDF}}(\delta, \Omega, \phi_m) = \frac{\Omega}{2}\sigma_{\phi_s}(a_j^\dagger e^{i(\phi_m+\delta t)} + a_j e^{-i(\phi_m+\delta t)}), \tag{2.3}$$

where $\sigma_{\phi_s} = \sigma_x \cos\phi_s + \sigma_y \sin\phi_s$ and ϕ_s and ϕ_m are the phases associated with the qubit and the bosonic mode, respectively (see Methods). Ω and δ are the Rabi frequency and detuning of the laser from the bosonic mode, respectively. We use the notation $H_{j,x}^{\mathrm{SDF}}$ and $H_{j,y}^{\mathrm{SDF}}$ for SDF interactions where $\phi_s = 0$ and $\phi_s = \pi/2$, respectively. Interactions in the σ_z basis are obtained using a qubit basis rotation, $H_{j,z}^{\mathrm{SDF}} = R_x(\pi/2)H_{j,y}^{\mathrm{SDF}}R_x(-\pi/2)$, where $R_x(\theta)$ are driven qubit rotations around the Bloch sphere. H^{JT} can then be implemented in a programmable way using two simultaneous SDFs (see fig. 2.1g),

$$H_{\mathrm{I}}^{\mathrm{JT}} = H_{1,z}^{\mathrm{SDF}}(\omega, \sqrt{2}\,\kappa, 0) + H_{2,x}^{\mathrm{SDF}}(\omega, \sqrt{2}\,\kappa, 0). \tag{2.4}$$

The parameters κ and ω are chosen to produce a clear wavepacket interference. To achieve this, κ/ω should be large enough that the wavepacket prepared at the minimum of the potential energy surface (at $Q_1 = -\kappa/\omega$) has negligible overlap with the conical intersection. However, κ/ω should also be kept small enough to mitigate vibrational decoherence that increases with larger vibrational excitations. To balance these considerations, we choose $\kappa/\omega = 1.5$, for which the wavepacket has only 1.7% of the density at $Q_1 \geq 0$. κ, implemented by adjusting the Rabi frequency, is maximised to increase the speed of the dynamics; its value is constrained by the available SDF-laser power to $\kappa = 2\pi \times 1.00\,\mathrm{kHz}$, yielding $\omega = 2\pi \times 667\,\mathrm{Hz}$. With these parameters, the wavepackets are expected to experience the greatest geometric-phase interference at $T = 1.59\,\mathrm{ms}$, which was computationally predicted as half the time at which the width of the probability density is minimized.

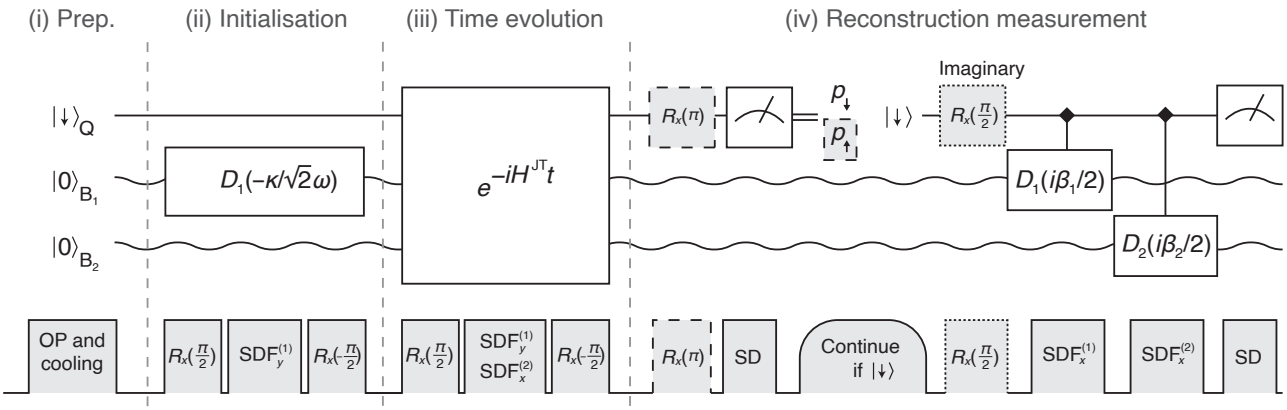

Figure 2.2: **Experimental protocol for geometric-phase dynamics simulation and wavepacket reconstruction. (top)** Quantum circuit diagram for a single-trapped-ion simulator, consisting of a qubit (Q, solid line) and 2 bosonic modes (B_1, B_2, wavy lines), and **(bottom)** corresponding experimental pulse sequence. **(i)** Preparation of fiducial states by optical pumping and cooling. **(ii)** Initialisation: B_1 is displaced by $D_1(-\kappa/\sqrt{2}\,\omega)$, implemented using an SDF pulse with surrounding qubit $\pi/2$ pulses to map to the correct basis. **(iii)** Time evolution under the Jahn-Teller Hamiltonian for duration t, implemented using two simultaneous SDF pulses in different bases, acting on the two bosonic modes. **(iv)** Reconstruction measurement: a state detection (SD) pulse collapses the qubit state, and the circuit proceeds only if the measured state was $|\downarrow\rangle$ (rounded shape). An additional single-qubit pulse (dashed) is introduced to retrieve information entangled with the $|\uparrow\rangle$ state. The qubit probabilities $p_\downarrow$ and $p_\uparrow$ are calculated from the mid-circuit measurement outcomes. Controlled displacements acting in the σ_x basis (denoted ◆) map the motional degrees of freedom onto the qubit, allowing the real part of the characteristic function to be measured. Its imaginary part is obtained using an additional $R_x(\pi/2)$ pulse prior to the controlled displacements (dotted). Successive R_x rotations shown separately in the circuit are combined into a single pulse in the experiment.

We probe the dynamics of the geometric phase around the conical intersection by reconstructing the ion's motional probability densities at different evolution times t. The experimental sequence consists of four stages, shown in fig. 2.2. (i) Preparation of the qubit and cooling of the vibrational modes to their ground states is achieved by optical pumping, Doppler cooling, and sideband cooling. (ii) Initialisation consists of displacing B_1 to $Q_1 = -\kappa/\omega$ by applying an SDF interaction $H^{\mathrm{SDF}}_{1,z}(0, \Omega_1, \pi/2)$ for a duration τ. This applies the displacement operator $D_1(-\Omega_1\tau/2)$, where Ω_1 and τ are chosen to implement $D_1(-\kappa/\sqrt{2}\,\omega)$. (iii) Evolution of the system under H_I^{JT} is achieved by applying the two simultaneous SDF interactions of eq. (2.4) for an experimentally variable duration t. (iv) Reconstruction of the joint densities of B_1 and B_2 is achieved by measuring the characteristic function

$$\chi(i\beta_1, i\beta_2) = \langle\Psi|\, D_1(i\beta_1) D_2(i\beta_2)\, |\Psi\rangle\,, \tag{2.5}$$

where $|\Psi\rangle$ is the total wavefunction of the system, and β_1 and β_2 are real numbers. See Methods for details.

The joint probability densities are reconstructed using the circuit in fig. 2.2. Two SDF pulses are sequentially applied on B_1 and B_2, and $\chi(i\beta_1, i\beta_2)$ is scanned over β_1, β_2. These measurements yield the joint probability density via the Fourier transform of the measured

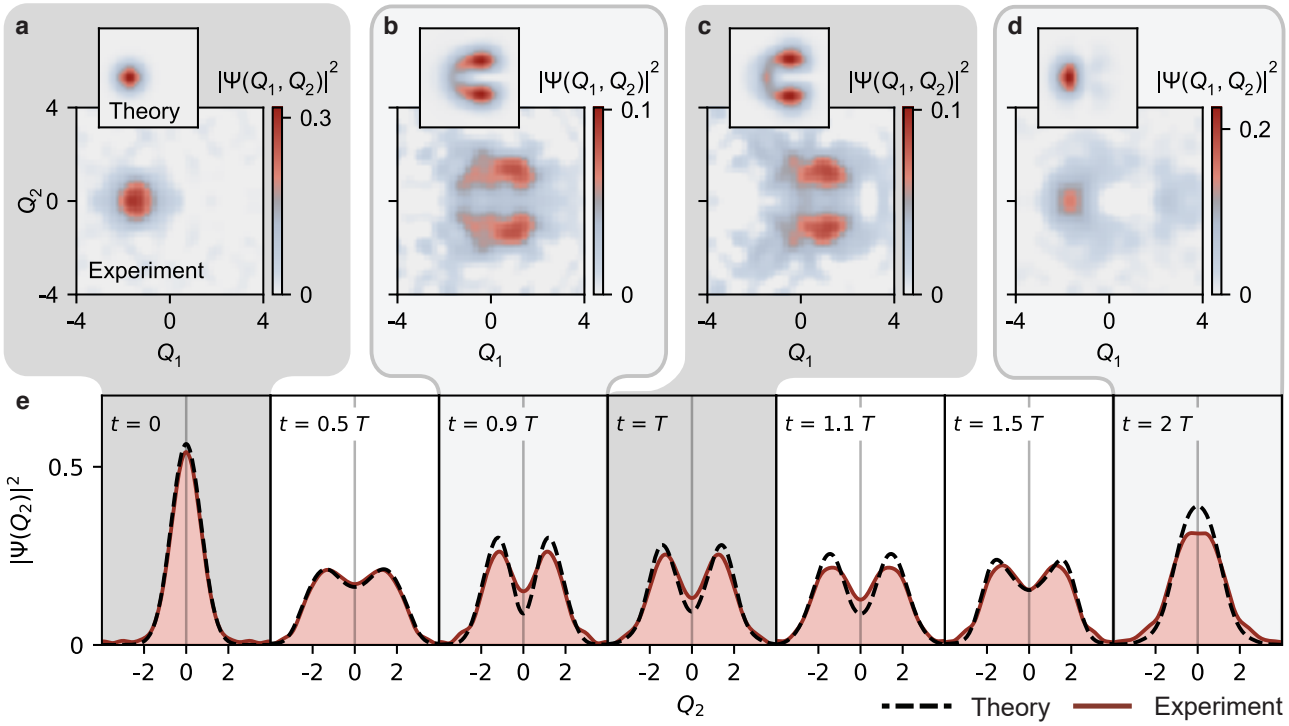

Figure 2.3: **Wavepacket dynamics around an engineered conical intersection. a-d** Reconstructed two-dimensional motional densities of the $^{171}\mathrm{Yb}^+$ ion at times $t = 0$, $0.9T$, T, and $2T$, with theoretical predictions in the insets. The nodal line at $Q_2 = 0$, $Q_1 > 0$ is a direct signature of geometric-phase interference. **e** One-dimensional motional densities (with the Q_1 coordinate integrated out) at more values of t. Geometric-phase interference causes the dip at $Q_2 = 0$ around $t = T$. The motional densities are obtained using eq. (2.5) (and its one-dimensional equivalent) from the characteristic functions, $\chi(i\beta_1, i\beta_2)$ and $\chi(i\beta_2)$, measured using the circuit in fig. 2.2 (see Methods for details).

characteristic function

$$|\Psi(Q_1, Q_2)|^2 = \iint \frac{d\beta_1 d\beta_2}{2\pi^2} e^{-i\sqrt{2}\,(Q_1\beta_1 + Q_2\beta_2)} \chi(i\beta_1, i\beta_2). \tag{2.6}$$

In further detail, we measure $\chi(i\beta_1, i\beta_2)$ by mapping information from the multimode bosonic system onto the qubit using SDF pulses, moving beyond previous works on direct single-mode [100, 145–147] and indirect multimode reconstructions [148]. The reconstruction consists of preparing the qubit in $|\downarrow\rangle$ and applying two successive SDF interactions, $H^{\mathrm{SDF}}_{1,x}(0, \Omega_2, 0)$ and $H^{\mathrm{SDF}}_{2,x}(0, \Omega_2, 0)$ with durations τ_1 and τ_2. Doing so results in controlled displacements $D_1(i\beta_1/2)$ and $D_2(i\beta_2/2)$, where $\beta_j = \Omega_2\tau_j$. $\chi(i\beta_1, i\beta_2)$ is measured for different values of β_1 and β_2 by varying τ_1 and τ_2. We reconstruct the characteristic functions of the bosonic modes entangled with the $|\downarrow\rangle$ and $|\uparrow\rangle$ qubit states independently. Reconstructing the $|\downarrow\rangle$ component is achieved by adding a mid-circuit measurement which projects out the $|\uparrow\rangle$ component (see Methods). The experiment is repeated with an additional $R_x(\pi)$ pulse prior to the mid-circuit measurement to reconstruct the $|\uparrow\rangle$ component. The qubit probabilities $p_\downarrow$ and $p_\uparrow$ are calculated from the success rate of the mid-circuit measurement. After the displacements, measuring the qubit in the σ_z basis gives the real part of the characteristic function, $\langle\sigma_z\rangle = \mathrm{Re}\,\chi(i\beta_1, i\beta_2)$. Repeating the experiment with an additional $R_x(\pi/2)$ pulse prior to the displacements gives the imaginary part,

after which the full $\chi(i\beta_1, i\beta_2)$ is obtained by adding the real and imaginary parts associated with both $|\downarrow\rangle$ and $|\uparrow\rangle$.

The reconstructed probability densities in fig. 2.3a–d demonstrate a direct measurement of the wavepacket interference caused by the geometric phase. At $t = 0$, the initial wavepacket is prepared at $(Q_1, Q_2) = (-1.5, 0)$. As the wavepacket evolves around the conical intersection, the nodal line becomes visible at $Q_2 = 0$ and is most pronounced at $t = T$; this is a direct observation of destructive interference due to geometric phase. Finally, at $t = 2T$, the two wavepackets recombine close to their initial position. The experimental results agree well with theoretical predictions, reproducing key features of interference and wavepacket recombination.

Further quantitative insight may be gained from the 1-dimensional density $|\Psi(Q_2)|^2$, obtained by omitting the $D_1(i\beta_1)$ displacements from the reconstruction procedure above. In this case, the measurements scanned over β_2 are Fourier-transformed to give $|\Psi(Q_2)|^2 = \int d\beta_2\, e^{-i\sqrt{2}\, Q_2\beta_2}\chi(i\beta_2)/\sqrt{2}\,\pi$. In fig. 2.3e, we present $|\Psi(Q_2)|^2$ for seven different evolution times. A comparison of experiment and theory shows excellent agreement in the shape and amplitude of the measured density function. We attribute minor discrepancies to the dephasing of the bosonic modes, miscalibrations such as uncompensated AC Stark shifts, and technical imperfections in the protocol implementation.

2.4 Discussion

Our approach avoids the limitations of direct experiments on molecular systems, where only few observables—such as spectra and scattering cross sections—can be measured. Instead, a fully controllable quantum device—such as an ion-trap MQB simulator [11]—can, in principle, read out any observable; as we showed here, this includes the full two-dimensional density of the $^{171}Yb^+$ ion as it moves in space and time. A further advantage comes from the ratio (r) of the ion's natural timescale (ms) and the measurement speed (ns), leading to an increase in the observable timing resolution of $r \sim 10^6$. This improves the achievable resolution of chemical-dynamics measurements relative to ultrafast observations.

A key general feature of quantum simulations is their programmability [149]. Our work is a simulation of the dynamics of the Jahn-Teller model, which is often used to describe molecular systems. In an MQB simulator, the qudit-boson interaction is controllable, meaning that the same device can be programmed to simulate different molecular systems, solid-state systems, or theoretical models that do not occur naturally. In particular, our geometric-phase simulator could be used to simulate dynamics in molecules with conical intersections where the interactions are not as symmetric as in H^{JT}, such as the general quadratic vibronic-coupling Hamiltonian [11].

Like any analog simulation—quantum or classical—our approach is ultimately limited by noise and uncorrected errors. In our experiment, the main sources of decoherence and dissipation are motional dephasing and motional heating [106, 150] (see Methods). However, in MQB simulations of molecular processes, noise can be characterised and even amplified in order to create a realistic model of molecular environments, such as collisions in solution. Since our Jahn-Teller experiment shows only weak effects of decoherence over the full period $2T$, we would need to inject additional noise to simulate conical-intersection dynamics of real molecules in chemically realistic situations (i.e., other than a single molecule in vacuum). In scaling up to larger molecules, the ability to simulate dissipation would allow us to probe regimes in nonadiabatic dynamics that are among the most difficult to simulate on conventional computers [11].

Our methodology for probability density reconstruction enables scalability and resource efficiency. Early techniques for motional-state tomography were performed in the Fock basis [100, 148, 151], a process that requires many measurements if full motional densities are sought. More recently, wavepacket-reconstruction methods were developed based on the direct measurement of the characteristic function, significantly reducing the number of necessary measurements [147]. Our approach builds on the latter techniques, but has two additional advantages. First, we extend the characteristic-function method to multimode probability density reconstruction, while retaining both the requirement of few measurements and the ability to use one readout qubit. Second, using a mid-circuit measurement allows us to reuse the simulation qubit for the reconstruction, without any ancilla qubits.

We have recently become aware of related simultaneous work on simulating a conical intersection using a chain of trapped ions [107]. The system was adiabatically driven to its ground state, whose reconstructed two-dimensional density showed a node attributed to geometric phase. This work is complementary to ours in several ways: it focused on signatures of geometric phase in the ground state, not in the dynamics; it used Trotterised time evolution, while we drove the two interactions simultaneously; and it used an ancilla qubit in the reconstruction, while we used the mid-circuit-measurement approach above.

In conclusion, our experiment represents the first direct observation of wavepacket interference caused by geometric phase in dynamics around a conical intersection. Our approach to quantum simulation using an MQB trapped-ion system makes chemical dynamics that are otherwise unmeasurable directly accessible in the laboratory. This is a key demonstration of the utility of small-scale quantum computational devices to offer new, practical insights into chemical dynamics and resolve intractable problems in chemical physics.

S1 Methods

S1.1 Experimental setup

The $^{171}Yb^{+}$ ion is confined in a Paul trap with radial mode oscillation frequencies of $2\pi \times 1.34\,\mathrm{MHz}$ and $2\pi \times 1.47\,\mathrm{MHz}$, corresponding to bosonic mode B_1 and B_2. The qubit is encoded in the two magnetically insensitive hyperfine levels of the $^2S_{1/2}$ ground state, where we assign the labels $|\downarrow\rangle = |F = 0, m_F = 0\rangle$ and $|\uparrow\rangle = |F = 1, m_F = 0\rangle$.

We use two laser beams derived from a 355 nm pulsed laser to coherently control the qubit and bosonic modes via stimulated Raman transitions within the $^2S_{1/2}$ ground state. The two Raman beams are orthogonal to one another, and configured so that they can be coupled to both radial vibrational modes. Each Raman beam passes through an acousto-optical modulator (AOM), which allows the phase, frequency and amplitude of the beam to be adjusted by altering the RF signal driving the AOM. One of the RF signals is generated by an arbitrary waveform generator (Keysight M8190A), allowing multiple phase-coherent tones to be imprinted on one of the laser beams. We ensure phase coherence between all pulses in the experimental sequence by tracking the phase (relative to the beginning of the pulse sequence) and applying appropriate corrections (detailed in section S2.2).

By tuning the frequency difference of the Raman beams, one can drive carrier, red- and blue-sideband transitions (see section S2.2). Qubit rotations are obtained by driving carrier transitions, while an SDF $H^{\mathrm{SDF}}_{j,\phi_s}(0, \Omega, \phi_m)$ arises from combining the red- and blue-sideband transitions. Applying this interaction for a duration τ with the qubit in an eigenstate of σ_{ϕ_s} displaces bosonic mode j by $D_j(\alpha) = \exp(\alpha a_j^\dagger - \alpha^* a_j)$, where $\alpha = -i\Omega\tau e^{i\phi_m}/2$. The amplitude and phase-space direction of the displacement are adjusted by varying τ and ϕ_m, respectively.

S1.2 Experimental protocol

Preparation. The bosonic modes are cooled in two stages. First, they are Doppler cooled using a 369.5 nm laser red-detuned from the $^2S_{1/2} \rightarrow {}^2P_{1/2}$ transition. Second, resolved sideband cooling is used to reach their motional ground states, achieving temperatures of $\bar{n} = 0.04$ measured via sideband thermometry [152]. The qubit is prepared in its ground state $|\downarrow\rangle$ via optical pumping, using another 369.5 nm laser resonant with the $^2S_{1/2}\ |F = 1\rangle \rightarrow {}^2P_{1/2}\ |F = 1\rangle$ transition.

Initialisation. To initialise B_1, we apply an SDF interaction $H^{\mathrm{SDF}}_{1,y}(0, \Omega_1, \pi/2)$ for a duration τ, which gives a displacement $D_1(\alpha)$ where $\alpha = \Omega_1\tau/2$. Setting $\tau = \sqrt{2}\,\kappa/\omega\Omega_1$ so that $\alpha = \kappa/\sqrt{2}\,\omega$ displaces the mode from $Q_1 = 0$ to $Q_1 = -\kappa/\omega$ because $D_1(\alpha)Q_1D_1(\alpha)^\dagger = Q_1 - \sqrt{2}\ \mathrm{Re}\,\alpha = Q_1 - \kappa/\omega$. The qubit is first mapped into the SDF interaction basis ($|+\rangle_y$) with an $R_x(\pi/2)$

rotation, and is returned to $|\downarrow\rangle$ after the displacement with an $R_x(-\pi/2)$ rotation. The Rabi frequency of the SDF interaction was frequently recalibrated and on average we measured $\Omega_1 = 2\pi \times 2.23\,\mathrm{kHz}$.

Time evolution. Two SDF interactions on B_1 and B_2 are applied during the time evolution. Their measured Rabi frequencies were, on average, $\sqrt{2}\,\kappa = 2\pi \times 1.42\,\mathrm{kHz}$ and are calibrated within 2% of each other. The duration T of the geometric-phase dynamics is scaled according to the calibrated Rabi frequency.

Reconstruction measurement. After the simulated time evolution, the system is in the entangled state $|\Psi\rangle = a_\downarrow |\downarrow\rangle |\psi_\downarrow\rangle_{B_1} |\xi_\downarrow\rangle_{B_2} + a_\uparrow |\uparrow\rangle |\psi_\uparrow\rangle_{B_1} |\xi_\uparrow\rangle_{B_2}$. In preparation of the reconstruction, a mid-circuit measurement projects the qubit state to either $|\downarrow\rangle$ or $|\uparrow\rangle$ through state-dependent fluorescence induced by a 369.5 nm laser beam resonant with the $^2\mathrm{S}_{1/2}\ |F=1\rangle \rightarrow {}^2\mathrm{P}_{1/2}\ |F=0\rangle$ transition. The qubit states are inferred by thresholding the number of photons collected on an avalanche photodiode (measured state preparation and measurement fidelity of 99.5%), and the outcomes of the measurement determine the probabilities $p_\downarrow = |a_\downarrow|^2$ and $p_\uparrow = |a_\uparrow|^2$. A measurement outcome of $|\uparrow\rangle$ induces significant decoherence of the bosonic modes due to photon recoils. Therefore, the reconstruction only proceeds if the measurement outcome is $|\downarrow\rangle$, for which no photon is emitted. Doing so projects the bosonic modes to $|\psi_\downarrow\rangle_{B_1} |\xi_\downarrow\rangle_{B_2}$. To retrieve $|\psi_\uparrow\rangle_{B_1} |\xi_\uparrow\rangle_{B_2}$ instead, we insert an $R_x(\pi)$ pulse that flips the qubit before the measurement. After the mid-circuit measurement, the characteristic functions $\chi_\downarrow(i\beta_1, i\beta_2)$ and $\chi_\uparrow(i\beta_1, i\beta_2)$ corresponding to each qubit state are measured as described in the main text. The full characteristic function is then the sum of both contributions, $\chi(i\beta_1, i\beta_2) = p_\downarrow \chi_\downarrow(i\beta_1, i\beta_2) + p_\uparrow \chi_\uparrow(i\beta_1, i\beta_2)$. The values $\beta_j = \Omega_2 \tau_j$ are scanned by varying the SDF-pulse duration τ_j. The Rabi frequency was recalibrated between experiments and, on average, $\Omega_2 = 2\pi \times 2.31\,\mathrm{kHz}$, resulting in combined pulse durations of up to 553 µs. We measured $\chi(i\beta_2)$ for $\beta_2 \in [0, 5]$ and $\chi(i\beta_1, i\beta_2)$ for $\beta_1, \beta_2 \in [0, 4]$ by varying the SDF pulse durations. Since the characteristic function is Hermitian, $\chi(i\beta_1, i\beta_2)^* = \chi(-i\beta_1, -i\beta_2)$, we used symmetry to find $\chi(i\beta_2)$ for $\beta_2 < 0$ and $\chi(i\beta_1, \beta_2)$ for $\beta_1 < 0$ or $\beta_2 < 0$. We did not measure the vanishing imaginary part of $\chi(i\beta_2)$ nor $\chi_\downarrow$ at $t = 0$. The measured characteristic functions are shown in section S2.1.

Data acquisition. The characteristic functions were measured in a way to average out the effects of drift. In each run of the experiment, we randomised the order of the displacement-pulse durations in which χ was reconstructed. For each run, the quantum circuit to obtain $\chi_\downarrow$ and $\chi_\uparrow$ was repeated until the mid-circuit measurement succeeded 500 times, resulting in 500 measurement repetitions of the reconstruction routine and 1000 measurements to obtain a value of the full χ. Furthermore, the order of the displacements was randomised. Overall, each of the 1- and 2-dimensional experiments was repeated, respectively, four and two times and the results of the runs averaged for a total of 2000 and 1000 measurements for each duration.

The bosonic mode frequencies were calibrated every 6 min, while the full system parameters were recalibrated after the second experimental run (see section S2.3 for more details). The 1-dimensional and the four 2-dimensional ($t = \{0, 0.9T, T, 2T\}$) experiments were done on five separate days with total durations of 15.6, 2.8, 8.8, 8.7 and 10.6 hours, respectively.

Noise sources Decoherence of the bosonic modes, made up of motional heating and dephasing, was the dominant noise mechanism in our system. Motional heating was caused by electric field noise at the radial mode frequency, while motional dephasing arose from fluctuations in the harmonic trapping potential strength [88]. We measured the heating rate and the motional dephasing time of B_1 (representative for both modes) to be $\dot{\bar{n}} = 0.2\,\text{quanta}\,\text{s}^{-1}$ and $T_2^* = 35\,\text{ms}$ [106]. The motional coherence was limited by noise in the radio frequency (RF) trapping voltage, which was actively stabilised to mitigate fluctuations in the radial mode frequencies. Slow drifts of the trapping voltage were compensated for with frequent motional mode recalibrations (see section S2.3).

S2 Supplemental material

S2.1 Characteristic functions

Figure S1 shows the measured characteristic functions used to reconstruct the wavepacket probability densities. The two-dimensional characteristic functions (fig. S1a–d) require four measurements at each t to obtain the real and imaginary parts of $p_\downarrow\chi_\downarrow(i\beta_1, i\beta_2)$ and $p_\uparrow\chi_\uparrow(i\beta_1, i\beta_2)$. The one-dimensional characteristic functions (fig. S1e) require two measurements to determine $p_\downarrow\chi_\downarrow(i\beta_2)$ and $p_\uparrow\chi_\uparrow(i\beta_2)$, as the vanishing imaginary part is not measured. In both one- and two-dimensional reconstructions, only positive values of β_1 and β_2 are sampled; the characteristic function in other ranges is obtained by symmetry.

We performed post-processing to remove artifacts associated with Fourier transformations between a characteristic function and its probability density. A non-zero DC offset appearing as background noise in the characteristic functions propagates into the probability densities at the origin [147]. Since background noise with a non-zero mean is a technical imperfection and is independent of the geometric-phase evolution, we correct for it in post-processing. We estimate the mean of the background noise by averaging $\chi(i\beta_1, i\beta_2)$ with $\sqrt{\beta_1^2 + \beta_1^2} \geq 3.6$ for the two-dimensional and $\chi(i\beta_2)$ with $\beta_2 \geq 3.6$ for the one-dimensional case, and offset the data by the negative of this average. This baseline correction was on average 0.02, with the largest correction of 0.03.

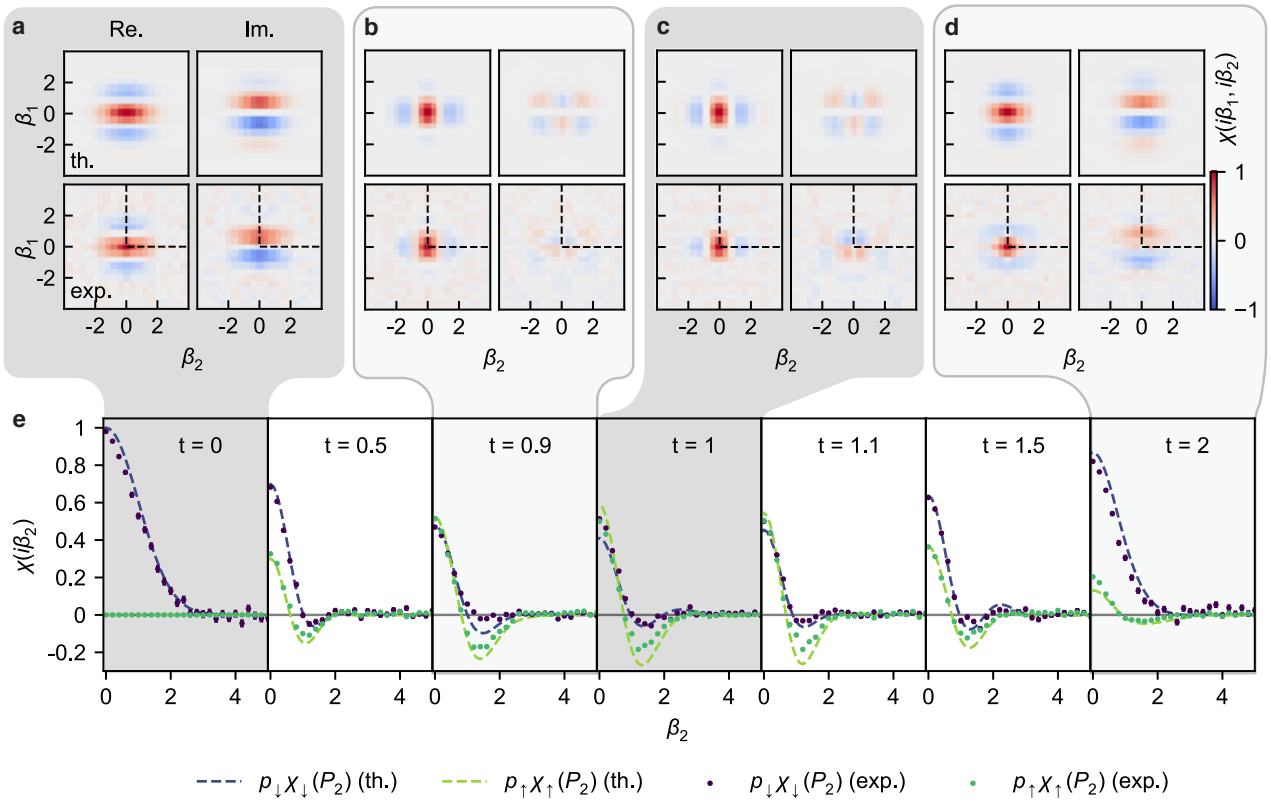

Figure S1: **Characteristic functions of the wavepacket measured for various evolution times. a-d** Joint two-dimensional characteristic function $\chi(i\beta_1, i\beta_2) = p_\downarrow\chi_\downarrow(i\beta_1, i\beta_2) + p_\uparrow\chi_\uparrow(i\beta_1, i\beta_2)$ measured at times $t = \{0, 0.9T, T, 2T\}$ using the full pulse sequence of fig. 2.2. The real (left) and imaginary (right) parts are measured with and without an $R_x(\pi/2)$ pulse in the reconstruction. The top row shows theoretical predictions and the bottom experimental results. $\chi(i\beta_1, i\beta_2)$ were measured in the range $\beta_1, \beta_2 \in [0, 4]$ with 11×11 equidistant samples (dashed quadrant). Values in the remaining three quadrants are obtained from the symmetry of $\chi(i\beta_1, i\beta_2)$. **e** One-dimensional characteristic functions $\chi_\downarrow(i\beta_2)$ and $\chi_\uparrow(i\beta_2)$ obtained by omitting displacements on B_1 in the reconstruction. β_2 was uniformly sampled in the range $[0, 5]$ with 26 points. Each two- and one-dimensional characteristic function was averaged over 1000 and 2000 measurements, respectively. Error bars in **e** represent one standard deviation based on quantum projection noise.

S2.2 Phase coherence in the pulse sequence

This appendix describes the experimental procedure to track the qubit and motional phases, ensuring phase coherence between sequential spin-motional interactions.

The laser-induced excitations interacting with an ion with a qubit frequency ω_0 and a motional mode with frequency ω_m are the carrier (c), red-sideband (rsb), and blue-sideband transitions (bsb). Their interaction Hamiltonians, after dropping high-frequency terms, are

$$H_\mathrm{c} = \frac{\Omega_c}{2}\sigma^+ e^{i\phi_c} e^{i(\omega_c - \omega_0)t} + \mathrm{h.c.}, \tag{S1}$$

$$H_\mathrm{rsb} = \frac{\eta\Omega_r}{2}\sigma^+ a e^{i\phi_r} e^{i(\omega_r - \omega_0 + \omega_m)t)} + \mathrm{h.c.}, \tag{S2}$$

$$H_\mathrm{bsb} = \frac{\eta\Omega_b}{2}\sigma^+ a^\dagger e^{i\phi_b} e^{i(\omega_b - \omega_0 - \omega_m)t)} + \mathrm{h.c.}, \tag{S3}$$

where η is the Lamb-Dicke parameter and $\Omega_{c,b,r}$ are the respective Rabi frequencies. $\omega_{c,b,r}$

and $\phi_{c,b,r}$ correspond, respectively, to the frequency differences and the phase differences of the two orthogonal Raman beams. Simultaneously driving the red- and blue-sidebands with $\Omega = \eta\Omega_r = \eta\Omega_b$ gives

$$\begin{aligned} H_{\mathrm{SDF}} &= H_{\mathrm{rsb}} + H_{\mathrm{bsb}} \\ &= \frac{\Omega}{2}\sigma^{+}[\, a e^{i\phi_r} e^{i(\omega_r - \omega_0 + \omega_m)t} + a^{\dagger} e^{i\phi_b} e^{i(\omega_b - \omega_0 - \omega_m)t} + \mathrm{h.c.}]. \end{aligned} \tag{S4}$$

We consider ω_r and ω_b to be set near-resonant with the red- and blue-sideband transitions,

$$\omega_r = \omega_0 - \omega_m - \delta\omega_m + \delta\omega_0, \tag{S5}$$

$$\omega_b = \omega_0 + \omega_m + \delta\omega_m + \delta\omega_0, \tag{S6}$$

where $\delta\omega_0$ is an asymmetrical (center-line) detuning from the qubit frequency, and $\delta\omega_m$ is a symmetrical detuning from the motional mode frequency. With the spin phase $\phi_s = (\phi_r + \phi_b)/2$ and the motional phase $\phi_m = (\phi_b - \phi_r)/2$, eq. (S4) can be rewritten as

$$H_{\mathrm{SDF}} = \frac{\Omega}{2}\sigma^{+} e^{i(\delta\omega_0 t + \phi_s)} \left[a e^{-i(\delta\omega_m t + \phi_m)} + a^{\dagger} e^{i(\delta\omega_m t + \phi_m)} \right] + \mathrm{h.c.} \tag{S7}$$

This Hamiltonian corresponds to eq. (2.3) in the main text by setting $\delta\omega_0 = 0$ and $\delta\omega_m = \delta$. The motional phase ϕ_m can be adjusted to selectively displace a mode along Q or P. Equation (S7) shows that non-zero or miscalibrated $\delta\omega_0$ and $\delta\omega_m$ introduce a time-dependent phase offset to ϕ_s and ϕ_m which, if uncorrected, will lead to incorrect interactions.

The qubit frequency detuning is, from eq. (S5) and eq. (S6), $\delta\omega_0 = (\omega_b + \omega_r)/2 - \omega_0$. To avoid phase lags associated with ϕ_s, we enforce $(\omega_b + \omega_r)/2 = \omega_c = \bar{\omega}_0$ for all pulses throughout the entire circuit, namely single-qubit rotations and SDF interactions on B_1 and B_2. Here, $\bar{\omega}_0$ indicates the qubit frequency measured via a Ramsey sequence in a separate calibration experiment.

Likewise, eq. (S5) and eq. (S6) give the motional detuning as $\delta\omega_m = (\omega_b - \omega_r)/2 - \omega_m$. To avoid unwanted phase lags associated with ϕ_m, we enforce $(\omega_b - \omega_r)/2 = \bar{\omega}_m$ for all SDF pulses throughout the circuit, where $\bar{\omega}_m$ is the experimentally measured motional frequency, whose calibration procedure is detailed in section S2.3. There is an unavoidable phase lag due to the detuning δ required in the SDF interactions during the time evolution. To correct this, we add a motional phase offset of $\tau_1\delta$ to the SDF interaction during the initial displacement, where τ_1 is the duration of the initialisation. Furthermore, a motional phase offset of $(t + \tau_1)\delta$ is added to the reconstruction SDF pulses, where t is the duration of the time evolution.

S2.3 Calibration of motional frequencies

We used a calibration scheduling routine to recalibrate parameters during each experiment and ensure high-fidelity implementations of the pulse sequence. Moreover, we optimised the scheduler to maximise the experimental duty cycle by analysing the temporal noise behaviours.

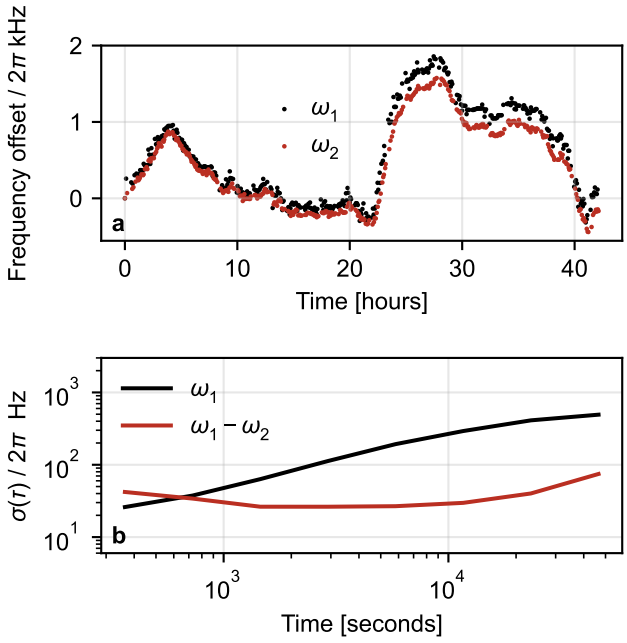

Figure S2: **Frequency drifts of radial motional modes. a** Time series of motional frequencies $\omega_{1,2}$ corresponding to $B_{1,2}$, measured using the calibration routine detailed in the text and plotted as the frequency offset from ω_1 measured at $t = 0$. **b** Allan deviation of ω_1, and of the difference between the two frequencies $(\omega_1 - \omega_2)$.

The data quality of the reconstructed densities depends on correctly setting the laser frequencies for the motional sideband interactions that enact SDF interactions. The motional frequencies ω_1 and ω_2 associated with B_1 and B_2 are calibrated as previously reported [106]. To do so, both SDF interactions are applied, but we set the fields associated with ω_2 to be sufficiently off resonant while calibrating ω_1. We prepare the state $|\downarrow\rangle |0\rangle_{B_1}$ and apply two sequential SDF pulses with a relative phase shift $\phi_m = \pi$. In the absence of frequency errors, the mode returns to its original state and a qubit measurement yields zero population in $|\uparrow\rangle$. However, in the presence of errors, the motion remains entangled with the qubit, giving a non-zero measured probability. The SDF fields' frequencies are then scanned, and a fit to the measurements yields the correct mode frequency. We repeat this procedure to calibrate ω_2 by setting the SDF field associated with ω_1 to be off resonant.

Figure S2 shows the drifts in the radial mode frequencies over time, which varied in a range of $2\pi \times 2.2\,\text{kHz}$ over 2 days. From numerical simulations, we determined that an error tolerance of about 10% is required for the detuning ($\delta \simeq 2\pi \times 667\,\text{Hz}$) in the time evolution to obtain adequate results. Given that typical experiments lasted tens of hours, frequent recalibrations of the motional mode frequencies were necessary. To this end, we implemented a scheduling algorithm to interleave calibrations and experiments [153]. The scheduling rate was determined by choosing a time interval for which the Allan deviation was sufficiently small. From fig. S2b, we chose an interval of 6 minutes, corresponding to an Allan deviation of $2\pi \times 26\,\text{Hz}$ and satisfying the required tolerance. We also found highly correlated noise between the radial

modes (see fig. S2), suggesting a common noise source (e.g., trap RF amplitude fluctuations). Therefore, to increase the experiment duty cycle, frequency offsets measured on B_1 were also used to correct for B_2.

Chapter 3: Simulating open-system molecular dynamics on analog quantum computers

This chapter is a reformatted version of the publication:
Vanessa C. Olaya-Agudelo, Ben Stewart, Christophe H. Valahu, Ryan J. MacDonell, Maverick J. Millican, Vassili G. Matsos, Frank Scuccimarra, Ting Rei Tan and Ivan Kassal, "Simulating open-system molecular dynamics on analog quantum computers", *Phys. Rev. Research* **7**, 023215 (2025).

Abstract

Interactions of molecules with their environment influence the course and outcome of almost all chemical reactions. However, classical computers struggle to accurately simulate complicated molecule-environment interactions because of the steep growth of computational resources with both molecule size and environment complexity. Therefore, many quantum-chemical simulations are restricted to isolated molecules, whose dynamics can dramatically differ from what happens in an environment. Here, we show that analog quantum simulators can simulate open molecular systems by using the native dissipation of the simulator and injecting additional controllable dissipation. By exploiting the native dissipation to simulate the molecular dissipation—rather than seeing it as a limitation—our approach enables longer simulations of open systems than are possible for closed systems. In particular, we show that trapped-ion simulators using a mixed qudit-boson (MQB) encoding could simulate molecules in a wide range of condensed phases by implementing widely used dissipative processes within the Lindblad formalism, including pure dephasing and both electronic and vibrational relaxation. The MQB open-system simulations require significantly fewer additional quantum resources compared to both classical and digital quantum approaches.

3.1 Introduction

Most molecular dynamics is governed by interactions between molecules and their surroundings. With the exception of molecules in vacuum or dilute gas, chemistry occurs in environments—from solvents to crystals to proteins—which decohere the molecule's quantum state and can transfer energy to and from the molecule. Molecular dynamics in condensed phase can differ completely from that in the isolated molecule because molecule-solvent interactions can induce processes such as non-adiabatic transitions, charge transfer, and barrier crossing [17].

Accurate simulations of an isolated molecule's quantum dynamics are challenging on conventional computers due to the exponential growth of the Hilbert space with molecular size. Extending such simulations to an open-system treatment is even more difficult and usually prohibitive, as it often involves representing the molecule's mixed state with a density matrix. These limitations have constrained the most accurate open-system simulation methods to small molecules [46, 154–158].

Quantum computers promise to simulate molecular quantum dynamics efficiently (in polynomial time in system size), but, like classical computers, usually require more resources to simulate open systems. Quantum computers can outperform classical ones by encoding the molecular quantum states on an inherently quantum platform [61, 159–161]. Nevertheless, current quantum algorithms for simulating open-system dynamics require more quantum resources (such as qubits and operations), making them prohibitively expensive for current quantum hardware. Two broad approaches have been pursued for representing system-bath interactions on quantum computers. In the first, additional qubits are added to represent the environment [162–165]. In the other, intrinsic noise of the quantum device is used to mimic the environment [166, 167]. However, when the intrinsic noise does not directly correspond to the desired dissipative process [166]—as is the case when qubit-based computers are used to simulate bosonic modes—using the intrinsic noise may be either impossible or require additional resources (whether qubits or gates) to transform the intrinsic noise into the desired form [167]. Hybrid approaches are also possible, which combine intrinsic noise on ancilla registers representing an environment [168, 169]. Therefore, in both approaches, and especially when simulating systems that cannot be directly mapped to qubits, considerable additional quantum resources are generally required to transform a closed-system quantum simulation into an open one.

Analog quantum simulators using bosonic degrees of freedom promise to simulate molecular quantum dynamics with even fewer resources than digital quantum computers. An analog simulator is a purpose-built device whose Hamiltonian can be engineered to match that of the simulated system, so that the simulator's time evolution reproduces the desired dynamics.

For molecular simulations, analog simulators based on the mixed-qudit-boson (MQB) en-

coding represent molecular electronic and vibrational degrees of freedom using the qudit and bosonic modes of a trapped ion or a circuit quantum electrodynamics (cQED) system [11]. Using bosonic degrees of freedom to simulate nuclear motions—instead of encoding them in many qubits—reduces the quantum resource requirements by about an order of magnitude compared to qubit-based digital quantum simulation [11]. Experimental demonstrations of MQB simulation include simulations of conical intersections [105, 107, 170] and vibronic spectra [106].

However, MQB simulations of molecular dynamics have not been fully generalised to open-system dynamics, with existing proposals limited to vibrational dissipation in trapped-ion devices [11]. Other theoretical [171–173] and experimental [81–83, 174] works on the quantum simulation of energy or charge transfer problems used bosonic degrees of freedom in open-system analog simulations, but were restricted to only some noise mechanisms or were not applicable to molecular quantum dynamics because bosonic modes were used only to represent the environment, not the system of interest.

Here, we present a framework for simulating open-system molecular dynamics with an MQB simulator. Our approach has two significant strengths. First, the dissipation can be engineered using both native dissipation and injected controllable dissipation, on both the qudit and the bosonic modes, so that chemical dissipative processes can be easily mapped onto the MQB simulator. Doing so turns decoherence mechanisms that usually limit analog simulations into a resource that makes the simulations more powerful. Second, engineering the dissipative processes requires few additional resources, whose number is often independent of the molecular size. In particular, we show how chemically relevant dissipative processes—including both electronic and vibrational relaxation and dephasing—can be implemented with existing trapped-ion technology. Overall, MQB simulators can solve the harder problem of open-system simulation with minimal overhead and with greater resistance to errors.

3.2 Molecular open-system dynamics

There are many approaches to modelling open molecular systems, depending on where the molecule-environment boundary is drawn and what techniques are used to simulate either the molecule, the environment, or their interaction [17, 175]. In all cases, open-system simulations aim to simulate the environment using a simpler method than that used for the molecule itself. The approaches to simulating the environment range from ones that explicitly describe the components of the environment, often at considerable computational cost, to those that treat either the environment or its influence on the molecule in an effective way.

A logical starting point for developing analog open-system approaches is the Lindblad master equation [16, 176], the most general completely positive and trace-preserving Markovian master

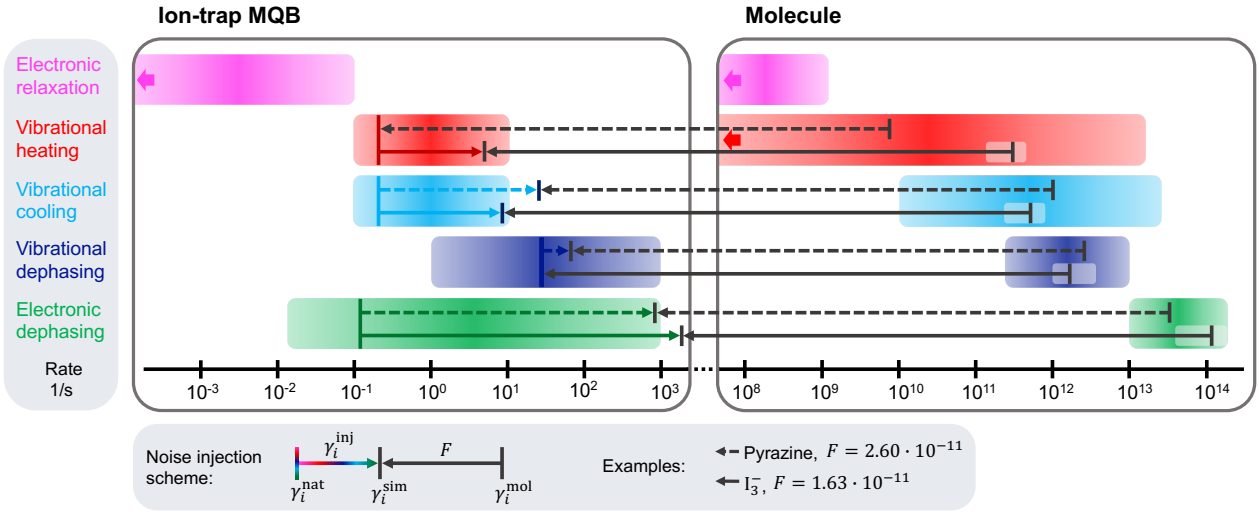

Figure 3.1: Typical rates for the most-relevant dissipative processes, **(left)** in a trapped-ion MQB simulator [93–95, 106, 177, 178] and **(right)** in molecules in condensed phase (modified from [17]). For both pyrazine [179–181] and triiodide [21] examples, each dissipative rate γ_i^{mol} (and range: grey highlights) is mapped onto the corresponding trapped-ion rate $\gamma_i^{\text{sim}} = F\gamma_i^{\text{mol}}$ using the scaling factor $F = \max_i \gamma_i^{\text{nat}}/\gamma_i^{\text{mol}}$ (black arrows). The maximum ratio is obtained for vibrational pure dephasing for triiodide and vibrational heating for pyrazine; therefore, no injection is required for these types of dissipation. Other dissipative processes require injected rates γ_i^{inj} (coloured arrows), to ensure that $\gamma_i^{\text{sim}} = \gamma_i^{\text{nat}} + \gamma_i^{\text{inj}}$.

equation. It describes the dynamics of the molecule's reduced density matrix ρ (we set $\hbar = 1$ throughout) by

$$\frac{d\rho}{dt} = -i[H^{\text{mol}}, \rho] + \sum_i \gamma_i^{\text{mol}} \mathcal{D}\left[L_i\right]\rho, \tag{3.1}$$

where H^{mol} is the Hamiltonian of the isolated molecule, which can be specified in any form, including as a vibronic coupling (VC) model [2, 11] (for example, see the VC Hamiltonian in eq. (3.4)). Each dissipative superoperator $\mathcal{D}\left[L_i\right]$ with rate γ_i^{mol} acts on ρ as

$$\mathcal{D}\left[L_i\right]\rho = L_i \rho L_i^\dagger - \tfrac{1}{2}\{L_i^\dagger L_i, \rho\}, \tag{3.2}$$

describing a dissipative process by a Lindblad operator L_i.

In chemical contexts, there are usually four dominant dissipation mechanisms, which can be derived from microscopic principles. Equation (3.1) is usually derived from the related Redfield master equation, which is obtained from a perturbative treatment of the system-environment coupling in the Markovian limit [17, 175]. A Redfield equation is usually converted to a Lindblad equation by making the secular approximation [16, 17, 175], which is valid when the timescales of interest are slower than any rapidly oscillating terms in the master equation, allowing them to average out. In the secular limit, population relaxation and pure dephasing become decoupled [17, 175], making it possible to classify the most important dissipative processes in open chemical systems. With typical timescales given in fig. 3.1, they are:

1. *Radiative electronic relaxation* is the decay of excited electronic populations by spontaneous emission, including both fluorescence and phosphorescence. It is described by the dissipator

$\mathcal{D}[|n\rangle\langle m|]$ and rate $\gamma^{\mathrm{mol}}_{nm}$ for electronic states with energies $\varepsilon_m > \varepsilon_n$. Non-radiative electronic relaxation, such as intersystem crossing and internal conversion, are indirect consequences of vibrational relaxation and vibronic coupling, meaning that they are accounted for by the processes below.

2. *Vibrational heating and cooling* are the gain and loss of energy in molecular vibrational modes, and are the most important way for a molecule to reach equilibrium with a thermal environment. For mode j, heating and cooling have dissipators $\mathcal{D}[a_j^\dagger]$ and $\mathcal{D}[a_j]$, with rates $\gamma^{\mathrm{mol}}_{+,j}$ and $\gamma^{\mathrm{mol}}_{-,j}$, respectively. Detailed balance at temperature T^{mol} requires $\gamma^{\mathrm{mol}}_{+,j} = \gamma^{\mathrm{mol}}_{-,j} \exp(-\nu_j^{\mathrm{mol}}/k_{\mathrm{B}}T^{\mathrm{mol}})$ for mode frequency ν_j^{mol}.
3. *Electronic pure dephasing* is the reduction in phase coherence between electronic eigenstates, described by the dissipator $\mathcal{D}[|n\rangle\langle n|]$ and rate $\gamma^{\mathrm{mol}}_{\mathrm{e},n}$ for electronic state n.
4. *Vibrational pure dephasing* is the decay of phase coherence between vibrational states, described by the dissipator $\mathcal{D}[a_j^\dagger a_j]$ and rate $\gamma^{\mathrm{mol}}_{\mathrm{v},j}$ for vibrational mode j.

3.3 Analog open-system simulation

An analog simulator evolves in time in the same way as the molecule being simulated, so that the molecule's dynamics can be retrieved by measuring the simulator evolution. To achieve this, the molecular Hamiltonian H^{mol} must be mapped onto the controllable simulator Hamiltonian H^{sim}. To allow for a change of time scales, the mapping may include a scaling factor F such that $H^{\mathrm{sim}} = FH^{\mathrm{mol}}$, where F represents the ratio of the typical energy scale of the simulator to that of the molecule. Here, we extend the existing closed-system simulation approach to open-system ones and, by considering how this change affects the possible values of F, show that there is always a performance advantage in open-system simulations compared to closed ones.

For open-system simulations, two sources of dissipation can be used by the simulator: *native* uncontrollable dissipation and *injected* controllable dissipation. Native dissipation is intrinsic, always present in the simulator, and cannot be tuned. Conversely, injected dissipation consists of processes that can be engineered. Native dissipation is often considered to be a hindrance in quantum systems, but, in analog simulations, it can be a valuable tool for open-system simulations that extends the possible duration of simulations.

Native dissipation can be useful in an analog simulation if it contains a significant component that is Markovian and stable. Fortunately, as in molecules, dominant dissipative processes in analog hardware are usually well described using Lindblad dissipators, $\mathcal{D}[L_i^{\mathrm{nat}}]$, with corresponding rates, γ_i^{nat} [88]. Indeed, if the coupling to the environment is weak and the secular approximation holds, the same four dissipative processes that are dominant in molecules will be

dominant in the simulator. We assume that the simulator's dissipation rates are stable, i.e., that they can be measured in a preliminary experiment and remain constant throughout subsequent simulations. Stability is manageable because it only requires the dissipation to be stable over several runs of an experiment before it can be calibrated again.

We then refer to native dissipators $\mathcal{D}\left[L_i^{\text{nat}}\right]$ as *usable* if they implement a desired molecular dissipator $\mathcal{D}[L_i]$. In contrast, *unusable* dissipation includes all native dissipators that have no analog in the molecule, as well as processes that cannot be described by the Lindblad formalism (e.g., non-Markovian ones).

A molecular dissipator, $\mathcal{D}[L_i]$, can be simulated on the analog simulator by ensuring that its dissipation rate is related to the corresponding molecular rate by the same scaling factor F as above, $\gamma_i^{\text{sim}} = F\gamma_i^{\text{mol}}$. This condition can be met by using native dissipation with rate γ_i^{nat} and injecting additional dissipation of the same type at rate γ_i^{inj} that satisfies

$$\gamma_i^{\text{sim}} = \gamma_i^{\text{nat}} + \gamma_i^{\text{inj}} = F\gamma_i^{\text{mol}}. \tag{3.3}$$

For a closed-system simulation, F can be chosen within hardware constraints, $F \in [F_{\text{min}}^{\text{cs}}, F_{\text{max}}^{\text{cs}}]$ ("cs" for closed system). The lower bound, $F_{\text{min}}^{\text{cs}} = t_{\text{mol}}/\tau_d^{\text{cs}}$, is set by the ratio of the desired total simulation time in the molecule, t_{mol}, to the coherence time of the simulator, τ_d^{cs}, after which the simulator is deemed insufficiently reliable. The upper bound, $F_{\text{max}}^{\text{cs}}$, is the ratio of the maximum simulator interaction that can be engineered in H^{sim} and the largest interaction of that type in H^{mol}. Consequently, the longest molecular time that can be simulated on the specific hardware is $t_{\text{max}}^{\text{cs}} = \tau_d^{\text{cs}} F_{\text{max}}^{\text{cs}}$.

Including dissipation gives a new range of F for open-system simulation, $F \in [F_{\text{min}}^{\text{os}}, F_{\text{max}}^{\text{os}}]$ ("os" for open system). $F_{\text{max}}^{\text{os}}$ remains set by the hardware capabilities and is therefore unchanged, $F_{\text{max}}^{\text{os}} = F_{\text{max}}^{\text{cs}}$. By contrast, $F_{\text{min}}^{\text{os}}$ must now meet two conditions. First, as in the closed simulation, F is constrained by the open-system coherence time τ_d^{os} of the simulator, $F \geq t_{\text{mol}}/\tau_d^{\text{os}}$. Because some dissipation is used in the simulation and τ_d^{os} is determined only by the unused dissipation, $\tau_d^{\text{os}} > \tau_d^{\text{cs}}$, giving an improvement over the closed-system case. Second, because all γ_i^{inj} must be positive, eq. (3.3) requires that $F\gamma_i^{\text{mol}} \geq \gamma_i^{\text{nat}}$ for all i, that is, $F \geq R = \max_i \gamma_i^{\text{nat}}/\gamma_i^{\text{mol}}$. Overall, the lower bound for the open-system simulation is $F_{\text{min}}^{\text{os}} = \max(t_{\text{mol}}/\tau_d^{\text{os}}, R)$.

Importantly, using some of the native noise in the simulation always extends the maximum simulation duration. The longest possible open-system simulated time is $t_{\text{max}}^{\text{os}} = \tau_d^{\text{os}} F_{\text{max}}^{\text{os}} = \tau_d^{\text{os}} F_{\text{max}}^{\text{cs}}$; because $\tau_d^{\text{os}} > \tau_d^{\text{cs}}$, we find that $t_{\text{max}}^{\text{os}} > t_{\text{max}}^{\text{cs}}$. Therefore, any hardware that can be used for closed-system simulation can achieve longer simulated time when used for open-system simulation.

If $F_{\text{min}}^{\text{os}} = R$, then the F that maximises the use of native dissipation and minimises injected dissipation is $F = F_{\text{min}}^{\text{os}}$; doing so means that no injected dissipation is required for the process with the maximum ratio $\gamma_i^{\text{nat}}/\gamma_i^{\text{mol}}$ (see section 3.6 for two examples).

3.4 Closed-system MQB simulation

MQB simulators [11] are examples of analog quantum simulators, in which the molecular electronic and vibrational degrees of freedom are encoded in a qudit and multiple bosonic modes of the simulator. In a trapped-ion MQB implementation, the qudit is encoded in the electronic states of one of the ions, while the bosonic modes correspond to the collective normal modes of motion (vibrational modes) of the ion chain. MQB simulators are programmable because all parameters—including the energies of all states and the couplings between degrees of freedom—can be controllably adjusted using light-matter interactions [11].

The quantum resources required for an MQB simulation scale linearly with molecule size [11]. A chain of N trapped ions contains $3N$ vibrational modes, meaning that a molecule with d electronic states and N vibrational modes can be mapped onto a single qudit in a chain of $\lceil N/3 \rceil$ ions.

The MQB approach implements vibronic-coupling Hamiltonians that are expressed as power series in the vibronic couplings [11]. The linear vibronic coupling (LVC) Hamiltonian, where the electronic and vibrational degrees of freedom are linearly coupled [11], is

$$H^{\mathrm{mol}} = \sum_j \nu_j^{\mathrm{mol}} a_j^\dagger a_j + \sum_{n,m} c_0^{(n,m)} |n\rangle \langle m| + \sum_n \sum_{j \in \mathbf{t}} \frac{c_j^{(n)}}{\sqrt{2}} (a_j^\dagger + a_j) |n\rangle \langle n| + \sum_{n \neq m} \sum_{j \in \mathbf{c}} \frac{c_j^{(n,m)}}{\sqrt{2}} (a_j^\dagger + a_j) |n\rangle \langle m| , \quad (3.4)$$

where $|n\rangle$ are the electronic states, a_j are the annihilation operators of the molecular vibrations, such that $Q_j = (a_j^\dagger + a_j)/\sqrt{2}$ is the dimensionless position of the jth mode. The constants $c_0^{(n,n)}$ are the electronic energies, $c_0^{(n,m)}$ $(n \neq m)$ are the inter-state couplings, $c_j^{(n)}$ and $c_j^{(n,m)}$ are the vibronic (vibrational-electronic) couplings for, respectively, the *tuning* $(j \in \mathbf{t})$ and the *coupling* $(j \in \mathbf{c})$ modes. Parametrising eq. (3.4) requires carrying out an electronic-structure calculation in advance [11]. Higher-order vibronic-coupling terms could be readily included in H^{mol}.

The molecular Hamiltonian, H^{mol}, can be directly encoded on a trapped-ion simulator. The mapping begins with the Hamiltonian of a chain of N ions [88],

$$H^{\mathrm{ion}} = \sum_{j=1}^{3N} \nu_j a_j^\dagger a_j + \frac{1}{2} \sum_{n=0}^{d-1} \omega_n |n\rangle \langle n| , \quad (3.5)$$

where the vibrational mode j has frequency ν_j and ω_n is the frequency of the nth electronic state relative to $|0\rangle$, the lowest state used in the simulation.

The remaining terms in H^{mol} are simulated by adding light-matter interactions that induce couplings in the simulator [11]. These interactions can be implemented through stimulated Raman transitions using pairs of non-copropagating laser beams that are both approximately

detuned by Δ from an electronic excited state $|e\rangle$ outside of the qudit [88, 90, 91]. The frequency difference between the two Raman beams, $\Delta\omega_{\mathrm{L}}$, can be tuned to implement all the necessary interactions: electronic coupling, vibronic tuning, and vibronic coupling.

Electronic coupling between states $|n\rangle$ and $|m\rangle$ is implemented by setting $\Delta\omega_{\mathrm{L}} = (\omega_m - \omega_n) + (\chi_m - \chi_n)$, where $\chi_m - \chi_n$ is a frequency shift relative to the electronic transition. In the interaction picture with respect to eq. (3.5) and after a rotating wave approximation, the electronic coupling Hamiltonian between states $|n\rangle$ and $|m\rangle$ is [88, 91]

$$H^{\mathrm{ion}}_{\mathrm{e},n,m} = \Omega_{n,m} \left|n\right\rangle \left\langle m\right| e^{-i(\chi_m - \chi_n)t} + \mathrm{h.c.}, \tag{3.6}$$

with interaction strength $\Omega_{n,m} = g^*_{n,e,A} g_{m,e,B}/2\Delta$, which can be adjusted by varying either the detuning Δ or the intensity-dependent light-matter couplings $g^*_{n,e,A}$ and $g_{m,e,B}$ of the beams coupling $|n\rangle$ to $|e\rangle$ and $|m\rangle$ to $|e\rangle$, respectively.

Vibronic tuning for state $|n\rangle$ is implemented by setting $\Delta\omega_{\mathrm{L}}$ close to the frequency of a vibrational mode j ($\Delta\omega_{\mathrm{L}} = \nu_j - \delta_j$), which, in the interaction picture with respect to eq. (3.5) and after a rotating wave approximation, gives [90, 91]

$$H^{\mathrm{ion}}_{\mathrm{t},n} = \Theta'_{n,j}(a_j^\dagger e^{-i\delta_j t} + a_j e^{i\delta_j t}) \left|n\right\rangle \left\langle n\right|, \tag{3.7}$$

where $\Theta'_{n,j} = \eta g^*_{n,A,j} g_{n,B,j}/\Delta$ is an AC Stark shift with η the Lamb-Dicke parameter. $\Theta'_{n,j}$ can be adjusted by varying either the detuning Δ or the intensity-dependent couplings $g_{n,A,j}$ and $g_{n,B,j}$. We have omitted a Stark shift term from eq. (3.7), which can be made vanishingly small by choosing appropriate laser parameters [182, 183].

Finally, vibronic coupling between states $|n\rangle$ and $|m\rangle$ requires that one of the Raman beams be bichromatic and contain two frequency tones of equal amplitude. The frequency differences between each bichromatic tone and the other Raman beam are $\Delta\omega^{\pm}_{\mathrm{L}} = (\omega_m - \omega_n) \pm (\nu_j + \delta_j) + (\chi_m - \chi_n)$. This interaction (akin to a Mølmer-Sørensen interaction [89]), in the interaction picture with respect to eq. (3.5) and after a rotating wave approximation, gives the coupling Hamiltonian [89, 91]

$$H^{\mathrm{ion}}_{\mathrm{c},n,m} = \Omega'_{n,m,j} \left(a_j^\dagger e^{-i\delta_j t} + a_j e^{i\delta_j t}\right) \left(\left|n\right\rangle \left\langle m\right| e^{-i(\chi_m - \chi_n)t} + \mathrm{h.c.}\right), \tag{3.8}$$

with $\Omega'_{n,m,j} = \eta g^*_{n,m,A,j} g_{n,m,B,j}/2\Delta$, where $g_{n,m,A,j}$ is the light-matter coupling of the monochromatic Raman beam and $g_{n,m,B,j}$ is the light-matter coupling of both tones in the bichromatic Raman beam. $\Omega'_{n,m,j}$ can then be adjusted by varying either Δ, $g_{n,m,A,j}$, or $g_{n,m,B,j}$.

The electronic-coupling, vibronic-tuning, and vibronic-coupling Hamiltonians can be added for any modes and any electronic states by introducing interactions as described above. For N ions and d electronic states, and after moving to a further interaction picture with respect to

$H = \sum_{j=1}^{3N} \delta_j a_j^\dagger a_j + \sum_{n=0}^{d-1} \chi_n |n\rangle\langle n|$, the overall simulator Hamiltonian becomes

$$H^{\text{sim}} = \sum_{j=1}^{3N} \delta_j a_j^\dagger a_j + \sum_{n=0}^{d-1} \chi_n |n\rangle\langle n| + \sum_{n\neq m} \Omega_{n,m} |n\rangle\langle m| + \sum_{n} \sum_{j\in\mathbf{t}} \Theta'_{n,j}(a_j^\dagger + a_j) |n\rangle\langle n| + \sum_{n\neq m} \sum_{j\in\mathbf{c}} \Omega'_{n,m,j}(a_j^\dagger + a_j) |n\rangle\langle m| . \quad (3.9)$$

H^{sim} is a direct mapping of the molecular Hamiltonian of eq. (3.4). The simulator is fully programmable: the parameters of eq. (3.9)—δ_j, χ_n, $\Omega_{n,m}$, $\Theta'_{n,j}$, and $\Omega'_{n,m,j}$—can be tuned independently by adjusting suitable laser parameters, such as the intensity or frequency [11].

The scaling factor F for molecular simulations on ion traps is typically between $F_{\text{min}}^{\text{cs}} \sim 10^{-12}$ and $F_{\text{max}}^{\text{cs}} \sim 10^{-10}$ (fixed by the maximum achievable laser power for Raman interactions), the ratio between molecular femtosecond timescales and trapped-ion millisecond timescales. The slower ion-trap dynamics, combined with the sub-microsecond timing resolution of trapped-ion simulators, means that greater time resolution is available on an MQB simulator than in direct spectroscopic experiments on a molecule [105]. The long coherence times in trapped-ion systems allow the simulation of chemical dynamics for hundreds of picoseconds [106], which is sufficient to observe ultrafast photochemical dynamics.

3.5 Open-system MQB simulation on ion traps

Each chemical dissipator listed in section 3.2 can be engineered on a trapped-ion MQB simulator, using a combination of light-matter interactions and various types of noise injection (summarised in fig. 3.1). For each case, we derive a rate for the injected dissipation, which we show to be fully controllable, allowing one to tune the simulator dissipator rates of eq. (3.3).

3.5.1 Radiative electronic relaxation

In an MQB architecture, radiative electronic relaxation corresponds to the native spontaneous decay of an excited state $|m\rangle$ to a lower state $|n\rangle$ at a rate Γ_{nm}. This is a native dissipative process with Lindblad operator $L_i = |n\rangle\langle m|$ and rate $\gamma_{nm}^{\text{nat}} = \Gamma_{nm}$.

When the native Γ_{nm} is insufficient to map the radiative electronic relaxation rate of the molecule, optical pumping [184]—a common technique used in operations such as laser cooling [102], dissipative quantum state preparation [185], and measurement [186]—can artificially decrease the lifetime of a given excited state. The procedure is depicted in fig. 3.2a and involves driving a transition from $|m\rangle$ to an auxiliary high-lying electronic state $|l\rangle$ that can decay to $|n\rangle$ with $\Gamma_{nl} > \Gamma_{nm}$. The driving is achieved using a laser with interaction strength Ω_{ml} and frequency ω_{ext}, which is detuned from the electronic transition by $\Delta_{ml} = \omega_{\text{ext}} - (\omega_l - \omega_m)$. The

population in $|l\rangle$ decays to $|n\rangle$ and $|m\rangle$ with rates Γ_{nl} and Γ_{ml}, respectively. Population that returns to $|m\rangle$ repeats the optical-pumping cycle until it is completely transferred to $|n\rangle$. The state $|l\rangle$ can be adiabatically eliminated from the dynamics when $\Gamma_{nl} \gg \Omega_{ml}$, resulting in an effective decay rate [187]

$$\gamma_{nm}^{\text{inj}} = \frac{\Omega_{ml}^2}{(\Gamma_{nl} + \Gamma_{ml})^2 + 4\Delta_{ml}^2}\Gamma_{nl}. \tag{3.10}$$

γ_{nm}^{inj} can be tuned over a wide range by varying the laser properties Ω_{ml} and Δ_{ml}.

Photon scattering during optical pumping imparts momentum kicks to the ions that can heat the vibrational modes. However, this heating rate is negligible in practice, being quadratic in the Lamb-Dicke parameter η, $\gamma_+ = \Gamma'_{nm}\eta^2$ [188]. Typical values $\Gamma'_{nm} \approx 0.02\,\text{s}^{-1}$ and $\eta = 0.1$ give $\gamma_+ = 2 \times 10^{-4}\,\text{s}^{-1}$, which is negligible compared to typical heating rates in ion-traps, which are in the range 0.1 to $10\,\text{s}^{-1}$ (see fig. 3.1). In any event, what little heating is induced could always be considered as additional useful heating.

The derivation of eq. (3.10) assumes that population can only decay from $|l\rangle$ to $|n\rangle$ or $|m\rangle$. If there are dipole-allowed transitions to other electronic states $|m'\rangle$, additional driving beams can repump the population from $|m'\rangle$ back into the optical pumping cycle [189].

3.5.2 Vibrational heating and cooling

Vibrational heating and cooling in a trapped-ion simulator commonly occur due to electric-field noise. This dissipation is routinely characterised experimentally [150, 190] and is described by Lindblad dissipators $\mathcal{D}[a]$ and $\mathcal{D}[a^\dagger]$. The corresponding rates are approximately, $\gamma_{+,j}^{\text{nat}} = \gamma_{-,j}^{\text{nat}} \exp\left(-\nu_j/k_B T^{\text{nat}}\right) \approx \gamma_{-,j}^{\text{nat}}$, because typical trap frequencies ($\nu_j/2\pi \sim 1\,\text{MHz}$) are much smaller than $k_B T^{\text{nat}}$ for T^{nat} between 4 and 300 K. These native rates vary from 0.1 to 1000 quanta/s [177, 190, 191]. If the native dissipative rates are insufficient, additional dissipation can be injected.

Single-mode heating and cooling

The injection of vibrational heating and cooling was proposed for ion-trap simulators in the original MQB paper [11]. The proposed injection was via resolved-sideband laser interactions, where the desired molecule-environment coupling and temperature could be controlled by tuning the laser parameters [11]. However, these laser interactions could change the ion's electronic state, disturbing the ongoing coherent simulation.

To overcome this limitation, a similar dissipation scheme can be implemented using an ancillary ion that shares the motion with the MQB qudit ion (i.e., sympathetic cooling [82, 90, 192]), without affecting the electronic states of the qudit. Dissipators $\mathcal{D}[a_j]$ and $\mathcal{D}[a_j^\dagger]$ can then be engineered using a bichromatic laser (one with two frequency tones), interacting with the

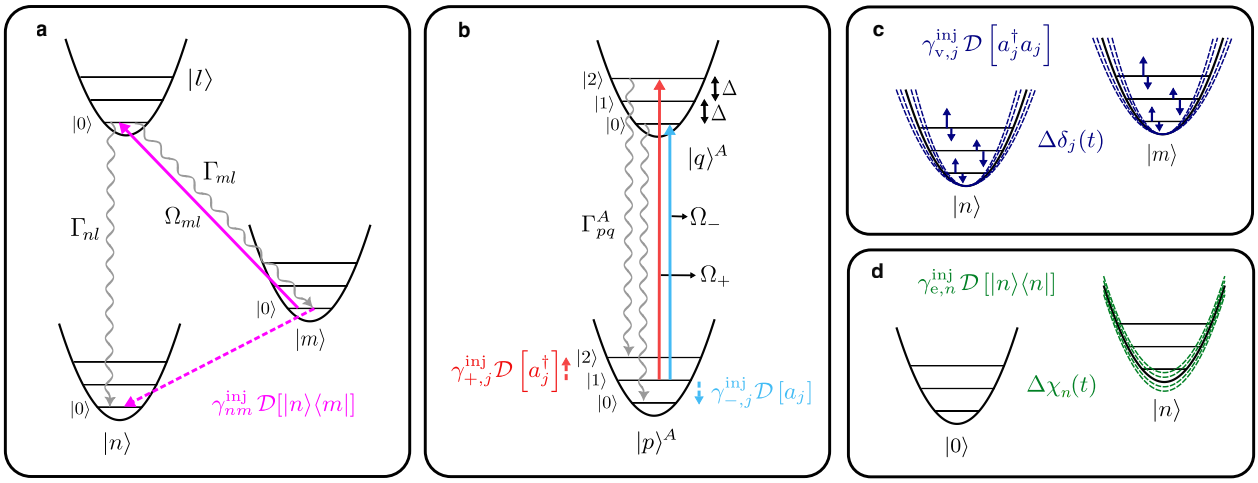

Figure 3.2: Injecting the four molecular Lindblad dissipators into a trapped-ion MQB simulator. **a)** Optical pumping to control the radiative electronic relaxation from $|m\rangle$ to $|n\rangle$. The $|m\rangle$ population is pumped (pink solid arrow) to an auxiliary state $|l\rangle$, chosen for its rapid spontaneous decay (wavy arrows) back to $|n\rangle$ and $|m\rangle$. The population at $|m\rangle$ effectively decays to $|n\rangle$ (pink dashed arrow) with rate γ^{inj}_{nm}. **b)** Resolved sideband interactions applied to an ancilla ion (A) injecting vibrational heating and cooling. A bichromatic laser with coupling strengths $\Omega_\pm$ (red and blue arrows) and detunings $\Delta = \pm\nu_j$ changes the vibrational state from $|i\rangle$ to $|i \pm 1\rangle$. This is followed by an electronic decay from $|q\rangle^A$ to $|p\rangle^A$ at a rate Γ^A_{pq} (wavy arrows), without affecting the vibrational state. **c)** Injection of vibrational pure dephasing. A noisy trap electrode or targeted laser field induces fluctuations in the jth vibrational mode potential strength (blue dotted potentials), which in turn induce fluctuations $\Delta\delta_j(t)$ in the mode's energy levels (small blue arrows). **d)** Injection of electronic pure dephasing. A noisy magnetic field or targeted laser field induces fluctuations $\Delta\chi_n(t)$ in the electronic energy level $|n\rangle$ (green dotted potentials).

ancilla ion. The frequency of each tone is set so that it sympathetically cools or heats a shared vibrational mode. The ratio of the two tones' strengths can be adjusted to simulate a desired environment's temperature.

Figure 3.2b depicts the electronic transition $|p\rangle^A \to |q\rangle^A$ in the ancillary ion A driven by a bichromatic laser. The interaction strengths are Ω_- and Ω_+, with detunings $\Delta = -\nu_j$ for the red sideband and $\Delta = +\nu_j$ for the blue sideband, respectively. The electronic population decays from $|q\rangle^A$ to $|p\rangle^A$ at rate Γ^A_{pq} (this can be due to spontaneous emission or engineered as in eq. (3.10)). The dynamics of the vibrational mode is then described by the Lindblad master equation [101, 103]

$$\frac{d\rho_j}{dt} = -i[\nu_j a_j^\dagger a_j, \rho_j] + \left(\gamma^{\text{inj}}_{+,j}\mathcal{D}[a_j^\dagger] + \gamma^{\text{inj}}_{-,j}\mathcal{D}[a_j]\right)\rho_j, \tag{3.11}$$

where ρ_j is the reduced density matrix of mode j. In the limit $\Omega_\pm \ll \Gamma^A_{pq}$ (which usually holds in trapped-ion simulators), the injected dissipation rates depend only on the laser parameters [101, 103, 187]:

$$\gamma^{\text{inj}}_{\pm,j} = \eta_j^2 \Gamma^A_{pq}\left[B(\Delta \mp \nu_j) + \alpha B(\Delta)\right], \tag{3.12}$$

$$B(\Delta) = \frac{\Omega_\pm^2}{\left(\Gamma^A_{pq}\right)^2 + 4\Delta^2}, \tag{3.13}$$

where η_j is the Lamb-Dicke parameter and α is an angular factor ($\alpha = 2/5$ for dipole transitions [187]).

In molecules, heating and cooling most commonly arise when the molecule is coupled to a thermal environment. Simulating a thermal environment requires that the heating and cooling rates satisfy detailed balance, $\gamma^{\text{sim}}_{+,j} = \gamma^{\text{sim}}_{-,j} \exp(-\nu_j / k_{\text{B}} T^{\text{sim}})$, where $T^{\text{sim}} = (\nu_j / \nu_j^{\text{mol}}) T^{\text{mol}}$. In terms of the injected rates,

$$\gamma^{\text{inj}}_{+,j} = \gamma^{\text{inj}}_{-,j} \zeta^2 - \gamma^{\text{nat}}_{-,j} (1 - \zeta^2), \tag{3.14}$$

where $\zeta^2 = \exp(-\nu_j^{\text{mol}} / k_{\text{B}} T^{\text{mol}})$. If, as is the case in good ion traps, $\gamma^{\text{nat}}_{-,j} \ll \gamma^{\text{inj}}_{-,j}$, the Boltzmann factor can be incorporated into the simulation through the interaction strength of eq. (3.12) by setting $\Omega_+ = \zeta \Omega_-$. In other words, the environment temperature T^{mol} can be set by tuning the ratio between the blue- and red-sideband interaction strengths, while their absolute value determines the strength of the system-environment coupling.

Global vibrational heating and cooling

Using mode-resolved laser interactions as described above means that the number of required laser interactions scales linearly with the number of modes, a cost that can be significantly reduced if all the heating and cooling rates are similar. In many cases, the precise spectral density of the environment is either unknown or unimportant; in those cases, it is common to assume that the heating rates for all vibrational modes are equal (and likewise for the cooling rates). In those cases, where a precise spectral density is not required, similar heating and cooling rates can be injected for all modes using a single broadband laser that can heat and cool all modes simultaneously. According to eq. (3.12), this can be achieved if the laser parameters (Γ^A_{pq}, $\Omega_\pm$, Δ) and the vibrational frequencies (ν_j) are similar for all vibrational modes. A global laser interaction with a sufficiently broadband spectrum can target all modes, setting the same values for Γ^A_{pq} and $\Omega_\pm$, as well as small Δ for all modes.

3.5.3 Electronic and vibrational pure dephasing

Electronic and vibrational dephasing can be injected by inducing classical stochastic fluctuations in the energy levels of the electronic and vibrational states. The resulting dephasing rates can be tuned by controlling the variances and correlation times of the fluctuations.

We consider a fluctuating Hamiltonian proportional to an arbitrary operator O,

$$H(t) = \Delta\Phi(t)\, O, \tag{3.15}$$

where the fluctuations, $\Delta\Phi(t)$, are a zero-mean stochastic process. To simulate pure dephasing, we consider the ensemble average of the density matrix $\langle \rho \rangle$ over many realisations of $\Delta\Phi(t)$ [193,

194]. This approach reflects experimental quantum simulations, where expectation values are measured by averaging over many outcomes. The resulting dissipator is [195, 196]

$$\mathcal{D}[O]\langle\rho\rangle = \gamma\left(O\langle\rho\rangle O^\dagger - \tfrac{1}{2}\{O^\dagger O, \langle\rho\rangle\}\right), \tag{3.16}$$

with rate $\gamma = \frac{1}{2}\int_0^t \langle\Delta\Phi(t)\Delta\Phi(s)\rangle\, ds$, where $\langle\Delta\Phi(t)\Delta\Phi(s)\rangle$ is the auto-correlation function of the fluctuations. For Gaussian, Markovian, and wide-sense stationary noise, the rate simplifies to [197]

$$\gamma = \tfrac{1}{2}\langle\Delta\Phi(t)^2\rangle\tau_c, \tag{3.17}$$

where $\langle\Delta\Phi(t)^2\rangle$ is the variance of the noise and $\tau_c \ll 1/\gamma$ is its correlation time. Either of these quantities can be used to adjust the dephasing rate.

In the following, we present several ways to inject stochastic fluctuations into the terms of the simulator Hamiltonian of eq. (3.9), in a way that results in controllable electronic and vibrational dephasing.

Dephasing single modes or electronic levels by noise

Vibrational and electronic pure dephasing can be independently engineered by adding frequency fluctuations to the laser beams that drive the closed-system dynamics. Such frequency fluctuations can be imprinted on the beams by frequency modulating the acousto-optical modulator (AOM) already used for the closed-sysem simulation. (fig. 3.3). Thus, no additional experimental hardware is necessary to inject pure dephasing.

Vibrational pure dephasing of mode j is implemented by injecting frequency fluctuations into both vibronic Hamiltonians of eqs. (3.7) and (3.8), with the replacement $\delta_j \to \delta_j + \Delta\delta_j(t)$. Electronic pure dephasing of qudit levels n and m requires adding frequency fluctuations to the coupling Hamiltonians of eqs. (3.6) and (3.8), with the replacements $\chi_n \to \chi_n + \Delta\chi_n(t)$ and $\chi_m \to \chi_m + \Delta\chi_m(t)$. To this end, we modify the frequency differences of the Raman beams as follows. For the vibronic tuning interaction, we set $\Delta\omega_{\mathrm{L}} = \nu_j - (\delta_j + \Delta\delta_j(t))$. For the vibronic coupling interaction, we set $\Delta\omega_{\mathrm{L}}^{\pm} = (\omega_m - \omega_n) \pm (\nu + \delta_j + \Delta\delta_j(t)) + (\chi_m + \Delta\chi_m(t)) - (\chi_n - \Delta\chi_n(t))$. For the electronic coupling interaction, we set $\Delta\omega_{\mathrm{L}} = (\omega_m - \omega_n) + (\chi_m + \Delta\chi_m(t)) - (\chi_n + \Delta\chi_n(t))$. Moving to an interaction picture with these detunings, the simulation Hamiltonian becomes

$$H^{\mathrm{sim}} = \sum_{j=1}^{3N}(\delta_j + \Delta\delta_j(t))a_j^\dagger a_j + \sum_{n=0}^{d-1}(\chi_n + \Delta\chi_n(t))\,|n\rangle\langle n| + \sum_{n\neq m}\Omega'_{n,m}\,|n\rangle\langle m| + \sum_n\sum_{j\in\mathbf{t}}\Theta'_{n,j}(a_j^\dagger + a_j)\,|n\rangle\langle n| + \sum_{n\neq m}\sum_{j\in\mathbf{c}}\Omega'_{n,m,j}(a_j^\dagger + a_j)\,|n\rangle\langle m|\,. \tag{3.18}$$

H^{sim} contains stochastic terms of the form in eq. (3.15), from which we can retrieve the induced dephasing rates. Vibrational dephasing for mode j is obtained by setting $O = a_j^\dagger a_j$

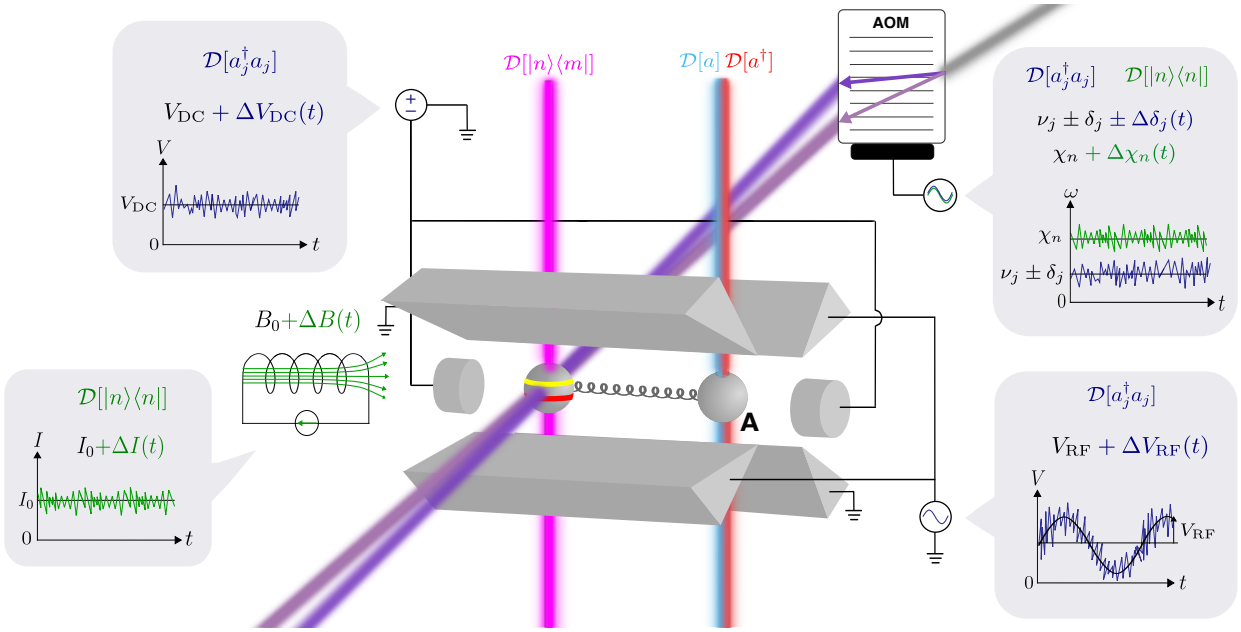

Figure 3.3: Simulating MQB open-system molecular dynamics in an ion trap. The ions (spheres) are trapped in vacuum in a linear chain by two DC (end caps) and four RF electrodes (triangular blades). The closed-system simulation is achieved using a qudit ion representing the molecular electronic states (yellow $|m\rangle$ and red $|n\rangle$ lines) and collective ion vibrational modes (grey spring) representing molecular vibrations. Vibronic coupling is simulated with a bichromatic laser field (two shades of purple) originating from a single incident laser (grey) modulated by an AOM. An open-system simulation requires an ancilla ion (A) (which shares vibrational modes with the qudit ion) and controllable implementations of the four Lindblad dissipators: $\mathcal{D}[|n\rangle\langle m|]$ (pink) can be injected via optical pumping; $\mathcal{D}[a_j]$ (light blue) and $\mathcal{D}[a_j^\dagger]$ (red) can be achieved using blue- and red-sideband interactions; $\mathcal{D}[|n\rangle\langle n|]$ (green), can be injected in two ways: (1) using a noisy detuning ($\Delta\chi_n$) in the vibronic-coupling laser or (2) using a noisy current ΔI to fluctuate the magnetic field ($B_0+\Delta B$); and $\mathcal{D}[a_j^\dagger a_j]$ (dark blue) can also be implemented in two ways: (1) using a fluctuating detuning $\Delta\nu_j$ in the vibronic-coupling laser or (2) using noisy voltages $\Delta V_{\rm RF}$ and $\Delta V_{\rm DC}$ on the electrodes.

and $\Delta\Phi(t) = \Delta\delta(t)$, resulting in rate $\gamma_{{\rm v},j}^{\rm inj} = \langle\Delta\delta_j(t)^2\rangle\tau_c/2$. Similarly, electronic dephasing involving qudit level n is obtained by setting $O = |n\rangle\langle n|$ and $\Delta\Phi(t) = \Delta\chi_n(t)$, resulting in rate $\gamma_{{\rm e},n}^{\rm inj} = \langle\Delta\chi_n(t)^2\rangle\tau_c/2$. The total electronic dephasing rate between levels n and m is then $\gamma_{nm}^{\rm inj} = \gamma_{{\rm e},n}^{\rm inj} + \gamma_{{\rm e},m}^{\rm inj}$. Because the magnitudes of the fluctuations and their correlation times are independently controlled, the dephasing rate of each mode and electronic level is independently programmable.

When engineering dephasing, large frequency fluctuations in the laser fields may cause unwanted off-resonant couplings to other vibrational modes. These couplings can be minimized by increasing τ_c, which leads to a smaller variance of the noise, or by choosing ion trap parameters which increase the frequency spacings between the vibrational modes.

Global electronic dephasing by magnetic field fluctuations

A simplified injection of electronic pure dephasing can be implemented if all electronic states involved in the simulation are affected by global stochastic frequency fluctuations, creating

similar pure dephasing rates. As in section 3.5.2, this scheme can be used to simulate open systems for which there is not enough information about the pure dephasing rate of each electronic state. Assuming that different electronic states experience similar pure dephasing rates can be a satisfactory approximation in these cases.

Global dephasing can be implemented using fluctuating magnetic fields ΔB, which alter the energies of magnetically sensitive electronic states. To first order in ΔB, the fluctuation in the nth electronic energy is [88]

$$\Delta\omega_n = \left(\frac{d\omega_n}{dB}\right)_{B_0} \Delta B, \tag{3.19}$$

where $(d\omega_n/dB)_{B_0}$ is the sensitivity at the average field B_0. The fluctuation ΔB can be engineered using a noisy current ΔI in the magnetic field source, such that $\Delta B = (dB/dI)\Delta I$. For cylindrical solenoids, the typical source of magnetic fields in ion traps, $dB/dI = C\mu_0/L$, where C is the number of windings, L is the length of the solenoid, and μ_0 is the vacuum permeability. Using eq. (3.19), eq. (3.17) gives the injected dephasing rate,

$$\gamma_{\mathrm{e},n}^{\mathrm{inj}} = \frac{1}{2}\left(\frac{d\omega_n}{dB}\frac{dB}{dI}\right)^2 \langle \Delta I^2 \rangle \tau_c. \tag{3.20}$$

For these rates to be similar, one needs to find electronic states with similar $d\omega_n/dB$. For states that are linearly sensitive to the magnetic field, $d\omega_n/dB$ is proportional to the projection of the total angular momentum onto the quantisation axis (m_J), which allows states of similar m_J to be selected as the qudit states. In particular, hyperfine states within the same angular momentum manifold experience similar sensitivities [98].

Global vibrational dephasing by trapping voltage fluctuations

Similarly to electronic dephasing in the previous section, the same (or similar) vibrational pure dephasing rates are often assumed to affect all modes in an open molecule [179–181]. This global dephasing can be implemented by injecting noise into the strength of the ions' confining potentials, which control the vibrational mode frequencies. This injection can be achieved by inducing voltage fluctuations in the electrodes that create the confining electric fields (fig. 3.3).

The ions' vibrational frequencies are determined by the three-dimensional electric fields produced by the four radio-frequency (RF) and two static (DC) electrodes (fig. 3.3). The blade electrodes, with RF signal of peak voltage $V_{\mathrm{RF}}^{(0)}$ produce a radially confining potential (in the xy plane), while the end caps with DC voltage V_{DC}^{0} confine the ions axially (along z). A chain of N ions has $3N$ vibrational modes, of which the radial frequencies $\nu_{r,i}$ are determined by the RF voltage, while the axial frequencies $\nu_{z,i}$ by the DC voltage. One can relate the vibrational frequencies to the center-of-mass frequencies $\nu_{r,0}$ and $\nu_{z,0}$ using geometric factors: $\nu_{r,i} = \kappa_{r,i}\nu_{r,0}$ and $\nu_{z,i} = \kappa_{z,i}\nu_{z,0}$ [88], where $\kappa_{r,i}$ and $\kappa_{z,i}$ are typically of the same order of magnitude for all i [198].

		Triiodide ($F = 1.6 \times 10^{-11}$)			Pyrazine ($F = 2.6 \times 10^{-11}$)		
Dissipation	$\gamma_i^{\text{nat}}/\text{s}^{-1}$	$\gamma_i^{\text{mol}}/\text{ps}^{-1}$	$\gamma_i^{\text{sim}}/\text{s}^{-1}$	Imp. (kHz)	$\gamma_i^{\text{mol}}/\text{ps}^{-1}$	$\gamma_i^{\text{sim}}/\text{s}^{-1}$	Imp. (kHz)
Elec. relaxation	0	0	0	$\Omega_{ml}/2\pi = 0$	0	0	$\Omega_{ml}/2\pi = 0$
Vib. cooling	0.20 [105]	0.52 [21]	8.6	$\eta\Omega_-/2\pi = 11$	1.0 [179]	27	$\eta\Omega_-/2\pi = 20$
Vib. heating	0.20 [105]	0.31 [21]	5.0	$\eta\Omega_+/2\pi = 8.5$	0.0077 [179]	0.20	$\eta\Omega_+ = 0$
Vib. dephasing	29 [105]	1.8 [21]	29	$\sqrt{\langle\Delta\delta_j^2\rangle}/2\pi = 0$	2.1 [181]	55	$\sqrt{\langle\Delta\delta_j^2\rangle}/2\pi = 2.3$
Elec. dephasing	0.12 [199]	120 [21]	2000	$\sqrt{\langle\Delta\chi_n^2\rangle}/2\pi = 20$	33 [180]	870	$\sqrt{\langle\Delta\chi_n^2\rangle}/2\pi = 13$

Table 3.1: Dissipation rates γ_i^{mol} and the corresponding simulated rates $\gamma_i^{\text{sim}} = F\gamma_i^{\text{mol}}$ in an ion-trap MQB simulator for triiodide in solution [21] and for a 3-mode, 2-state pyrazine molecule where the dissipation is due to the other vibrational modes. The column "Imp." denotes experimental parameters for implementing γ_i^{sim}.

Small voltage fluctuations change the vibrational frequencies according to the corresponding sensitivities:

$$\Delta\nu_{r,i} = \left(\frac{d\nu_{r,i}}{dV_{\text{RF}}}\right)_{V_{\text{RF}}^{(0)}} \left(V_{\text{RF}} - V_{\text{RF}}^{(0)}\right), \tag{3.21}$$

$$\Delta\nu_{z,i} = \left(\frac{d\nu_{z,i}}{dV_{\text{DC}}}\right)_{V_{\text{DC}}^{(0)}} \left(V_{\text{DC}} - V_{\text{DC}}^{(0)}\right). \tag{3.22}$$

We therefore obtain the injected pure dephasing rates,

$$\gamma_{\text{v},r,i}^{\text{inj}} = \frac{1}{2}\kappa_{r,i}^2 \left(\frac{d\nu_{r,}}{dV_{\text{RF}}}\right)^2 \langle\Delta V_{\text{RF}}^2\rangle\tau_c, \tag{3.23}$$

$$\gamma_{\text{v},z,i}^{\text{inj}} = \frac{1}{2}\kappa_{z,i}^2 \left(\frac{d\nu_{z,0}}{dV_{\text{DC}}}\right)^2 \langle\Delta V_{\text{DC}}^2\rangle\tau_c. \tag{3.24}$$

Therefore, global pure vibrational dephasing can be implemented if all of the geometric factors κ are sufficiently close to each other. The variances of the pure dephasing of axial and radial modes can be separately tuned by varying the amplitudes of the DC and RF voltage fluctuations, respectively.

3.6 Examples

We apply our method to two well-studied examples of open-molecular systems: (1) triiodide in a polar solvent, and (2) pyrazine modelled as an LVC system with dissipative dynamics due to its intramolecular vibrational modes. In both examples, we use molecular Lindblad dissipation rates determined in earlier works and map them to equivalent rates in an experimentally realistic trapped-ion MQB simulator.

Our approach requires predetermined Lindblad dissipation rates for the open system of interest, which are obtainable from time-resolved spectroscopy, simulations on classical computers, or a combination of both. For example, time-resolved spectroscopic experiments often report population decay and dephasing times T_1 and T_2, respectively, for both electronic states and

vibrational modes. The electronic pure dephasing rate is then given by $\gamma_{\mathrm{e},n}^{\mathrm{mol}} = 1/T_{2\mathrm{e}} - 1/2T_{1\mathrm{e}}$, where the electronic dephasing time $T_{2\mathrm{e}}$ can be obtained from fitting the electronic time-dependent spectra [181]. $T_{1\mathrm{e}}$ is extracted from the radiative quantum yield $Y_R = T_{1\mathrm{e}}\gamma_{nm}^{\mathrm{mol}}$ [181], where the radiative electronic relaxation rate is determined by the strength of the transition dipole moment $|m\rangle \to |n\rangle$ [181]. The analogous vibrational times $T_{2\mathrm{v}}$ and $T_{1\mathrm{v}}$—also obtainable from time-dependent spectroscopy—determine $\gamma_{-,j}^{\mathrm{mol}} - \gamma_{+,j}^{\mathrm{mol}} = 1/T_{1\mathrm{v}}$ and $\gamma_{\mathrm{v},j}^{\mathrm{mol}} = 1/T_{2\mathrm{v}} - 1/2T_{1\mathrm{v}}$ [21].

Triiodide in a polar solvent

Triiodide gained interest after time-resolved spectroscopic experiments of its photodissociation dynamics in the condensed phase showed the vibrational decoherence effects of solvents [19–21]. In particular, the key role of the symmetric stretch mode ν_1 at $112\,\mathrm{cm}^{-1}$ makes it ideal for probing solvent effects on the dynamics.

The relevant dissipation rates were measured by pumping the molecule to a dissociative electronic surface and then monitoring the solvent-induced vibrational dissipation using time-delayed probe pulses. The resulting spectrum was fitted to a decaying sine function to obtain the vibrational relaxation and dephasing times $T_{1\mathrm{v}}$ and $T_{2\mathrm{v}}$ [21, 200]. The electronic dephasing rate was also chosen to fit the spectral modulations. The ranges of the corresponding dissipation rates obtained for water and ethanol solvents are given in fig. 3.1. Radiative electronic relaxation was not included because it is much slower than the other processes.

These measured rates can be mapped onto an MQB simulator. Table 3.1 shows the average of the dissipative rates in water and ethanol and gives examples of typical native dissipation rates γ_i^{nat} for an Yb^+ trapped-ion simulator [105, 106]. We select the scaling factor F as described in section 3.3 to minimise the injected dissipation. In this example, vibrational pure dephasing determines $F = \gamma_{\mathrm{v},r}^{\mathrm{nat}}/\gamma_{\mathrm{v},1}^{\mathrm{mol}} = 1.6 \times 10^{-11}$, so that no injection of this dissipation type would be required. F is then used to scale the other rates γ_i^{sim} in table 3.1. Electronic and vibrational dephasing, occurring on timescales of tens and hundreds of femtoseconds, respectively, would affect the MQB dynamics on 1–30 ms timescales. Vibrational dissipation would be mapped from a picosecond in the molecule to 0.1 s in the ion trap.

All calculated parameters for simulating γ_i^{sim} are within existing experimental capabilities, for which we have used representative values from past ion-trap MQB simulations [11, 105, 106]. The interaction strength $\eta\Omega_-/2\pi = 11\,\mathrm{kHz}$, and therefore also the smaller Ω_+, are well within the range achievable by tuning the laser power [201]. Ω_- is calculated from eq. (3.12), using $\Gamma_{pq}^A/2\pi = 20\,\mathrm{MHz}$ and $\nu_x/2\pi = 1.34\,\mathrm{MHz}$, values reported for an Yb^+ ion trap [105]. Ω_+ is obtained from the Boltzmann factor using $\nu_1 = 112\,\mathrm{cm}^{-1}$ and $T^{\mathrm{mol}} = 300\,\mathrm{K}$ [21]. The fluctuations for injecting electronic dephasing, $\sqrt{\langle\Delta\chi_n^2\rangle}\,/2\pi = 20\,\mathrm{kHz}$, could be imprinted on the frequency of each Raman beam using an AOM. The electronic dephasing rate $\gamma_{\mathrm{e},n}^{\mathrm{sim}}$ is

determined using eq. (3.17), where the correlation time τ_c must be chosen much smaller than the dephasing timescale; we choose $\tau_c = 10\,\mu s \ll 1/\gamma_{e,n}^{sim} = 500\,\mu s$. This choice is well within the capabilities of modern control electronics, which achieves temporal resolutions of 100 ns.

Pyrazine

Pyrazine is widely used for studying ultrafast nonadiabatic dynamics due to the conical intersection between its excited electronic states [46]. This 24-mode molecule has been successfully modelled as an open quantum system in which three vibrational modes, one coupling (ν_{10a}) and two tuning (ν_1 and ν_{6a}), are coupled to the first two excited electronic states, $n\pi^*$ and $\pi\pi^*$, while the remaining 21 modes form a weakly coupled environment that leads to dissipative dynamics [180].

As in the triiodide example, dephasing and relaxation constants for electronic states and vibrational modes were retrieved from fitting the experimental absorption spectrum [154, 156, 180, 181]. Radiative electronic relaxation from $\pi\pi^*$ to $n\pi^*$ is forbidden and not included. The pure dephasing constant for the state $\pi\pi^*$ was $T^*_{2,\pi\pi^*} = 30\,fs$. We assume that the constants $T_{1v} = 1\,ps$ [154, 156] and $T_{2v} = 320\,fs$ [180] are the same for all modes.

Using the procedure above, we converted the dissipation times into the Lindblad rates and mapped them to the simulator dissipative rates (table 3.1). In particular, we use the tuning mode $\nu_1 = 1016\,cm^{-1}$ to exemplify the Lindblad rates for the vibrations. In this case, F comes from the vibrational heating of this tuning mode, $F = \gamma^{nat}_{+,r}/\gamma^{mol}_{+,1} = 2.6 \times 10^{-11}$, which, along with the ν_{6a} and ν_{10a} modes, would not require dissipation injection, i.e., $\Omega_+ = 0$. The other Lindblad rates are scaled as before, $\gamma_i^{sim} = F\gamma_i^{mol}$. The experimental parameters for dissipation injection (including single-mode schemes) are calculated as in the triiodide example and reported in table 3.1. In this case, vibrational cooling could also be implemented globally by targeting the vibrational modes with one broadband laser interaction, such that the laser power is adjusted to $\Omega_- = 20\,kHz$. The global vibrational dephasing scheme would also be suitable, with fluctuations $\sqrt{\langle \Delta\nu_r^2 \rangle}\,/2\pi = 2.3\,kHz$ produced via trapping potential fluctuations ΔV_{RF}.

3.7 Discussion

Our approach extends molecular MQB simulation from closed systems to open ones, the latter characterised by the most common set of Lindblad dissipators used in chemistry. Dissipation can be included in the simulation using a combination of native and injected dissipation, an approach that turns native dissipation into a valuable resource for analog simulation. In addition, injected

dissipation, described for trapped-ion systems, could be readily implemented using available simulators with few additional hardware modifications and independently of the molecular size.

Using native noise as a simulation resource diminishes the common argument that the accumulation of errors makes analog simulators impractical. Dissipation and decoherence are the main sources of error in analog devices—quantum or classical—and limit the simulation time. However, analog classical simulations were, despite errors, essential for classical computation before large-scale digital computers [202]. Similarly, successful quantum simulations of closed systems [105, 106] have shown that available decoherence times in analog quantum simulators are sufficiently low to allow accurate simulations, up to hundreds of femtoseconds on molecular timescales, which are the most relevant for photochemistry. Here, we have shown that harnessing a simulator's native noise as a resource *always* extends the possible simulation times, up to picoseconds on molecular timescales.

The result of using noise as a resource is counterintuitive: open-system simulation, which is usually a *harder* problem than closed-system simulation, becomes an *easier* problem on an MQB simulator when Lindblad dynamics is implemented. On both classical and quantum digital computers, simulating open-system dynamics requires more resources, either to represent density matrices instead of wavefunctions or to represent the environment (or both). By contrast, on an analog simulator, if some of the noise is used for the simulation, the remaining unusable dissipation has a smaller deleterious effect, extending the possible simulation duration.

The transition from a closed to an open simulation requires minimal additional experimental cost on a trapped-ion MQB simulator. When using Raman lasers to inject dissipation, no additional hardware is required at all, since those lasers are required for the LVC simulation as well. For the other hardware we describe, such as the magnetic-field solenoid, the overhead is constant regardless of the system size (e.g., only one solenoid is needed for any molecule).

Ion traps are particularly versatile MQB simulators. The two example systems show that our approach can accommodate a wide range of molecular systems: from a small inorganic ion to a neutral organic molecule; from a polar solvent to an environment of intramolecular vibrations; different numbers of vibrational modes, with frequencies varying by an order of magnitude; global- and single-mode dissipation injection; and scaling-factor selection to minimise noise injection.

Like any LVC simulation, our scheme requires a parametrisation of the Hamiltonian in eq. (3.4). As is standard in non-adiabatic dynamics, the parameters can be obtained using a prior electronic-structure calculation. In addition, we require values of the dissipation rates; these can also be obtained from a prior calculation or by comparison with experimental results on related molecules. For systems without enough experimental information and unknown dissipative rates, our global injection schemes offer an initial approach for estimation of the

molecular dissipation effects and for the interpretation of experimental data. For example, our algorithm could be used in the quantum time-domain spectroscopy algorithm [106] to predict or explain spectral peak broadening in open molecular systems.

We expect that our approach can be extended to dissipation models more general than the Lindblad master equation. For example, non-Markovian environments include strong coupling between the molecule and the environment with long-time correlation functions [23]. One possibility for engineering a non-Markovian environment could be to inject correlated (coloured) classical noise [203] into the amplitude and phase of the laser beams used for vibronic and electronic coupling. Alternatively, a hybrid approach could be pursued, which combines our Lindblad techniques with an explicitly implemented, strongly coupled environment, implemented using additional ancillary ions [82, 83] or vibrational modes (with structured spectrum).

3.8 Conclusion

Overall, including native dissipation relaxes the experimental complexity when transitioning from closed- to open-system simulation and reduces error accumulation, allowing for longer, more accurate analog simulations of molecular dynamics. When injected dissipation is necessary, minimal hardware modifications are required. Because of the difficulty of simulating open molecular systems both classically and on digital quantum computers, these advantages position analog quantum simulation as a contender for achieving quantum advantage on a problem of practical importance.

Chapter 4: Experimental Quantum Simulation of Chemical Dynamics

This chapter is a reformatted version of the publication:
Tomas Navickas, Ryan J. MacDonell, Christophe H. Valahu, Vanessa C. Olaya-Agudelo, Frank Scuccimarra, Maverick J. Millican, Vassili G. Matsos, Henry L. Nourse, Arjun D. Rao, Michael J. Biercuk, Cornelius Hempel, Ivan Kassal, Ting Rei Tan, "Experimental Quantum Simulation of Chemical Dynamics", *J. Am. Chem. Soc.* **147**, 23566–23573 (2025).

Abstract

Accurate simulation of dynamical processes in molecules and reactions is among the most challenging problems in quantum chemistry. Quantum computers promise efficient chemical simulation, but the existing quantum algorithms require many logical qubits and gates, placing practical applications beyond existing technology. Here, we carry out the first quantum simulations of chemical dynamics by employing a more hardware-efficient encoding scheme that uses both qubits and bosonic degrees of freedom. Our trapped-ion device accurately simulates the dynamics of non-adiabatic chemical processes, which are among the most difficult problems in computational chemistry because they involve strong coupling between electronic and nuclear motions. We demonstrate the programmability and versatility of our approach by simulating the dynamics of three different molecules as well as open-system dynamics in the condensed phase, all with the same quantum resources. Our approach requires orders of magnitude fewer resources than equivalent qubit-only quantum simulations, demonstrating the potential of using hybrid encoding schemes to accelerate quantum simulations of complex chemical processes, which could have applications in fields ranging from energy conversion and storage to biology and drug design.

4.1 Introduction

Dynamics is central to chemistry because it underpins all of chemical reactivity and kinetics. However, predicting the quantum-mechanical dynamics of both nuclei and electrons involved in chemical transformations remains one of the great challenges of computational chemistry. Particularly difficult are simulations of non-adiabatic processes, where the breakdown of the Born-Oppenheimer approximation leads to the entangled motion of nuclear wavepackets on multiple potential-energy surfaces on ultrafast timescales [2, 204]. These effects are especially important in photochemistry, including almost all chemical reactions in the atmosphere, such as those responsible for smog formation and ozone depletion; interactions of organisms with light, whether through photosynthesis, vision, or UV DNA damage; solar energy conversion through solar cells; and compounds for preventing and treating disease, from sunscreens to photodynamic therapies [205].

Methods to simulate non-adiabatic dynamics on conventional, classical computers are either approximate or limited by computational scaling that is unpredictable a priori [2, 40]. Even more complicated is simulating open quantum systems, including chemical dynamics in the condensed phase [17]. On classical computers, doing so usually involves tracking density matrices (more complicated than wavefunctions) as well as the system's interactions with its environment. Classical multi-configuration time-dependent Hartree (MCTDH) calculations have been achieved for relatively small systems with explicit bath modes [40, 44, 206] or weak system-bath couplings [207], but increasing the coupling strength or the number of modes quickly becomes intractable.

Simulating chemistry on quantum computers promises to overcome the challenges faced by conventional computational techniques. Indeed, using quantum machines for simulating nature is the idea that launched quantum computing [7], because a controllable quantum device could mimic another quantum system efficiently (with polynomial resources in system size) [8]. Simulations of quantum chemistry, encompassing both electronic structure and dynamics, are particularly suited for quantum simulation and are likely to be the earliest applications of quantum computing [53, 60, 208]. Most chemical quantum algorithms have focused on finding static molecular properties, usually energies [53–57, 60, 209, 210]. By contrast, there are few quantum algorithms for molecular dynamics [61, 63, 161, 211], despite the centrality of dynamics to chemistry. To make matters worse, useful applications of those algorithms would require quantum computers with many more low-error qubits and gates than is feasible with existing technology [61, 63, 161].

The hardware costs of existing algorithms can be reduced by encoding information not only in qubits but in other degrees of freedom as well [11, 212]. This approach is particularly natural in

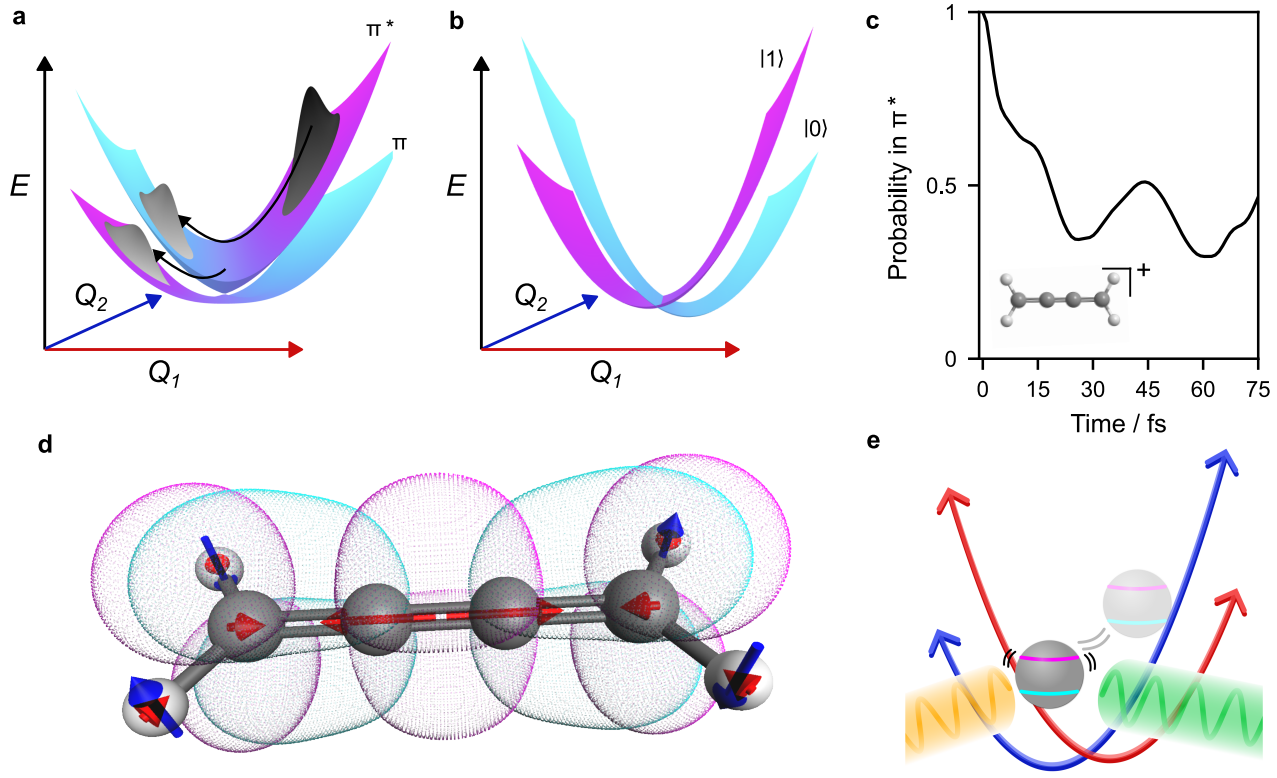

Figure 4.1: **Mapping non-adiabatic chemical dynamics onto an MQB simulator. (a)** Adiabatic potential energy surfaces (PES) of the butatriene cation determined from solving the Born-Oppenheimer Hamiltonian at all nuclear positions. The cyan and magenta regions of the surfaces correspond to π and π^* electronic characters. The two PESs intersect at a conical intersection (CI) through a coupling with the central bond stretching (Q_1) and torsion (Q_2) vibrational modes. This vibronic coupling allows ultrafast molecular dynamics: an initial wavepacket (grey, top right) on the upper surface approaches the conical intersection and splits into two entangled branches on the two electronic surfaces. **(b)** Diabatic representation of the PESs. The coupling between surfaces (not shown) is linear along Q_2. **(c)** Probability of the wavepacket remaining in the initial diabatic state π^* as a function of time. **(d)** Butatriene molecule with its electronic states represented by orbitals (pink and cyan) that differ between the two states, and the two vibrational modes Q_1 (red) and Q_2 (dark blue). **(e)** Molecular electronic and vibrational degrees of freedom can both be mapped onto a mixed qudit-boson (MQB) simulator consisting here of one trapped ion. Potentials and vibronic couplings are induced with lasers (yellow and green beams).

the context of chemical dynamics, where molecular vibrational degrees of freedom can be mapped onto bosonic hardware elements present in multiple quantum architectures [11, 82, 83, 105–107, 170, 213, 214]. Using bosons reduces hardware resource requirements compared to the alternative of using a large number of qubits to encode a single continuous degree of freedom. In particular, the mixed-qudit-boson (MQB) approach allows simulations of molecular models with vibrational-electronic (vibronic) couplings using significantly reduced quantum resources compared to qubit-only simulations [11, 214]. This is achieved using qudits (d-level quantum systems) controllably coupled to bosonic modes to encode, respectively, molecular electronic states and nuclear vibrations (Fig. 4.1). MQB simulators based on trapped-ion systems have been used to predict vibronic spectra and to observe the dynamical geometric-phase interference around an engineered conical intersection [105–107, 215]. Previous experimental quantum

simulations of chemical dynamics were important but limited demonstrations, restricted to non-molecular model Hamiltonians or being non-programmable. A programmable MQB simulator would allow tunable experimental parameters to simulate a wide range of molecules using the same hardware.

Here, we perform the first programmable MQB simulations of non-adiabatic photochemical dynamics using a trapped-ion system. We demonstrate the programmability of the simulator by reproducing the real-time molecular dynamics of three different photoexcited molecules—the allene cation, the butatriene cation, and pyrazine—encoded using different parameters in a vibronic-coupling Hamiltonian. In each molecule, the vibronic couplings give rise to a conical intersection, which allows ultrafast (femtosecond) population transfer between electronic states [2, 204]. Experimental measurements reliably reproduce the expected chemical dynamics, including signatures of the conical intersections. We further demonstrate the extensibility of our simulator to open-system dynamics by implementing simulations of pyrazine coupled to a thermal bath, showing the expected damping of coherent effects and thermalization. Our results further demonstrate the hardware efficiency of MQB simulation: with one trapped-ion qudit, two vibrational modes, and one laser pulse, it achieves a computation that would require 11 qubits and over 10^5 entangling gates in a standard qubit-only framework.

4.2 MQB simulation of photochemistry

In an ion-trap MQB simulator, molecular vibrations and electronic states are encoded in motional and electronic degrees of freedom of the trapped ion [11] (Fig. 4.1). We simulate non-adiabatic dynamics in an analog fashion by reconstructing the time evolution of important molecular properties, rescaled to a timescale accessible by the simulator. Typically, temporal dynamics are rescaled from femtoseconds to milliseconds—i.e., by a factor of approximately 10^{11}—sufficient to enable direct probing with conventional electronics and laser systems.

To represent molecular systems, MQB simulators use vibronic coupling (VC) Hamiltonians [11], which are widely used to represent potential energy surfaces and their couplings. The parameters of a VC Hamiltonian can be obtained beforehand using electronic-structure theory. While here we address the challenge of simulating the dynamics generated by VC Hamiltonians, the parametrisation of the Hamiltonian can pose a separate challenge itself, which we discuss further below. Alternatively, electronic degrees of freedom can be included in the simulation using a fermion-to-qubit encoding without the need to parametrise a VC Hamiltonian [216].

Our simulation of molecular dynamics comprises three stages (Fig. 4.2). First, the initial wavefunction is prepared by exciting the qudit and displacing the relevant motional modes. Second, using laser-ion interactions with frequencies and intensities chosen to reproduce the

molecular VC Hamiltonian, the simulator is evolved for some duration. Third, desired observables are measured. This process is repeated for varying evolution durations, allowing the reconstruction of observables as a function of time.

We simulate the photoinitiated non-adiabatic dynamics in three molecules: photoionised allene ($C_3H_4^+$), photoionised butatriene ($C_4H_4^+$), and photoexcited pyrazine ($C_4N_2H_4$). The three molecules exhibit a wide variety of photochemical dynamics due to differences in their potential energy surfaces (see Fig. 4.3a-c). Allene is photoionised to a degenerate pair of π states that are coupled via symmetry-breaking vibrational modes: bond alternation and torsion [217]. The potential is thus symmetric about the conical intersection along both vibrational modes. Butatriene is photoexcited to the cationic π^* state, coupled to the π state through central bond stretching and torsion [218, 219]. Both electronic potential-energy surfaces are displaced along the bond-stretching mode, leading to a peaked conical intersection, i.e., one where the lower adiabatic surface decreases in energy in all directions away from the intersection. Finally, pyrazine is photoexcited to the bright (large transition dipole moment) $\pi\pi^*$ state and decays to the dark $n\pi^*$ state, and its dynamics is dominated by a ring breathing mode and an out-of-plane hydrogen wag [220, 221]. The resulting Hamiltonian leads to a sloped conical intersection, where the lower adiabatic potential energy increases in one direction (here, $-Q_1$).

Each of the three molecules is well described by a linear VC (LVC) model, where the two electronic states and the two vibrational modes are linearly coupled. Denoting the initially excited electronic state as $|1\rangle$ (and the other one as $|0\rangle$), the Hamiltonian is [11]

$$\hat{H}_{\text{mol}} = -\tfrac{1}{2}\Delta E\hat{\sigma}_z + \sum_j \omega_j \hat{a}_j^\dagger \hat{a}_j + \frac{\kappa}{\sqrt{2}}\hat{\sigma}_z(\hat{a}_1^\dagger + \hat{a}_1) + \frac{\lambda}{\sqrt{2}}\hat{\sigma}_x(\hat{a}_2^\dagger + \hat{a}_2), \tag{4.1}$$

where $\hat{\sigma}_{x,z}$ are the Pauli operators and $\hat{a}_j$ is the annihilation operator of the jth mode with frequency ω_j. ΔE is the energy difference between the two electronic states, while κ and λ are the tuning and coupling parameters, respectively. The initial wavefunction is a coherent state displaced along the mode $j = 1$ by $\hat{D}_1(\alpha) = \exp(\alpha\hat{a}_1^\dagger - \alpha^*\hat{a}_1)$. The parameter values for each molecule are given in table 4.1.

4.3 Trapped-ion simulation

Each term in the LVC Hamiltonian $\hat{H}_{\text{mol}}$ can be implemented on a trapped-ion MQB simulator consisting of a qubit (qudit with $d = 2$) representing the electronic states of the molecule and two motional modes of the ion in its harmonic confining potential representing the vibrations (Fig. 4.1e) [11]. This correspondence between molecular and trapped-ion Hamiltonian terms underpins the straightforwardness of our simulation approach. The vibronic couplings are implemented by tunable, laser-driven spin-dependent forces (SDF) in the Lamb-Dicke regime [11],

which drive the motional modes depending on the state of the qubit. After interaction-frame transformations and rotating-wave approximations [11, 88], the Hamiltonian for interactions involving mode j is

$$\hat{H}^{\mathrm{SDF}}_{j,\phi_s}(\delta,\Omega) = \frac{\Omega}{2}\left(\hat{\sigma}_x\cos\phi_s + \hat{\sigma}_y\sin\phi_s\right)\left(\hat{a}_j^\dagger + \hat{a}_j\right) + \delta\hat{a}_j^\dagger\hat{a}_j, \tag{4.2}$$

where $\hat{\sigma}_{x,y,z}$ are the Pauli matrices, ϕ_s is a phase that determines the qubit operator, which can be adjusted by the laser phase, Ω is the Rabi frequency that is tuneable with the laser intensity, and δ is the adjustable detuning of the laser frequency from the motional mode. We use the notation $\hat{H}^{\mathrm{SDF}}_{j,x}$ and $\hat{H}^{\mathrm{SDF}}_{j,y}$ for interactions where $\phi_s = 0$ and $\phi_s = \pi/2$, respectively. An SDF interaction in the $\hat{\sigma}_z$ basis can be obtained with a qubit basis rotation, $\hat{H}^{\mathrm{SDF}}_{j,z} = \hat{R}_x(\pi/2)\hat{H}^{\mathrm{SDF}}_{j,y}\hat{R}_x(-\pi/2)$, where $\hat{R}_x(\theta)$ are laser-driven qubit rotations around the x-axis of the Bloch sphere. We can also implement a Hamiltonian that generates a qubit rotation around $\hat{\sigma}_z$ by sandwiching a laser-driven interaction $\hat{H}^{\mathrm{Q}}_y(\chi) = \chi\hat{\sigma}_y/2$ between two $\hat{R}_x$ rotations, i.e., $\hat{H}^{\mathrm{Q}}_z = \hat{R}_x(\pi/2)\hat{H}^{\mathrm{Q}}_y\hat{R}_x(-\pi/2)$, where the Rabi frequency χ is tuneable using the laser's power.

$\hat{H}_{\mathrm{mol}}$ is experimentally implemented by simultaneously driving two SDF interactions and a qubit rotation, resulting in the ion Hamiltonian $\hat{H}_{\mathrm{ion}} = F\hat{H}_{\mathrm{mol}}$, where the scaling factor F scales molecular frequencies (THz) and timescales (ps) to the trapped ion's frequencies (MHz) and timescales (ms). Overall,

$$\hat{H}_{\mathrm{ion}} = \hat{H}^{\mathrm{SDF}}_{1,z}(F\omega_1, \sqrt{2}\,F\kappa) + \hat{H}^{\mathrm{SDF}}_{2,x}(F\omega_2, \sqrt{2}\,F\lambda) + \hat{H}^{\mathrm{Q}}_z(-F\Delta E). \tag{4.3}$$

All parameters of eq. (4.3) (ω_1, ω_2, κ, λ, and ΔE) are programmable and can be set to simulate any two-state, two-mode LVC molecule. To obtain faster ion-trap dynamics, F is maximised within the constraint of the available laser power [11, 214].

4.3.1 Closed-system experiment

We perform our experiment with a single $^{171}\mathrm{Yb}^+$ ion electromagnetically held in vacuum with a quadrupole ion trap [105, 106]. A combination of radio-frequency and static electric fields confine the ion and give rise to secular vibrational motions with frequencies $\{\omega_x, \omega_y, \omega_z\} = 2\pi \times \{1.33, 1.51, 0.5\}$ MHz. These vibrations are harmonic to an excellent approximation. We encode the two molecular electronic states into the two magnetically insensitive hyperfine levels of the ion's $^2\mathrm{S}_{1/2}$ ground state, with labels $|0\rangle \equiv |F=0, m_F=0\rangle$ and $|1\rangle \equiv |F=1, m_F=0\rangle$. The molecular vibrational modes, B_1 and B_2, are encoded in the vibrational modes along the radial x and y directions.

The experimental sequence for enabling the direct simulation of photochemical dynamics in the time domain is shown in Fig. 4.2 (methods are detailed in [105, 106]). We program the experiment with parameters of $\hat{H}_{\mathrm{ion}}$ chosen according to table 4.1 to implement each of the three

	Allene [217]	Butatriene [219]	Pyrazine [221]
$\|1\rangle$	π_x	π^*	$\pi\pi^*$
$\|0\rangle$	π_y	π	$n\pi^*$
$\omega_1/2\pi$ (THz)	22.5	62.9	17.9
$\omega_2/2\pi$ (THz)	57.3	22.0	28.5
$\Delta E/2\pi$ (THz)	0	131.5	199
$\kappa/2\pi$ (THz)	74.7	62.1	-30.7
$\lambda/2\pi$ (THz)	67.7	69.6	63.3
α	0	-0.140	0.210
$F/10^{-11}$	1.08	1.10	1.33

Table 4.1: **Parameters of the LVC Hamiltonian $\hat{H}_{\text{mol}}$,** through which the MQB simulator can be programmed to simulate different molecules. $|0\rangle$ and $|1\rangle$ are the two relevant electronic states of the molecule. ω_1 and ω_2 are the frequencies of the two vibrational modes. ΔE is the energy difference between the electronic states at the origin. κ and λ are the tuning and coupling parameters, respectively. α is the displacement of the initial wavepacket. Parameters programmed on the MQB simulator are obtained by scaling the molecular frequencies by F. All molecular parameters are literature values obtained from electronic-structure calculations [217, 219, 221].

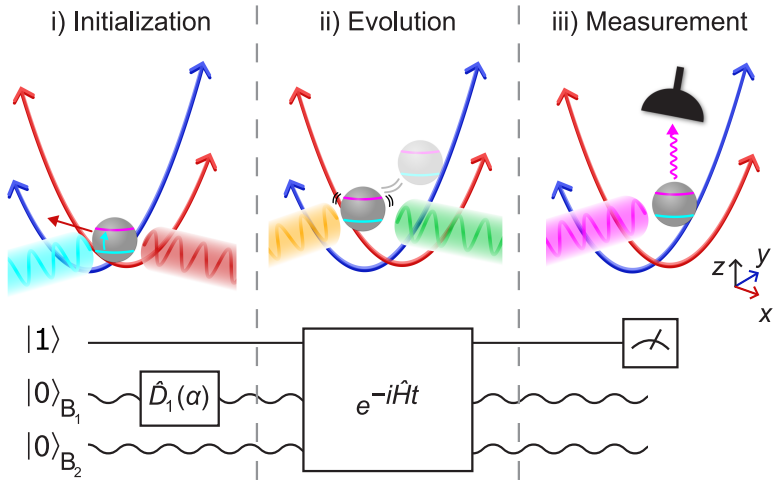

Figure 4.2: **Experimental implementation of an MQB simulator for chemical dynamics.** Three stages of MQB dynamics simulation: i) initialization, ii) evolution, and iii) measurement. Top row: trapped ion during each stage, with colors and symbols as in Fig. 4.1. Bottom row: circuit diagram of the pulse sequence acting on the qubit and two modes B_1 and B_2 (wavy lines). **i)** During initialization, the qubit is prepared in state $|1\rangle$ and the vibrational modes are prepared in their ground states. Then, B_1 is displaced by $\hat{D}_1(\alpha)$ using a state-dependent force enacted by laser beams (cyan and red). **ii)** During evolution, the Hamiltonian is applied for duration t using state-dependent forces enacted by laser beams (yellow and green). **iii)** The electronic state is measured using a photon counter through state-dependent fluorescence (pink).

target molecules. In each case, the scaling factor F is chosen to be $F = \Omega_1/\sqrt{2}\,\kappa$, where Ω_1 is the Rabi frequency of the SDF interaction of eq. (4.2) with mode B_1. The specific implementation of each simulation follows the three-stage process introduced above. First, initialization prepares the qubit in $|1\rangle$ and the modes in their ground states, followed by displacing B_1 by $\hat{D}_1(\alpha)$. Second, the system is evolved by applying $\hat{H}_{\text{ion}}$ for an experimentally variable duration t_{ion},

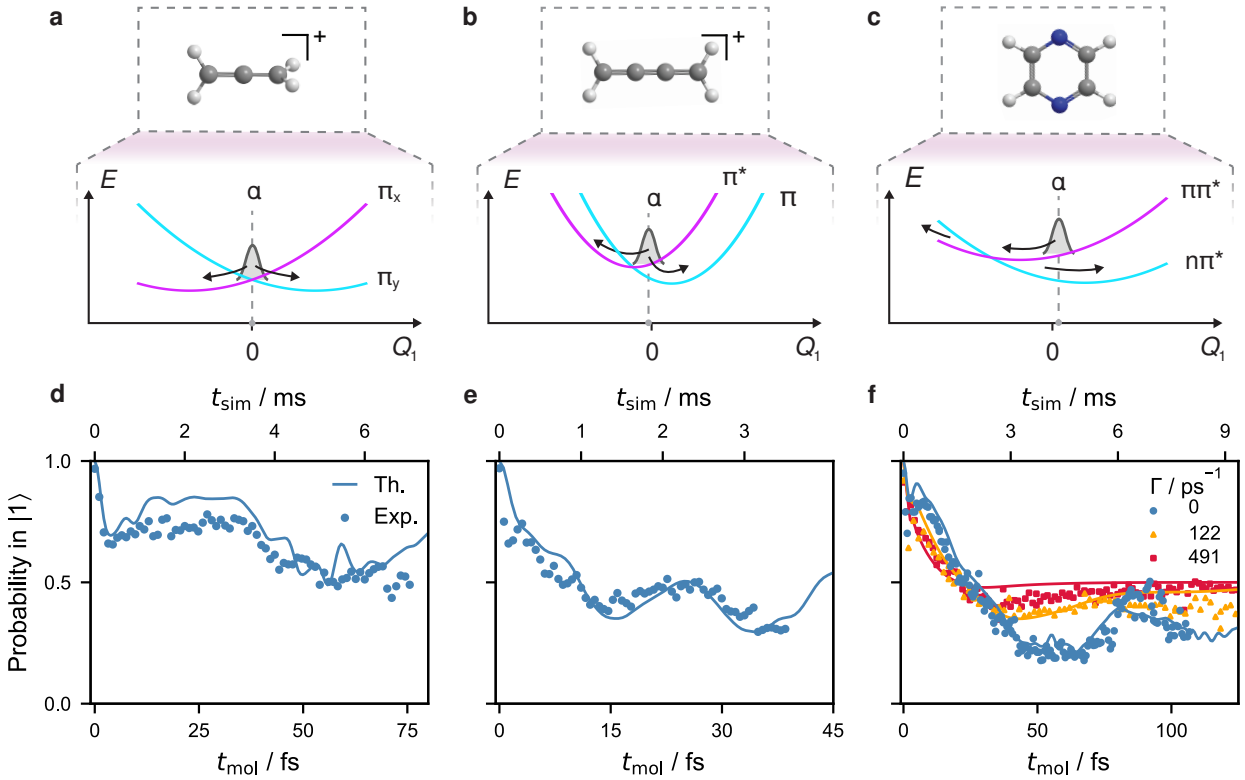

Figure 4.3: **Quantum simulation of photochemical dynamics in (a,d) photoionised allene, (b,e) photoionised butatriene, and (c,f) photoexcited pyrazine. (a–c)** Potential energy surfaces of each molecule (one-dimensional slice at $Q_2 = 0$; diabatic states in pink and cyan), with the wavepacket (gaussian width not to scale) initialised by displacement to $Q_1 = \alpha$. Each molecule results in a distinct energy landscape, where the conical intersection is (a) symmetric, (b) peaked, and (c) sloped. Black arrows indicate possible pathways for wavepackets to evolve on the PESs. **(d–f)** Corresponding molecules are simulated on an ion-trap MQB simulator using the LVC Hamiltonian of eq. (4.3) with parameters from table 4.1. The probability of finding the wavepacket in the initial diabatic state as a function of the molecular evolution time (bottom axes). Additionally, in (f), open-system dynamics of pyrazine under heating and cooling dissipation with varying rates Γ. Solid lines are the solutions of the Schrödinger equation for closed-system dynamics and of the master equation (eq. (4.4)) for open-system dynamics. The simulator times shown in the top axes correspond to the closed-system dynamics. The scaling factors for the open-system dynamics with $\Gamma = \{122, 491\}$ ps^{-1} are $F = \{1.69, 1.24\} \times 10^{-11}$. Experimental data points are obtained by averaging over $M = 500$ measurement results. Error bars of probabilities (P) are due to quantum projection noise, calculated from the binomial distribution as $\sigma = \sqrt{P(1-P)/M}$, and are smaller than the plot markers.

which is related to the molecular timescale by $t_{\text{mol}} = F t_{\text{ion}}$. Third, measurement of the electronic populations is achieved by making a $\hat{\sigma}_z$ measurement on the qubit through state-dependent fluorescence [222].

Experimental measurements of the probability of finding the wavepacket in the initial diabatic state as a function of evolution time are shown in Fig. 4.3d-f. For all three molecules, experiments match the predicted dynamics arising from conventional calculations. Small discrepancies are due to miscalibrated experimental parameters and hardware noise. In all cases, we observe a population decay due to the strong coupling between electronic states in the region of the initial wavefunction. We further observe distinct behaviors for each molecule, caused by the different potential-energy surfaces. The symmetric conical intersection of the allene cation causes a

rapid decay of the population because the initial state is at the point of strongest coupling between electronic states; however, only a small amount of population is transferred due to the degeneracy of the π states. The initial geometry of allene is located at a region of strong coupling between electronic states, which causes a rapid initial decay; however, the π states are energetically equivalent, so no more than half the population is transferred. The butatriene cation likewise has an initial state with strong coupling, but the lower potential energy minimum of the π state favours a greater overall population transfer. Finally, the location of the pyrazine $\pi\pi^*$ minimum near its intersection with the $n\pi^*$ state leads to a near-complete occupation of the $n\pi^*$ state; however, the greater distance to the intersection leads to slower initial dynamics.

4.3.2 Open-system experiment

To further demonstrate the versatility of the MQB approach, we perform a quantum simulation of open-system vibronic dynamics, which enables the simulation of environmental molecular conditions. To do so, we externally inject noise into the same single-ion simulation above. Doing so shows that what is classically a harder computational problem can be solved using the same quantum resources on an MQB simulator [173, 214].

In particular, we simulate the non-equilibrium ultrafast dynamics of a pyrazine molecule interacting with a thermal bath. The dissipation is simulated by simultaneously injecting heating and cooling of the vibrational modes, described by the Lindblad master equation [150, 223],

$$\frac{d\hat{\rho}}{dt} = -i[\hat{H}_{\text{ion}}, \hat{\rho}] + \sum_j \left(\gamma_{+,j} \mathcal{D}[\hat{a}_j^\dagger]\hat{\rho} + \gamma_{-,j} \mathcal{D}[\hat{a}_j]\hat{\rho} \right), \tag{4.4}$$

where $\mathcal{D}[\hat{a}_j^\dagger]$ is the heating dissipator for mode j,

$$\mathcal{D}[\hat{a}_j^\dagger]\hat{\rho} = \hat{a}_j^\dagger \hat{\rho} \hat{a} - \tfrac{1}{2}\{\hat{a}_j^\dagger \hat{a}, \hat{\rho}\}, \tag{4.5}$$

and similarly for the cooling dissipator $\mathcal{D}[\hat{a}]\hat{\rho}$. Heating and cooling have rates $\gamma_{+,j}$ and $\gamma_{-,j}$, respectively, and describe energy transfer from the environment to the vibrations (heating) or vice versa (cooling).

The dissipators are engineered in the simulator by injecting a noisy electric field at the ion's location [224]. The electric field noise results in cooling and heating dissipators with approximately equal rates, $\gamma_j = \gamma_{+,j} = \gamma_{-,j}$, corresponding to a thermal bath with infinite temperature [150, 223]. In the molecule, this corresponds to a scaled dissipation rate $\Gamma_j = F^{-1}\gamma_j$. A noisy voltage signal, generated using an arbitrary waveform generator, is capacitively coupled onto a radial compensation electrode located 4.8 mm from the ion's position. The signal contains two frequency components oscillating near the vibrational mode frequencies, ω_x and ω_y. The rates γ_1 and γ_2 are programmed by varying the corresponding signal amplitudes. The

decay rates are calibrated using the trapped ion through a standard sideband thermometry experiment [152, 191].

The experiment correctly simulates the open-system dynamics at varying dissipation rates (Fig. 4.3f), showing the suitability of MQB simulation for the particularly challenging task of modelling ultrafast dynamics in open molecular systems. As expected, stronger dissipation leads to a faster loss of coherent features. With dissipation, the electronic population decays at long times to 0.5, consistent with a Boltzmann distribution at high temperature, where the populations of the two electronic states obey $n_1/n_0 = \exp(-\Delta E/k_{\mathrm{B}}T) = 1$. This equilibration occurs faster with stronger dissipation.

4.4 Discussion

In summary, we performed quantum simulations of non-adiabatic chemical dynamics of three molecules. We simulated the evolution of their vibrational wavepackets through conical intersections, obtaining distinct dynamics linked to the characteristics of their potential energy surfaces. We also simulated open-system dynamics of pyrazine coupled to a thermal bath using the same trapped-ion system.

Our experiment demonstrates three advantages of MQB simulations: programmability, resource efficiency, and the ability to simulate open systems.

MQB simulators are programmable, allowing us to simulate the dynamics of very different molecules simply by adjusting experimental parameters to match the different VC Hamiltonian in the same experimental apparatus.This programming is carried out through software-updated experimental parameters, without the need for hardware modification. Different features of photochemical processes were captured by the same MQB simulator: dynamics between different types of electronic states (ground or excited, singlet or doublet, degenerate or non-degenerate), vibrational modes and vibronic couplings with different symmetries, conical intersections with different topography (symmetric, peaked, and sloped), and a wide range of vibrational frequencies, vibronic couplings and wave-packet displacements.

MQB simulators require orders of magnitude lower quantum-hardware resourcing compared to qubit-only quantum simulations [11, 61]. We used a single trapped ion and a single laser pulse to simulate the ultrafast molecular dynamics of LVC models with two electronic states and two vibrational modes. The comparable quantum memory requirements can be estimated from the dimension of the necessary Hilbert space. Our simulations can be reproduced using 32 Fock states per mode, meaning that a comparable qubit-based simulation would need 11 qubits: $\lceil \log_2 32 \rceil = 5$ qubits for each of the two modes and an additional qubit for the electronic states. The CNOT gate requirements can be estimated using the resource-efficient Gray-code

qudit-to-qubit encoding [62] with accuracy chosen to reproduce the mean-squared error of our MQB simulation (which is 0.0034, averaged over the duration of our simulation). Doing so with a first-order Suzuki-Trotter decomposition needs 1000 errorless CNOT gates for each of 300 Trotter steps. Therefore, a comparable qubit-based simulation could be achieved with 3×10^5 CNOT gates. A realistic quantum computer with noisy gates or quantum error correction would require even more qubits and gates. A resource estimation for an MQB simulation of lattice gauge fields found a similar reduction of over five orders of magnitude of quantum resources [212].

We also demonstrate the ability of MQB simulators to simulate open-system dynamics by injecting controllable noise without using additional quantum resources. Comparable qubit-only simulations would have required additional ancilla resources to simulate the environment. On the MQB simulator, by contrast, the classically more difficult open-system problem is an easier task because some of the native noise can be used in the simulation, allowing for longer simulations with greater accuracy [214].

Extending MQB simulation beyond proof-of-principle experiments will enable increasingly challenging dynamics simulations. We envision opportunities for improvement in three areas: scale, non-linearities, and open quantum systems.

Scaling the experimental system from 1 to N trapped ions could enable the control of $3N$ motional modes [11]. The chief challenge to doing so is retaining the high quality of motional control over the additional modes, a matter complicated by spectral crowding and reduced interaction strengths [88]. These challenges could be mitigated using the same strategies developed for trapped-ion quantum computers using long ion chains, including advanced quantum-control methods and improved optical setups [225, 226].

MQB simulators could also be extended to implement higher-order vibronic-coupling models [11] or anharmonic potential energy surfaces. With the addition of beam-splitter interactions, the coherent laser-driven interactions demonstrated here are sufficient for universal control of MQB systems [227, 228], meaning that they can be composed into pulse sequences using quantum-control methods to engineer non-linear couplings or anharmonic potentials. However, full scope of this engineering remains an open question, because a fully general decomposition may scale unfavourably for high-dimensional, strongly coupled anharmonic potentials.

Finally, MQB simulations could be extended to include other types of dissipation for more comprehensive and fully programmable open-system quantum dynamics [214]. The most significant sources of noise in quantum-simulation experiments could be used as a resource to simulate the common forms of molecular decoherence and dissipation, thus significantly extending the useful lifetime of the simulation [214]. Fully exploiting all available sources of noise would be a powerful simulation technique because of the difficulty of open-system

chemical-dynamics simulations on classical computers.

Combining these three types of improvements in future experiments would allow addressing one of the great challenges of computational chemistry: simulation of the ultrafast dynamics of large, complicated molecules in the condensed phase. In doing so, MQB simulators could outperform other quantum simulation approaches: we estimate that an MQB simulator with 20–30 trapped ions could perform quantum-chemical-dynamics simulations that are classically intractable.

Our approach also opens up possibilities for hybrid simulation approaches that exploit complementary advantages of different types of hardware. For example, while an MQB simulator could carry out the dynamics, the electronic-structure calculations necessary to parametrise the VC Hamiltonians could be carried out on a classical computer or a digital quantum computer equipped with electronic-structure software.

Chapter 5: Using bosons to improve resource efficiency of quantum simulation of vibronic molecular dynamics

This chapter is a reformatted version of the publication:
Henry L. Nourse, Vanessa C. Olaya-Agudelo and Ivan Kassal, "Using bosons to improve resource efficiency of quantum simulation of vibronic molecular dynamics", *arXiv* 2512.20828 (2025).

Abstract

Simulating chemical dynamics is computationally challenging, especially for nonadiabatic dynamics, where numerically exact classical simulations scale exponentially with system size, becoming intractable for even small molecules. On quantum computers, chemical dynamics can be simulated efficiently using either universal, qubit-only devices or specialized mixed-qudit-boson (MQB) simulators, which natively host electronic and vibrational degrees of freedom. Here, we compare the quantum resources required for a qubit-only approach to achieve the same accuracy as an MQB device at simulating nonadiabatic molecular dynamics. We find that MQB simulations require orders-of-magnitude fewer quantum operations than qubit-only simulations, with a one-gate MQB circuit requiring a qubit-equivalent circuit volume of over 400,000 when simulating an isolated molecule, which increases to over ten million when environmental effects are included. These estimates assume perfect qubits and gates, and would increase by additional orders of magnitude if error correction were used for fault tolerance. When errors are small, the advantage of MQB simulators becomes even larger as system size increases. Our results highlight the enormous resource advantages of representing non-qubit chemical degrees of freedom natively, rather than encoding them into qubits.

5.1 Introduction

Chemical dynamics is fundamental to understanding the mechanisms of molecular transformations. Studying dynamics is particularly important for excited-state processes, where non-equilibrium quantum effects can steer reactions in potentially unexpected ways. Transitions

between excited states can lead to nonadiabatic quantum dynamics, which is particularly challenging to understand because it involves simultaneous changes in both electronic and nuclear degrees of freedom, leading to the breakdown of the Born-Oppenheimer approximation that underpins most chemical intuition. Nevertheless, nonadiabatic dynamics is ubiquitous, playing critical roles in processes such as photosynthesis [229], atmospheric chemistry [230], and solar energy conversion [231].

Accurately simulating nonadiabatic dynamics is challenging, even for small molecules, because the computational cost grows exponentially with system size for numerically exact, fully quantum algorithms. The cost arises from the need to accurately treat multiple coupled potential-energy surfaces [2, 3, 204]. Therefore, accurate state-of-the-art simulations are limited to chemical systems with a few tens of nuclear degrees of freedom [40, 232–234], and the situation is even more severe in the condensed phase, where one must model the influence of a large environment through open-system dynamics [206, 207, 232, 233, 235].

Quantum computers offer efficient simulation alternatives. Qubit-only simulators have universal applicability, since any quantum system can be simulated efficiently on a quantum computer [8, 60]. However, applying them to molecular dynamics involves discretizing continuous variables into qubits [61–66], which introduces substantial overhead in both the number of qubits and the circuit size. Nevertheless, qubit-only platforms carry the long-term prospect of fault-tolerant implementation because error-corrected qubits can execute deep circuits with controlled accuracy.

By contrast, mixed-qudit-boson (MQB) simulators naturally describe vibronic dynamics by mapping electronic states to qudits and nuclear motion to bosonic modes, such as the vibrations of trapped ions [11]. They have performed analog simulations of nonadiabatic dynamics in a range of chemical systems [105–107, 236], including dissipative processes of molecules interacting with an environment [82, 83, 236], which would incur significant overhead in qubit-only simulators [162–165, 237–242]. MQB devices promise to simulate nonadiabatic dynamics with high resource efficiency, with the potential of scaling to classically intractable systems with near-term technology. However, because they lack error correction they are susceptible to noise and the accumulation of errors.

Comparing the computational cost of MQB simulators and qubit-only computers is challenging because the two paradigms differ in how they represent quantum states, handle continuous variables, and scale with system size. They also have different sources of error, with MQB simulators suffering uncorrectable noise and qubit-only algorithms having greater algorithmic overhead and approximation error when bosonic degrees of freedom are discretized into qubits. Previous analyses of MQB simulation, primarily in lattice-gauge-theory and fermion-boson settings, have shown that access to native bosonic operations can reduce the number of quantum operations

because compiling them onto qubit-only devices introduces long gate sequences [243–246]. However, these approaches do not resolve the key issue for MQB simulators, i.e., determining when the accumulated hardware noise remains low enough that their resource advantage over qubit-only implementations survives. Answering this question requires a fair comparison of MQB and qubit-only approaches carrying out simulations with equal accuracy.

Here, we develop a systematic framework for comparing quantum resource costs between the two quantum-simulation approaches in the context of molecular dynamics. We quantify the quantum resources required in both approaches for simulating chemical dynamics to the same error. To ensure fairness, the comparison is made using the most resource-efficient method for each simulator, yielding conservative benchmarks. Using pyrazine as a case study, we find that MQB simulation requires dramatically fewer resources than qubit-only simulations to achieve the same error and that this advantage increases with system size, as long as errors are small. This is the case both for isolated molecules and, even more so, for molecules interacting with an environment.

5.2 Comparing quantum resources

Our approach to comparing quantum resource requirements on different types of simulators is as follows: (1) determining the resources to be counted for each simulator, (2) determining the error sources in both, and (3) counting the resources required for each simulator to achieve the same error in the desired observable.

The resource cost for quantum simulation has two broad components: computational memory and computational time. Memory is the number of information-carrying degrees of freedom (qubits, qudits, or bosonic modes) required to encode the relevant dynamics. It depends on the size of the molecular system, how it is mapped onto the simulator, and any memory overhead of the simulation algorithm. Time is the number of quantum operations (gates) that must be performed to evolve an initial state into the final state. This cost depends on the size of the system, the simulation algorithm, and the desired error in the final state.

To compare resource efficiency between quantum simulators, we employ a quantum volume metric that unifies memory and time costs [247–250]. We define the volume as the product of the memory and the time costs above. To compare resource efficiencies, for a given MQB volume (MQBV), we define the qubit-equivalent circuit volume (QECV) as the volume required for a qubit-only device to reproduce the same simulation task with the same error. The relative resource savings achieved by the MQB approach are then quantified by the advantage

$$A = \frac{\mathrm{QECV}}{\mathrm{MQBV}}. \tag{5.1}$$

To ensure a comparison of comparable simulation outcomes in the two approaches, simulation costs must be compared at fixed accuracy. The accuracy can be measured in a variety of ways [5], and the choice can affect the relative cost of the two simulations. In examples below, we track the error in the fidelity of the final state and in a chemically relevant observable, but our approach can be applied to any error metric.

There are two broad classes of errors in both MQB and qubit-only simulation. The first are experimental errors, being inaccuracies in gate execution and decoherence induced by the environment. The second are algorithmic errors, caused by mathematical approximations in the simulation algorithms. In principle, both would be accounted for in both types of simulations.

However, to simplify the discussion and highlight the key differences between MQB and qubit-only algorithms, we assume that the only source of error in MQB simulation is experimental error and in qubit-only simulation algorithmic error. The motivation for this distinction is that MQB simulation lacks error correction, so it accumulates error from experimental inaccuracies. Over time, this error will exceed any controllable algorithmic errors. In contrast, qubit-only simulations can, in principle, use error-correcting codes, in which multiple physical qubits encode higher-level logical qubits that suffer lower error rates [68, 251–254]. Gates on logical qubits then need to be decomposed into operations on the physical qubits, which incurs resource overheads. Therefore, the conservative approach to comparing the two errors is to compare the experimental error of MQB simulation with qubit-only algorithmic error. This implies that our qubit-only estimates are for perfect qubits and gates, free of experimental error. If the low experimental error is achieved through error correction, that overhead would increase the qubit-only resources.

5.3 Vibronic molecular dynamics

Vibronic molecular dynamics can be described by vibronic coupling (VC) Hamiltonians, which account for the coupling between electronic and vibrational degrees of freedom. VC Hamiltonians are Taylor expansions of the form [2, 3] (we set $\hbar = 1$ throughout)

$$H_{\mathrm{VC}} = \frac{1}{2}\sum_{j=1}^{M} \omega_j \left(P_j^2 + Q_j^2\right) + \sum_{n,m=1}^{D} W_{n,m} \left|n\right\rangle \left\langle m\right|, \tag{5.2}$$

$$W_{n,m} = c_0^{(n,m)} + \sum_j c_j^{(n,m)} Q_j + \sum_{j,k} c_{j,k}^{(n,m)} Q_j Q_k + \ldots, \tag{5.3}$$

where $|n\rangle$ is the nth diabatic electronic state; P_j and Q_j are the dimensionless momentum and position of the jth vibrational mode with frequency ω_j; D is the number of electronic states; M is the number of vibrational modes; and $c_0^{(n,m)}$, $c_j^{(n,m)}$, and $c_{j,k}^{(n,m)}$ are the expansion coefficients

of the molecular potential energy about the reference nuclear geometry (usually the minimum of the ground electronic surface).

Information about the system's dynamics is obtained by measuring observables, such as electronic-state populations, vibrational distributions, and spectroscopic correlation functions [255]. To determine these quantities for an isolated molecule, the initial molecular state ρ_0 is propagated in time under the unitary operator

$$U(t) = \exp(-iH_{\mathrm{VC}}t), \tag{5.4}$$

to the final state $\rho(t) = U(t)\rho_0 U^\dagger(t)$, on which any observable can be measured. For concreteness, we focus on diabatic population dynamics

$$P_n(t) = \mathrm{Tr}(\rho(t)\,|n\rangle\,\langle n|), \tag{5.5}$$

which are central to processes such as photoisomerization, exciton transfer, and internal conversion.

Molecular dynamics rarely occurs in isolation, instead taking place under continuous interaction with an environment. Even weak system-environment couplings can substantially modify dynamics, leading to phenomena such as decoherence, nonadiabatic transitions, and energy and charge transfer [17]. Many theoretical approaches have been developed to model these effects, but we restrict ourselves to Markovian dissipation described by the Lindblad master equation [17],

$$\frac{\partial\rho}{\partial t} = -i[H_{\mathrm{VC}},\rho] + \sum_{i=1}^{J}\gamma_i\mathcal{D}\left[V_i\right]\rho, \tag{5.6}$$

where γ_i is the rate at which the dissipator $\mathcal{D}\left[V_i\right]$ acts on the density matrix as

$$\mathcal{D}\left[V_i\right]\rho = V_i\rho V_i^\dagger - \tfrac{1}{2}\{V_i^\dagger V_i,\rho\}. \tag{5.7}$$

In chemical systems, the Lindblad equation usually arises from the assumption of weak and Markovian system-environment coupling, together with the secular approximation [17]. In that limit, the dominant dissipative processes are population transfers and dephasing, for both electronic and vibrational degrees of freedom. In particular, they are: radiative electronic relaxation described by $\mathcal{D}[|n\rangle\,\langle m|]$; vibrational heating and cooling in mode j, respectively described by $\mathcal{D}[a_j^\dagger]$ and $\mathcal{D}[a_j]$, where the annihilation operator for mode j is $a_j = (Q_j + iP_j)/\sqrt{2}$; electronic pure dephasing described by $\mathcal{D}[|n\rangle\,\langle n|]$; and vibrational pure dephasing in mode j described by $\mathcal{D}[a_j^\dagger a_j]$.

5.4 MQB simulation

MQB simulators [11] use both qudit and bosonic degrees of freedom, which can be implemented on a range of hardware, including ion traps [82, 83, 89, 105–107, 213, 256], circuit quantum

electrodynamics [84, 170, 257–260], and neutral atoms [261–264]. MQB devices natively encode the molecular degrees of freedom in H_{VC}, with qudits representing the electronic states and bosons the vibrational modes. Hence, H_{VC} can be directly mapped onto an MQB simulator, with $H_{\mathrm{MQB}} = FH_{\mathrm{VC}}$, where F is a scaling factor that accounts for differences in energy scales. An MQB simulation consists of preparing the simulator in an initial state, allowing it to evolve under H_{MQB} for a desired time, and measuring the observable of interest.

An MQB simulator can implement H_{VC} using the Hamiltonian [11]

$$\begin{aligned} H_{\mathrm{MQB}} = &\frac{1}{2}\sum_{j=1}^{M}\delta_j a_j^\dagger a_j + \sum_{n=1}^{D}\chi_n \left|n\right\rangle\left\langle n\right| + \sum_{n\neq m}\Omega_{n,m}\left|n\right\rangle\left\langle m\right| \\ &+ \sum_{n}\sum_{j}\Theta'_{n,j}(a_j^\dagger + a_j)\left|n\right\rangle\left\langle n\right| + \sum_{n,m}\sum_{j}\Omega'_{n,m,j}(a_j^\dagger + a_j)\left|n\right\rangle\left\langle m\right| + \ldots, \end{aligned} \tag{5.8}$$

where, with some abuse of notation, we use a_j to also denote the annihilation operator of the jth bosonic mode and $|n\rangle$ is a qudit state. All parameters can be programmed to reproduce relevant VC parameters and simulate a molecule of interest [11]. For example, for an ion-trap simulator, the parameters are programmed by adjusting the appropriate laser quantities [11]: δ_j arises from a laser's detuning from resonance with mode j, χ_n is a time-independent AC Stark shift, $\Omega_{n,m}$ can be controlled by changing the laser intensity or its detuning from an auxiliary electronic transition, $\Theta'_{n,j}$ corresponds to a time-dependent AC Stark shift from a pair of non-copropagating lasers, and $\Omega'_{n,m,j}$ is proportional to the Rabi frequency of a Mølmer-Sørensen interaction.

MQB simulators are resource efficient for vibrational molecular dynamics in both memory and time. The memory cost comes from two types of degrees of freedom: the number of qudits is always one and the number of bosons equals the number of vibrational modes in H_{VC}. Hence, the memory cost scales linearly with the number of molecular vibrational modes [11]. Depending on the underlying hardware, auxiliary qudit(s) and boson(s) might be used to implement certain gates [228, 260]. The time cost comes from single-qudit rotations, boson operations, and qudit-boson entangling operations, such as bosonic conditional displacements. Many of these operations can be combined into compound control pulses, which we count as one gate. Not all terms in H_{VC} are found in all types of MQB hardware, but they can be synthesized [11, 227, 228, 265–268] from native gates, which incurs an approximation error.

Extending the MQB approach to simulate molecules in an environment has the same resource cost as MQB simulation of unitary dynamics, but can be more accurate because environmental noise can be used as a resource [11, 214, 236]. Our goal is to simulate molecular dynamics under the master equation eq. (5.6), which MQB simulators can implement naturally [11, 214, 236] using two sources of dissipation: the intrinsic dissipation of the simulator itself and injected controllable dissipation, which can be engineered.

Native dissipation in the simulator can be classified as either *usable* or *unusable* [214],

depending on whether it can be harnessed to simulate dissipative molecular dynamics. For molecules interacting with an environment as described by eq. (5.6), usable dissipation is the Markovian simulator noise characterized by Lindblad dissipators $\mathcal{D}[V_i]$ and occurring at a native rate γ_i^{nat}, which can be measured in preliminary experiments. The unusable dissipation describes simulator dissipation that does not correspond to molecular dissipation processes.

As in simulations of isolated molecules, molecular dissipation rates are scaled to the MQB device as $\gamma_i^{\text{MQB}} = F\gamma_i$. However, when native dissipation is insufficient to reproduce the desired molecular dissipation, additional controllable dissipation of the same type $\mathcal{D}[V_i]$ can be injected, with rate γ_i^{inj}. The total rate is then

$$\gamma_i^{\text{MQB}} = \gamma_i^{\text{nat}} + \gamma_i^{\text{inj}} = F\gamma_i. \tag{5.9}$$

There are protocols to implement molecular dissipative processes using controllable noise injection. For example, in trapped-ion architectures [214, 236], radiative electronic relaxation, $\mathcal{D}[|n\rangle\langle m|]$, can be engineered using optical pumping to artificially shorten the lifetime of an excited state. Vibrational heating, $\mathcal{D}[a_j^\dagger]$, and cooling, $\mathcal{D}[a_j]$, can be implemented via resolved-sideband laser interactions applied to an ancillary ion that shares vibrations with the MQB simulator ions. Electronic, $\mathcal{D}[|n\rangle\langle n|]$, and vibrational, $\mathcal{D}[a_j^\dagger a_j]$, pure dephasing can be injected using stochastic fluctuations of the energies of the electronic and vibrational states.

There are several ways to choose the scaling factor F, depending on the dissipators involved and the fraction of injected noise included in the simulation [214]. Here, we only include one type of usable dissipation in the simulation, with rate γ_i^{MQB}. To maximize the simulation duration, we choose $F = \gamma_i^{\text{nat}}/\gamma_i$ so that this native dissipation is fully used, thereby eliminating the need for injected dissipation, $\gamma_i^{\text{inj}} = 0$ [214]. To distinguish the native dissipation used as a resource from unwanted dissipation that propagates into experimental errors, we denote the latter by γ_i^{err}.

5.5 Qubit-only simulation

Qubit-only quantum simulators encode both the electronic states and the vibrational modes of H_{VC} into qubits. All encodings of the vibrational modes are approximate because they represent an infinite-dimensional harmonic-oscillator Hilbert space in a finite number of qubits; however, the corresponding error can be systematically reduced at the cost of more quantum resources.

Different encodings—e.g., unary, binary, and Gray, whether in real space or Fock space—give different qubit and gate costs, sometimes offering tradeoffs between the two [62]. Binary and Gray encodings minimize the number of qubits but typically require more gates, while unary uses more qubits to reduce gate counts. Real-space representations give simple position operators at

the cost of complicated kinetic terms, whereas Fock-space representations can be more efficient for small oscillator displacements, where only low Fock states are occupied.

The memory cost of our qubit-only simulations are the numbers of qubits needed to encode the electronic and vibrational modes of H_{VC}. We use a Fock-space representation with the Gray encoding because it uses the fewest qubits and is more resource efficient than binary for position operators Q_j [62]. We assign a register of qubits to the electronic states (labeled x_0) and a register to each vibrational mode $(x_1, \ldots, x_M)$, which have been truncated to a d_j-level Fock space. The electronic states require $s_0 = \lceil \log_2 D \rceil$ qubits and each vibrational mode $s_j = \lceil \log_2 d_j \rceil$ qubits.

With that mapping, H_{VC} can be mapped onto qubits by decomposing each of its terms into a sum of Pauli strings. On a single qubit, the Pauli operators $\{I, \sigma_x, \sigma_y, \sigma_z\}$ form a basis for linear operators, and on s_j qubits, the basis is formed by the 4^{s_j} tensor products of these. Hence, any operator A_i acting on register i can be Gray-encoded as the Pauli sum [62]

$$\mathcal{G}[A_i] = \sum_{k=1}^{4^{s_i}} \alpha_{i,k} \mathcal{P}_{i,k}, \tag{5.10}$$

where the Pauli string $\mathcal{P}_{i,k} = \bigotimes_{\ell \in x_i} \sigma_{k,\ell}^{(i)}$ is a product of Pauli operators $\sigma_{k,\ell}^{(i)}$ acting on qubit ℓ of register x_i, and $\alpha_{i,k} = \mathrm{Tr}(P_{i,k} A_i)/2^{s_i}$. In practice, $\mathcal{G}[A_i]$ can have drastically fewer Pauli strings than 4^{s_i} if it is, e.g., diagonal, local, or sparse.

To map H_{VC} onto qubits, $\mathcal{G}[\cdot]$ is applied to each term in H_{VC}, except that we combine P_j^2 and Q_j^2 into $n_j = (P_j^2 + Q_j^2)/2$ because diagonal operators require fewer gates. For each term, we decompose the operators acting on different degrees of freedom separately and multiply the results together, e.g., $\mathcal{G}[|n\rangle \langle m| Q_i^r Q_j^v] = \mathcal{G}[|n\rangle \langle m|] \mathcal{G}[Q_i^r] \mathcal{G}[Q_j^v]$. After grouping equivalent Pauli strings and removing those proportional to the identity (which do not affect the dynamics), H_{VC} becomes

$$H_{\mathrm{qubits}} = \sum_{k=1}^{L} \alpha_k \mathcal{P}_k. \tag{5.11}$$

where $\mathcal{P}_k$ is a Pauli string with coefficient α_k and L is the total number of Pauli strings.

5.5.1 Isolated molecule

To simulate the unitary dynamics under H_{qubits}, various quantum-simulation algorithms could be used, including Trotter-based algorithms [8, 61] or qubitization-based approaches [269–271]. These exhibit different time and space costs, as well as different asymptotic scalings, and the choice of the best algorithm depends on the system under study and the available resources.

Here, we adopt Trotter-based algorithms because they tend to have lower overheads for small systems compared to the asymptotically faster qubitization-based approaches [272–274].

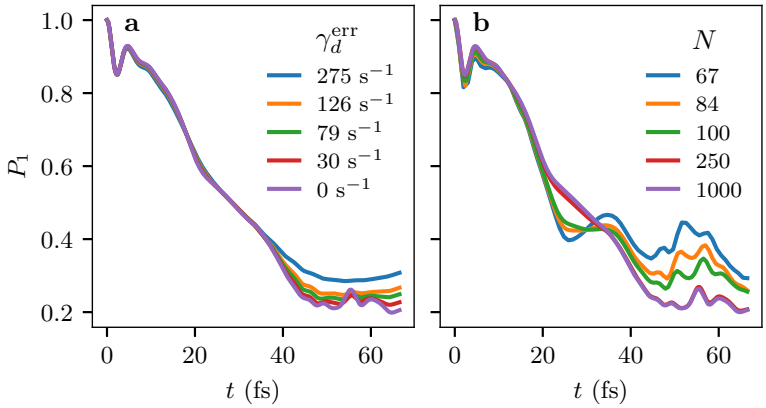

Figure 5.1: Simulated population dynamics of the pyrazine bright state $\pi\pi^*$ subject to different sources of error, using an LVC model with two electronic states and two vibrational modes. **(a)** Dynamics in an MQB simulator, subject to pure vibrational dephasing with rate γ_d^{err} on both vibrational modes. **(b)** Dynamics on a qubit-only simulator, subject to first-order Trotter error due to discretization to N steps.

In Trotterization, the total simulation time T is discretized into N steps of length $\Delta t = T/N$. The unitary evolution up to time T is then $U(T) \approx (U^{(p)}(\Delta t))^N$, where $U^{(p)}(\Delta t)$ is the pth order Trotter approximation for each time step. At first order,

$$U^{(1)}(\Delta t) = \prod_{k=1}^{L} U_k(\Delta t), \tag{5.12}$$

where $U_k(\Delta t) = \exp(-i\,\alpha_k \mathcal{P}_k\,\Delta t)$. Higher-order Suzuki-Trotter decompositions [37, 38] have better asymptotic scaling but can require more quantum resources at smaller errors [272, 275, 276]. To fairly compare with MQB simulation, the Trotter order that has the lowest resource count should be used. We use first-order because it is simple to analyze and performs comparably to second-order at errors achieved by MQB simulators (see section S1.1). Another Trotter-based quantum algorithm for VC models [66] achieves comparable costs to our method using a different bosonic representation and quantum circuit.

With this choice of algorithm, we can estimate the required qubit-only time cost. Each $U_k(\Delta t)$ can be decomposed into a CNOT ladder [5, 277–279] containing one $R_z(2\alpha_k \Delta t)$ gate and $2(p_k - 1)$ CNOT gates, where p_k is the number of non-identity single-qubit Pauli gates in the Pauli string $\mathcal{P}_k$ [62]. Therefore, in a single Trotter step, the total number of R_z gates is L and the total number of CNOT gates is $\sum_{k=1}^{L} 2(p_k - 1)$. However, it is thought that the number of CNOT gates can be reduced through optimization by up to a factor of 3 [62]; therefore, to be conservative in our comparison, we report the CNOT cost as $\sum_{k=1}^{L} 2(p_k - 1)/3$. For simulation to the final time T, the total number of gates is N times the number of gates for a single step.

5.5.2 Molecule in environment

Qubit-only devices can also simulate open quantum systems, often by using additional qubits to simulate the environment [162–165, 237–242]. Here, we use an algorithm that unravels the Lindblad dynamics into a stochastic differential equation (SDE) that can be solved using unitary dynamics in an enlarged Hilbert space [241]. It has low overhead and allows the use of the same Trotter-based simulation approach we use for an isolated molecule. Specifically, we use the dilated Hamiltonian

$$H_{\text{dil}} = \begin{pmatrix} \sqrt{\Delta t}\, H_{\text{qubits}} & V_1 & \dots & V_J \\ V_1^\dagger & 0 & \dots & 0 \\ \vdots & \vdots & \ddots & \vdots \\ V_J^\dagger & 0 & \dots & 0 \end{pmatrix}, \tag{5.13}$$

where $V_1, \dots, V_J$ are the jump operators from eq. (5.6). H_{dil} is a block matrix whose entries are $\sqrt{\Delta t}\, H_{\text{qubits}}$ and V_i, and a register of $\lceil \log_2(J+1) \rceil$ ancilla qubits (labeled b) is introduced for a binary encoding of the block index.

A discrete-time approximation to the evolution of ρ under eq. (5.6) is [241]

$$\rho_{m+1} \approx \text{Tr}_b \left(e^{-i\sqrt{\Delta t}\, H_{\text{dil}}} \, |0_b\rangle \langle 0_b| \otimes \rho_m \, e^{i\sqrt{\Delta t}\, H_{\text{dil}}} \right), \tag{5.14}$$

where ρ_m is the reduced density matrix of the molecule at time $t = m\Delta t$ and $|0_b\rangle$ are the ancilla qubits that are measured, discarded, and reset after each time step. The required time evolution generated by H_{dil} can be achieved with the same method used to time-evolve H_{qubits}. Hence, we time evolve H_{dil} using a first-order Trotter algorithm, as in eq. (5.12).

Counting resources for the time evolution under H_{dil} is similar to counting resources for evolution under H_{qubits}. The memory cost is the same as for the simulation of the isolated molecule, plus an additional $\lceil \log_2(J+1) \rceil$ ancilla qubits for the bath register. The time cost is counted in the same way as for eq. (5.12), except that the unitary dynamics is now governed by H_{dil}, so the number of R_z and CNOT gates will be higher. This increase occurs because of the increased dimension of H_{dil} (which requires more Pauli strings and thus more R_z gates) and because the CNOT ladder includes additional entangling operations with the bath register.

In our simulations of H_{qubits} and H_{dil}, we assume perfect qubits and gates. Hence, there are two classes of errors in our qubit-only simulations: the error from truncating the vibrational modes to d_j-level Fock spaces and the Trotter error in describing the dynamics under H_{qubits} or H_{dil}. Because we are interested in quantifying the necessary quantum resources due to algorithmic error, in our simulations we choose $d_j = 32$, which is large enough that the truncation error is negligible compared to the Trotter error. The algorithmic error can be systematically improved by increasing the Trotter number N, i.e., decreasing the time step Δt.

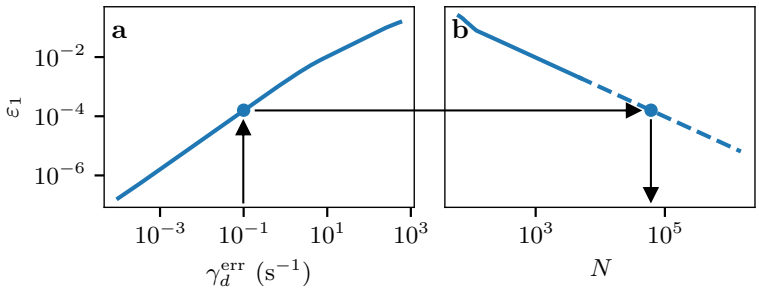

Figure 5.2: Matching errors between MQB and qubit-only simulations of isolated pyrazine. **(a)** MQB error of the excited-state population P_1 as a function of the vibrational pure-dephasing rate γ_d^{err}. **(b)** Same error for a qubit-only simulator, as a function of the Trotter number N. Arrows depict an example of error matching between MQB and qubit-only simulations: for $\gamma_d^{\mathrm{err}} = 0.1\,\mathrm{s}^{-1}$, the MQB simulation error of $\varepsilon_1 = 1.6 \times 10^{-4}$ is matched to the same qubit-only error, which occurs at $N = 61\,000$. Dashed line is extrapolation.

5.6 Example: Pyrazine

To demonstrate a comparison of MQB and qubit-only quantum resources, we apply our approach to pyrazine ($C_4N_2H_4$), a widely benchmarked system for nonadiabatic dynamics [220, 221, 280]. In pyrazine, photoexcitation from the ground state to the $\pi\pi^*$ bright state decays to the $n\pi^*$ dark state through internal conversion, mediated by vibrational degrees of freedom dominated by a ring-breathing mode and an out-of-plane hydrogen wag [220, 221]. This nonadiabatic dynamics can be described with a linear-vibronic-coupling (LVC) Hamiltonian with two electronic states linearly coupled to two vibrational modes. Denoting the $\pi\pi^*$ state as $|1\rangle$ and $n\pi^*$ as $|0\rangle$, the pyrazine LVC Hamiltonian is

$$H_{\mathrm{LVC}} = \tfrac{1}{2}\sum_{j=1}^{2}\omega_j(P_j^2 + Q_j^2) - \tfrac{1}{2}\Delta E\,\sigma_z + \kappa\sigma_z Q_1 + \lambda\sigma_x Q_2, \tag{5.15}$$

where $\omega_1/(2\pi) = 17.9\,\mathrm{THz}$, $\omega_2/(2\pi) = 28.5\,\mathrm{THz}$, $\Delta E/(2\pi) = 199\,\mathrm{THz}$, $\kappa/(2\pi) = -30.7\,\mathrm{THz}$, and $\lambda/(2\pi) = 63.3\,\mathrm{THz}$ [221]. The initial state ρ_0 is a Franck-Condon excitation from the ground state to the $\pi\pi^*$ state, corresponding to a displaced wavepacket with displacement parameter $\alpha = 0.210$ [221]. To simulate pyrazine in an environment, we consider the case where the molecule is subjected to vibrational pure dephasing, i.e., $V_j = n_j$ in eq. (5.6), with rate $\gamma_j = \gamma_d = 2.1 \times 10^{12}\,\mathrm{s}^{-1}$ for each vibrational mode j [181].

For MQB simulations, we model the simulator noise with a Lindblad master equation (eq. (5.6)). For isolated pyrazine simulated on ion-trap hardware, native dissipation is not used as a resource and the dominant error source is vibrational pure dephasing [105, 106, 214], which is modeled with Lindblad jump operators $V_j = n_j$ acting on each mode j with the same rate $\gamma_d^{\mathrm{nat}} = \gamma_d^{\mathrm{err}}$ (see fig. 5.1a). The native noise rates depend on the hardware, but typical ion-trap values are $\gamma_d^{\mathrm{nat}} \in [1, 10^2]\ \mathrm{s}^{-1}$ [94, 105, 106, 150, 177, 178, 214].

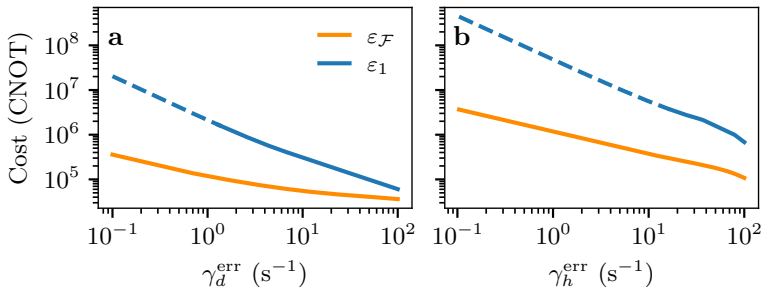

Figure 5.3: MQB simulation requires orders of magnitude fewer quantum resources compared to qubit-only simulation with the same error. Shown is the equivalent computational cost, in logical CNOT gates, on a qubit-only computer for simulating the vibronic dynamics of **(a)** isolated pyrazine and **(b)** pyrazine in an environment (with $\gamma_d = 2.1 \times 10^{12}\,\mathrm{s}^{-1}$). The equivalent cost is defined by matching the error ε_1 or infidelity $\varepsilon_{\mathcal{F}}$ on the MQB simulator, which arise from pure vibrational dephasing γ_d^{err} in **(a)** and vibrational heating γ_h^{err} in **(b)**. Typical ranges of these rates in trapped-ion simulators are $\gamma_d^{\mathrm{nat}} \in [1, 10^2]\ \mathrm{s}^{-1}$ and $\gamma_h^{\mathrm{nat}} \in [10^{-1}, 10^1]\ \mathrm{s}^{-1}$ [94, 105, 106, 150, 177, 178, 214]. Dashed lines are extrapolation.

When simulating pyrazine in an environment, the vibrational pure dephasing of the simulator becomes usable dissipation. Based on recent MQB hardware [105, 106, 236] we set $\gamma_d^{\mathrm{MQB}} = \gamma_d^{\mathrm{nat}} = 30\,\mathrm{s}^{-1}$, giving $F = \gamma_d^{\mathrm{nat}}/\gamma_d = 1.4 \times 10^{-11}$. Simulation errors are now due to the second-largest source of noise, which is not useful for describing our molecule-environment model. In ion-trap hardware, this is vibrational heating [105, 106, 214], $V_j = a_j^\dagger$, with all modes subject to the same rate $\gamma_h^{\mathrm{nat}} = \gamma_h^{\mathrm{err}}$, typically in the range $\gamma_h^{\mathrm{nat}} \in [10^{-1}, 10^1]\ \mathrm{s}^{-1}$ [94, 105, 106, 150, 177, 178, 214].

Figure 5.1 shows the effect of the simulation errors on the accuracy of the two simulation approaches in reproducing the population dynamics $P_1(t)$ of the $\pi\pi^*$ state of isolated pyrazine. In the MQB simulation (fig. 5.1a), decreasing the simulator noise γ_d^{err} decreases the error in $P_1(t)$, while in qubit-only simulation the error decreases with increasing Trotter number N. Section S1.2 provides the details of our numerical implementation.

We estimate the cost of MQB simulations on trapped-ion hardware based on previous vibronic simulations [105, 106, 236]. The memory cost is one qubit from a single ion to represent the two electronic states, as well as two bosons (two vibrations of the single ion) to encode the two molecular vibrational modes. The time cost is one gate because both the isolated and the in an environment simulations can be achieved with one gate, a single compound laser pulse [106].

For qubit-only simulations, we determine the resources necessary to match the error of MQB simulators. The memory cost to simulate isolated pyrazine is 11 qubits: one to encode the two electronic states and five to encode each vibrational mode with Fock-space cutoff $d = 32$, for which P_1 converges to within an absolute error of 10^{-6}. The time cost of each first-order Trotter step is 300 CNOT and 170 R_z gates. Our qubit-only simulations of pyrazine in an environment consider the same case as our MQB simulations, namely vibrational pure dephasing in each of the two modes with $\gamma_d = 2.1 \times 10^{12}\,\mathrm{s}^{-1}$. Including the $J = 2$ jump operators requires an additional $\lceil \log_2(J+1) \rceil = 2$ ancilla qubits to encode H_{dil}, giving a total memory cost of 13

qubits. The time cost per Trotter step is now 1800 CNOT and 700 R_z gates.

To compare quantum resources between MQB and qubit-only simulators, we consider two error metrics that provide complementary information about simulation accuracy. The maximum infidelity between the approximate state $\tilde{\rho}(t)$ and the exact state $\rho(t)$ is

$$\varepsilon_{\mathcal{F}} = \max_t \left(1 - \mathcal{F}(t)\right) = \max_t \left(1 - \left(\mathrm{Tr}\sqrt{\sqrt{\rho(t)}\,\tilde{\rho}(t)\sqrt{\rho(t)}}\,\right)^2\right), \tag{5.16}$$

and the maximum error in the $\pi\pi^*$ population is

$$\varepsilon_1 = \max_t \left|\tilde{P}_1(t) - P_1(t)\right|, \tag{5.17}$$

where $\tilde{P}_1(t)$ is the approximate and $P_1(t)$ the exact population. Infidelity is a global measure of how close the state remains to the exact one. By contrast, $P_1(t)$, like many chemical observables, probes local features of the state, making it less sensitive to simulation errors than the fidelity [281–283]. Evaluating both metrics therefore gives a more complete picture of how MQB and qubit-only simulations perform.

We match the errors between MQB and qubit-only simulators to compare their costs fairly. In particular, we compute the qubit-only gate cost, in CNOT and R_z gates, needed to achieve the same error as would be achieved with an MQB device with typical error rates. Specifically, given the γ_d^{err} rate of the MQB simulator, we determine the number of Trotter steps N needed for the qubit-only simulator to achieve the same accuracy, as illustrated in fig. 5.2. For pyrazine in an environment, we follow the same method, except that γ_h^{err} determines the MQB error. To match errors, we use cubic splines to interpolate between calculated values. To match low MQB simulation errors, we extrapolate the qubit-only results to larger Trotter numbers once numerical simulations become prohibitively expensive. The error of an observable is bounded by the operator-norm error for Trotter simulations, $\varepsilon_1 = O(t^2/N)$ [36, 272], meaning that $\log(\varepsilon_1) = -\log N + \text{constant}$ at fixed t. We perform numerical simulations up to an N large enough that ε_1 (and $\varepsilon_{\mathcal{F}}$) follow this expected scaling, beyond which we use it for extrapolation, as shown in fig. 5.2b.

Error-matching reveals the significant advantage of using bosons in the MQB approach, as shown in fig. 5.3. For both error metrics, the cost of the qubit-only simulation with equivalent error increases as the MQB simulator error decreases. This result holds for both simulations of the isolated pyrazine molecule and in an environment.

Table 5.1 highlights specific costs for MQB noise levels reflective of recent experiments [105, 106, 236]. For the isolated molecule, for qubit-only simulations to achieve the same infidelity as existing MQB devices requires at least 4×10^4 CNOT and 2×10^4 R_z gates. Because the memory requirements are larger as well, the single-pulse MQB simulation equates to a QECV of 4×10^5.

Table 5.1: Resource counts for simulating linear vibronic dynamics of pyrazine with two electronic states and two modes. MQB resources measure qudits and bosonic modes (memory) and sequential compound gates (time). Qubit-only resources measure qubits (memory) and CNOT and R_z gates (time). Volume is memory multiplied by time (CNOT), and advantage is the ratio of qubit-only and MQB volumes. Results are for MQB simulator noise representative of recent MQB hardware [105, 106]: $\gamma_d^{\text{err}} = 30\,\text{s}^{-1}$ for the isolated molecule and $\gamma_h^{\text{err}} = 2 \times 10^{-1}\,\text{s}^{-1}$ for the one in an environment.

	MQB	Qubit-only			
		Matched $\varepsilon_{\mathcal{F}}$		Matched ε_1	
		Isolated	Open	Isolated	Open
Memory	3	11	13	11	13
Time	1	4×10^4 CNOT 2×10^4 R_z	3×10^6 CNOT 1×10^6 R_z	1×10^5 CNOT 7×10^4 R_z	2×10^8 CNOT 8×10^7 R_z
Volume	3	4×10^5	3×10^7	1×10^6	2×10^9
MQB advantage		1×10^5	1×10^7	3×10^5	6×10^8

When environmental effects are included, the gap in quantum resources widens further by orders of magnitude. MQB simulations of a pyrazine molecule in an environment require far fewer resources than equally accurate qubit-only simulations. Specifically, we find that to match the infidelity of MQB simulations with one MQB gate requires 3×10^6 CNOT and 1×10^6 R_z gates, giving a QECV of 3×10^7. This improved MQB resource efficiency arises because bosonic degrees of freedom and their dissipators map naturally onto MQB simulators, while on qubit-only platforms these must be encoded into H_{dil} at significant cost.

The resource gap between MQB and qubit-only simulators is even larger for errors in the more chemically relevant population dynamics, $P_1(t)$. To match ε_1 in MQB simulations of isolated pyrazine, qubit-only simulations now require 1×10^5 CNOT and 7×10^4 R_z gates, with a QECV of 1×10^6. The resource gap between MQB and qubit-only simulations is enormous for pyrazine in an environment: 2×10^8 CNOT and 8×10^7 R_z gates, with a QECV of over 2×10^9. MQB simulators perform so well at calculating $P_1(t)$ primarily because dephasing in MQB devices damps coherences while preserving population transfer pathways, leading to small ε_1 even when global infidelity is modest. In contrast, Trotterization does worse because it induces coherent, history-dependent distortions (phase shifts and amplitude bias) that directly perturb population dynamics, as shown in fig. 5.1b. Therefore, for simulations of direct chemical relevance, such as populations, MQB devices can outperform qubit-only simulators by very large margins.

5.7 Scaling with system size

Understanding how the resource requirements of MQB and qubit-only simulators compare with increasing system size is essential for assessing their performance on larger, classically intractable systems. We expect the resource advantage of MQB simulators over qubit-only ones to increase for medium-sized molecular problems, and likely more so for chemically relevant open-system cases, before ultimately being limited at very large sizes by the increasing errors in MQB devices.

We extend our resource comparison to larger molecules by adding modes to the LVC model of pyrazine, where each additional mode contributes one quadratic term $\omega_2(P_j^2+Q_j^2)$ and one linear vibronic-coupling term $\lambda\sigma_x Q_j$. Because simulations beyond a few modes become prohibitively expensive on classical computers, we perform calculations at a smaller Fock-space truncation of $d=4$ for up to $M=5$ modes. MQB noise is modeled as a per-mode contribution, with each mode subject to the same dissipation rate—γ_d for isolated molecules and γ_h for molecules in an environment.

MQB simulation further improves its advantage over qubit-only simulation with increasing system size, as shown in fig. 5.4. Although MQB simulation error grows with the number of modes (see fig. 5.4a,c), the resources required for qubit-only simulation to match the MQB error also increase, so long as the MQB error remains small, as in our simulations (see fig. 5.4b,d). Qubit-only resource costs rise both in qubit count (each additional mode introduces 5 qubits) and in gate count (each mode contributes an additional sequence of CNOT ladders per Trotter step).

This advantage of MQB simulation at larger system sizes comes from the efficient encoding: the memory cost grows linearly as $1+M$ because each additional mode requires only one additional boson, while the full time evolution can still be implemented with a single compound laser pulse, amounting to one gate [11]. However, the error also grows with system size: as more modes are included, each one experiences environmental noise intrinsic to the MQB device. If all modes experience comparable dissipation rates (as we assume), the total error is expected to scale at least linearly with system size, as is typical in other analog devices [284, 285].

Qubit-only devices encounter a different bottleneck, the rapid growth of gate cost with the number of modes. Although the qubit-only memory cost scales linearly with the number of modes as well, the time cost of the Trotter simulation to reach error ε scales at least quadratically, as $O(M^{2+1/p}(\Lambda T)^{1+1/p}\varepsilon^{-1/p})$. This is because the gate cost grows linearly with M and the Trotter number scales as $N=O((M\Lambda T)^{1+1/p}\varepsilon^{-1/p})$. The latter is obtained from the commutator error for local Hamiltonians [272], where H_{qubits} is $(d+1)$-local because the qubit register encoding the electronic states overlaps in support with each bosonic qubit register

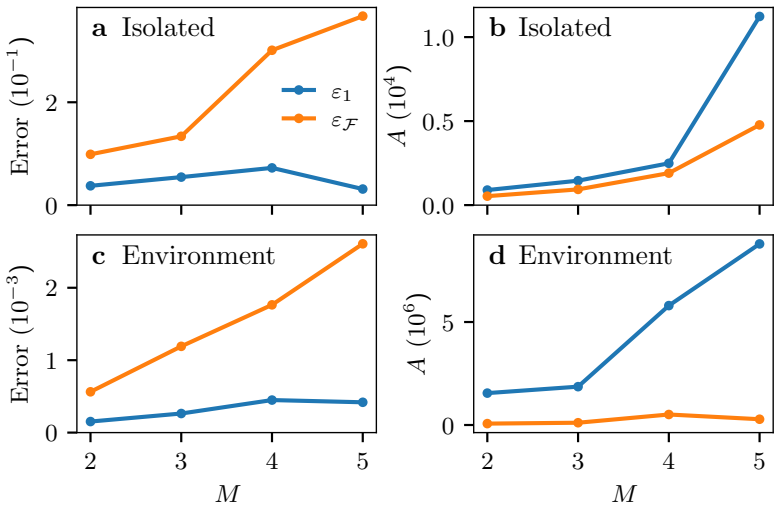

Figure 5.4: The advantage of MQB simulators over qubit-only simulators grows with system size, even as MQB errors increase. **(a,c)**: MQB errors increase with the number of modes M for both an isolated molecule and when in an environment (with $\gamma_d = 2.1 \times 10^{12}\,\mathrm{s}^{-1}$) because each mode experiences noise. Infidelity increases monotonically because it is a global error, whereas the population error is a local observable and can be non-monotonic. **(b,d)**: The advantage A—the ratio of qubit-only to MQB volume—increases with system size. Here, $\gamma_d^{\mathrm{err}} = 30\,\mathrm{s}^{-1}$ and $\gamma_h^{\mathrm{err}} = 0.2\,\mathrm{s}^{-1}$ for the isolated and in environment molecule, respectively.

through the linear-vibronic-coupling terms. For local Hamiltonians and pth order product formulas, achieving error ε requires $N = O(|||H_{\mathrm{qubits}}|||_1 ||H_{\mathrm{qubits}}||_1^{1/p} T^{1+1/p} \varepsilon^{-1/p})$ Trotter steps, where $|||\cdot|||_1$ denotes the induced 1-norm and $||\cdot||_1$ the 1-norm [272]. Since H_{LVC} has $\Theta(M)$ vibronic-coupling terms, $|||H_{\mathrm{qubits}}|||_1 = O(M\Lambda)$ and $||H_{\mathrm{qubits}}||_1 = O(M\Lambda)$, with $\Lambda = \max_k |\alpha_k|$.

For open systems, the resource advantage of MQB simulators is even greater as system size increases (see fig. 5.4d). Simulating more environmental interactions significantly raises resource costs in qubit-only devices; in particular, the gate count grows faster than for the isolated molecule because it scales with both the number of modes M and the number of jump operators J. In contrast, although noise in MQB simulators is extensive, the same is true for molecules coupled to an environment. If the dominant noise sources are harnessed as part of the simulation, only the residual unwanted noise contributes to the error, which then grows more slowly than in simulations of isolated molecules and may remain sufficiently small, or otherwise be mitigated, to achieve useful accuracy.

5.8 Discussion

We have shown that MQB simulators require orders-of-magnitude less resources compared to qubit-only ones, even for small molecules such as pyrazine. The advantage becomes even larger when environmental effects are included and as system size increases. This resource efficiency arises because MQB simulators can natively represent electronic states (as a qudit), molecular

vibrational modes (as bosons), and environmental effects (as Lindbladian dissipators).

Our resource counts are conservative, because all our algorithmic choices favor qubit-only efficiency. Most importantly, our qubit-only estimates only consider algorithmic error, i.e., they assume perfect, noiseless qubits and gates. In practice, incorporating fault tolerance would inflate both the qubit and gate counts by additional orders of magnitude [68, 252, 286]. Furthermore, our worst-case comparison is based on the infidelity $\varepsilon_{\mathcal{F}}$, which is particularly sensitive to MQB simulator noise; by contrast, errors in chemically relevant local observables, such as ε_1, would typically be significantly lower (see fig. 5.3). Finally, we applied a generous 1/3 reduction to CNOT counts to account for best-case circuit optimizations [62], further biasing our estimates downward. For larger systems, qubit-only simulation approaches based on higher-order product formulas [37, 38, 272] or qubitization [269–271] may offer improvements because they have better asymptotic scaling.

We expect the MQB advantage to persist for classically intractable system sizes. Under the analysis in section 5.7, the MQB resource advantage is expected to grow at least linearly with system size, since the resources required by qubit-only simulators scale at least quadratically, while errors in MQB devices increase approximately linearly. However, this growth cannot continue indefinitely. The analysis assumes small errors and therefore fails once the MQB error (whether $\varepsilon_{\mathcal{F}}$ or ε_1) becomes of order unity. No uncorrected simulator—quantum or classical—can simulate arbitrarily large systems for arbitrarily long times to an arbitrarily low error. However, the relevant question is whether practical, classically intractable problems can be solved in the foreseeable future given typical noise rates. We expect the answer to be yes because classical intractability arises in systems only slightly larger than those in our numerical simulations.

All results presented here are based on noise levels and capabilities representative of current MQB hardware. Further hardware improvements will extend the resource advantage to even larger molecular systems. Such improvements are likely to include improved experimental motional control and, in the longer term, bosonic quantum error suppression or correction [287, 288] to reduce residual noise.

Overall, our results support a clear design principle for quantum simulation of chemistry: represent non-qubit degrees of freedom natively whenever possible. For vibronic dynamics, this principle translates into orders-of-magnitude savings and a credible path to classically intractable regimes on near-term MQB devices, especially for open-system chemistry.

S1 Supplemental material

S1.1 Higher-order Trotter

We evaluate qubit-only resource requirements to simulate the LVC model of pyrazine using first-order Trotterization, as it has resource costs comparable to higher-order schemes while remaining simpler to analyze, as shown in fig. S1. Although higher-order Trotter formulas offer better asymptotic error scaling, their large constant prefactors can make each step more costly. This creates a tradeoff where higher orders become advantageous only at very small target errors.

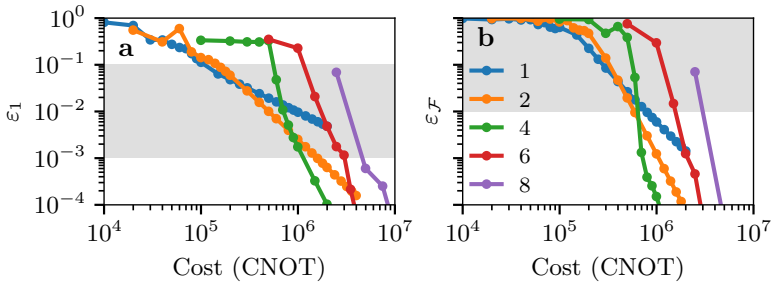

Figure S1: Resource requirements for first- and second-order Trotterizations are comparable in qubit-only simulations when targeting **(a)** population error and **(b)** infidelity for isolated pyrazine at error levels typically achieved by MQB simulators (shaded region). The legend labels the pth-order Suzuki-Trotter decomposition.

S1.2 Numerical implementation

We simulated the MQB dynamics using the `mesolve` function for open-system quantum dynamics in QuTiP [289]. Our qubit-only simulations were obtained from a Trotter algorithm also implemented using QuTiP. Equation (5.11) was obtained numerically by using Cirq [290] to find equivalent Pauli sums and removing terms with coefficients $|\alpha_k| < 10^{-10}$, which occur due to numerical rounding errors. To estimate errors of our simulations, we compared the simulation results to numerically exact simulations obtained using the `sesolve` and `mesolve` functions in QuTiP for an isolated and open molecule, respectively. In all of our `sesolve` and `mesolve` simulations, we set the relative and absolute convergence tolerances to 10^{-8} and 10^{-6}, respectively.

Chapter 6: Conclusion

This thesis has established the viability of MQB simulators as a practical near-term platform for the simulation of nonadiabatic chemical dynamics. As a result of the work reported here, MQB devices can efficiently simulate both isolated and open molecular dynamics, perform arbitrary measurements, harness noise as a resource to extend simulation times, and inject controllable dissipation without significant experimental overhead.

We showed that MQB devices can access phenomena of long-standing interest in chemical physics. By engineering a Jahn–Teller Hamiltonian in a trapped-ion simulator, we directly observed geometric-phase interference in a quantum system evolving around a conical intersection through full wavepacket reconstruction. This quantum effect had previously only been inferred indirectly in chemical reaction experiments, and its direct observation had remained elusive until now. This achievement demonstrates the power of MQB platforms to provide experimental insights into quantum effects underlying molecular processes.

We extended the MQB framework to simulate open-system dynamics, a crucial step towards modelling nonadiabatic processes in condensed-phase environments, a common setting for real chemical dynamics. Our approach harnesses the intrinsic noise of the simulator as a resource—allowing longer simulation times—and provides a clear experimental route to inject controllable dissipation with minimal overhead. Using the Lindblad formalism, this framework enables the inclusion of essential dissipative channels such as vibrational and electronic relaxation and dephasing, allowing MQB devices to capture coherence and dissipation that defines realistic molecular dynamics.

We then advanced from proof-of-principle experiments to programmable simulations, demonstrating that MQB devices can reproduce a range of nonadiabatic and photochemical processes across different molecular systems. To this end, we programmed a MQB platform to simulate and measure the ultrafast dynamics of three different molecules—allene, butatriene, and pyrazine—capturing both coherent and dissipative behaviour, the latter implemented through engineered dissipation. This demonstrates the versatility of MQB platforms in modelling diverse molecular systems.

Finally, we developed a systematic framework to quantify the quantum resources required for MQB simulations compared to qubit-only approaches. Our analysis revealed that MQB devices deliver dramatic efficiency gains, requiring at least five orders of magnitude fewer entangling operations for closed-system dynamics and over a million-fold improvement for open-system

simulations. These findings highlight the unique advantages of using bosonic degrees of freedom as natural simulators of vibrational dynamics.

Taken together, these contributions show that MQB simulators are experimentally feasible. They provide a versatile, programmable and efficient framework able to simulate coherent and dissipative dynamics of non-adiabatic chemical processes. MQB simulator can use their intrinsic noise as a resource to extend their simulation time. Similarly, controllable dissipation can be injected without adding significant experimental overhead compared to closed-system simulations. All these features offer experimentally accessible insights into complex quantum phenomena and deliver significant resource savings compared with alternative approaches. This thesis therefore positions MQB simulation as clear route toward addressing some of the most challenging problems in chemical dynamics, laying the groundwork for the next generation of quantum technologies in chemistry and materials science.

6.1 Outlook

A logical progression for MQB simulation is to move beyond proof-of-principle demonstrations and extend its scope to more complex and chemically relevant models. This includes, for example, incorporating anharmonic and non-linear couplings, simulating vibronic Hamiltonians with many degrees of freedom, and modelling open quantum systems in non-Markovian environments. Progress in these directions will enable the description of richer energy landscapes, capture collective vibrational effects in large molecules, and account for other system–environment interactions. Alongside hardware advances in MQB platforms, these developments, combined with strategies such as controlled noise engineering and bosonic error correction, will significantly expand the range of chemical processes accessible to MQB simulators in the near future.

A natural step forward is to extend MQB simulations to more complex Hamiltonians that go beyond the linear vibronic coupling model. This includes implementation of anharmonicities (e.g., Q^3 or Q^4) and non-linear couplings (e.g., $Q_1Q_2^2$ or $Q_1^2Q_2^2$). Such extensions are particularly relevant for describing chemical processes that involve richer energy landscapes than the harmonic approximation can provide, such as proton tunnelling in hydrogen-bonded systems [291, 292]. One promising route is to couple harmonic vibrational modes to anharmonic subsystems, such as qubits, thereby synthesising effective interactions that encode anharmonic terms and non-linear couplings in the previously harmonic mode. Developing these capabilities would significantly broaden the class of chemical problems accessible to MQB simulators, opening the way to quantitative studies of phenomena that remain beyond the reach of both current classical methods and standard harmonic models.

Similarly, the simulation of vibronic Hamiltonians with larger numbers of degrees of freedom

is crucial, as real molecular systems often involve many coupled vibrational modes. Increasing the number of degrees of freedom allows to capture more realistic nuclear dynamics, account for complex energy-redistribution pathways, and describe collective effects that cannot emerge in low-dimensional models. MQB architectures are continuously improving their capacity to support larger simulations. In trapped-ion systems, vibrational modes become spectrally congested as the number of ions increases [91, 293], leading to cross-talk during laser–ion interactions. Despite these limitations, current technologies have been able to spectrally resolve large ion chains and perform single-ion addressing for chains exceeding ten ions [293]. In circuit QED platforms, spatial restrictions limit the coupling of multiple resonators to a qudit system; in this case, multimode resonators could be implemented to enable medium-scale simulations [294]. These improvements offer an alternative route to extend the accessible system size.

Including simulations of chemical processes in non-Markovian environments—characterised by strong system-environment coupling and long-lived bath correlations—represents an important step towards more realistic modelling. A few approaches have been described to emulate such environments; one option is to inject correlated (coloured) classical noise [203] into the simulator, which could complement the noise-injection protocol developed in this thesis. Similarly, structured spectral densities of non-Markovian environments have already been implemented in trapped-ion architectures [82, 83], and these protocols could be adapted to mimic the environment using ancillary ions.

Our approach considers the use of native noise as a resource for simulation. By combining this with the extension of accessible modes, we expect at least the same favourable resource-scaling, compare to qubit-only simulation, as for small systems. The underlying assumption is that the usable noise engineered into the simulator remains dominant over unwanted, uncontrolled sources of noise. Nevertheless, as simulations grow in size and complexity, uncontrolled decoherence and cross-talk will inevitably accumulate. In this context, the development of error-correcting codes tailored for bosonic degrees of freedom offers a promising pathway [287, 288]. Such codes, which exploit redundancy in bosonic encodings, could help mitigate the effects of residual noise while retaining the natural resource efficiency of MQB simulators. The combination of controlled dissipation, intrinsic noise as a resource, and bosonic error correction would therefore provide a powerful toolkit for extending MQB simulations to larger and more chemically realistic systems.

Finally, the full scope of what can be simulated with MQB devices remains an open question. While this thesis has demonstrated that a variety of chemically relevant processes—such as energy transfer, vibrational relaxation, and ultrafast non-adiabatic dynamics—can already be addressed within this framework, the boundaries of its applicability are not yet fully charted. It is likely that many more processes lie within reach, but identifying and realising them will require continued theoretical and experimental exploration. At the same time, a number of central

challenges remain, including the accurate simulation of bond breaking and bond formation, strongly correlated electron–nuclear motion far from equilibrium, and long-time kinetics in complex environments. Defining and expanding this frontier will be key to broadening the ultimate potential of MQB simulation in chemistry.

Bibliography

[1] D. R. Yarkony, Rev. Mod. Phys. **68**, 985 (1996).

[2] W. Domcke, D. R. Yarkony, and H. Köppel, *Conical Intersections: Electronic Structure, Dynamics and Spectroscopy* (World Scientific Publishing, 2004).

[3] G. A. Worth and L. S. Cederbaum, Annu. Rev. Phys. Chem. **55**, 127 (2004).

[4] S. Sen, R. K. Kar, V. A. Borin, and I. Schapiro, WIREs Comput. Mol. Sci. **12**, e1562 (2022).

[5] M. A. Nielsen and I. L. Chuang, *Quantum Computation and Quantum Information: 10th Anniversary Edition* (Cambridge University Press, 2010).

[6] I. M. Georgescu, S. Ashhab, and F. Nori, Rev. Mod. Phys. **86**, 153 (2014).

[7] R. P. Feynman, Int. J. Theor. Phys. **21**, 467–488 (1982).

[8] S. Lloyd, Science **273**, 1073–1078 (1996).

[9] M. Born and R. Oppenheimer, Ann. Phys. **389**, 457 (1927).

[10] H. Köuppel, W. Domcke, and L. S. Cederbaum, Multimode molecular dynamics beyond the born-oppenheimer approximation, in *Advances in Chemical Physics* (John Wiley & Sons, Ltd, 1984) Chap. 2, pp. 59–246.

[11] R. J. MacDonell, C. E. Dickerson, C. J. T. Birch, A. Kumar, C. L. Edmunds, M. J. Biercuk, C. Hempel, and I. Kassal, Chem. Sci. **12**, 9794 (2021).

[12] G. J. Small, J. Chem. Phys. **54**, 3300 (1971).

[13] I. G. Ryabinkin, L. Joubert-Doriol, and A. F. Izmaylov, Acc. Chem. Res. **50**, 1785 (2017).

[14] I. G. Ryabinkin and A. F. Izmaylov, Phys. Rev. Lett. **111**, 220406 (2013).

[15] J. Li, L. Joubert-Doriol, and A. F. Izmaylov, J. Chem. Phys. **147**, 064106 (2017).

[16] H. P. Breuer and F. Petruccione, *The Theory of Open Quantum Systems* (Oxford University Press, 2002).

[17] A. Nitzan, *Chemical Dynamics in Condensed Phases*, 1st ed. (Oxford University Press, 2006).

[18] J. M. Jean, R. A. Friesner, and G. R. Fleming, J. Chem. Phys. **96**, 5827 (1992).

[19] U. Banin, A. Waldman, and S. Ruhman, J. Chem. Phys. **96**, 2416 (1992).

[20] U. Banin and S. Ruhman, J. Chem. Phys. **98**, 4391 (1993).

[21] U. Banin, A. Bartana, S. Ruhman, and R. Kosloff, J. Chem. Phys. **101**, 8461 (1994).

[22] I. Kassal and A. Aspuru-Guzik, New J. Phys. **14**, 053041 (2012).

[23] H.-P. Breuer, E.-M. Laine, J. Piilo, and B. Vacchini, Rev. Mod. Phys. **88**, 021002 (2016).

[24] I. de Vega and D. Alonso, Rev. Mod. Phys. **89**, 015001 (2017).

[25] J. C. Tully, Faraday Discuss. **110**, 407 (1998).

[26] A. Kirrander and M. Vacher, Ehrenfest methods for electron and nuclear dynamics, in *Quantum Chemistry and Dynamics of Excited States* (John Wiley & Sons, Ltd, 2020) Chap. 15, pp. 469–497.

[27] J. C. Tully, Chem. Phys. Lett. **816**, 140396 (2023).

[28] J. C. Tully and R. K. Preston, J. Chem. Phys. **55**, 562 (1971).

[29] M. Barbatti, WIREs Comput. Mol. Sci. **1**, 620 (2011).

[30] J. C. Tully, J. Chem. Phys. **93**, 1061 (1990).

[31] G. Worth, M. Robb, and B. Lasorne, Mol. Phys. **106**, 2077 (2008).

[32] T. J. Martinez, M. Ben-Nun, and R. D. Levine, J. Phys. Chem. **100**, 7884 (1996).

[33] M. Ben-Nun and T. J. Martinez, J. Chem. Phys. **108**, 7244 (1998).

[34] M. Feit, J. Fleck, and A. Steiger, J. Comput. Phys. **47**, 412 (1982).

[35] M. D. Feit and J. Fleck, J. A., J. Chem. Phys. **78**, 301 (1983).

[36] H. F. Trotter, Proc. Am. Math. Soc. **10**, 545 (1959).

[37] M. Suzuki, Phys. Lett. A **146**, 319 (1990).

[38] M. Suzuki, J. Math. Phys. **32**, 400 (1991).

[39] P. Duhamel and M. Vetterli, Signal Process. **19**, 259 (1990).

[40] G. A. Worth, H.-D. Meyer, H. Köppel, L. S. Cederbaum, and I. Burghardt, Int. Rev. Phys. Chem. **27**, 569 (2008).

[41] H. Wang, J. Phys. Chem. A **119**, 7951 (2008).

[42] M. Bonfanti, G. A. Worth, and I. Burghardt, in *Quantum Chemistry and Dynamics of Excited States*, edited by E. Gonzalez and R.Lindh (Wiley, 2020) pp. 383–406.

[43] H.-D. Meyer, F. Gatti, and G. A. Worth, Basic MCTDH theory, in *Multidimensional Quantum Dynamics* (John Wiley & Sons, Ltd, 2009) Chap. 3, pp. 17–30.

[44] G. A. Worth, H.-D. Meyer, and L. S. Cederbaum, J. Chem. Phys. **109**, 3518 (1998).

[45] G. Worth, H.-D. Meyer, and L. Cederbaum, Chem. Phys. Lett. **299**, 451 (1999).

[46] A. Raab, G. A. Worth, H.-D. Meyer, and L. S. Cederbaum, J. Chem. Phys. **110**, 936 (1999).

[47] H. Erik Donovan, Multi-configurational density functional theory: Progress and challenges, in *Quantum Chemistry and Dynamics of Excited States* (John Wiley & Sons, Ltd, 2020) Chap. 3, pp. 47–75.

[48] Q. Meng and H.-D. Meyer, J. Chem. Phys. **138**, 014313 (2013).

[49] Y. Xie, J. Zheng, and Z. Lan, J. Chem. Phys. **142**, 084706 (2015).

[50] I. Buluta and F. Nori, Science **326**, 108 (2009).

[51] J. I. Cirac and P. Zoller, Phys. Rev. Lett. **74**, 4091 (1995).

[52] F. Arute, K. Arya, and R. Babbush *et al.*, Nature **574**, 505 (2019).

[53] B. P. Lanyon, J. D. Whitfield, G. G. Gillett, M. E. Goggin, M. P. Almeida, I. Kassal, J. D. Biamonte, M. Mohseni, B. J. Powell, M. Barbieri, A. Aspuru-Guzik, and A. G. White, Nat. Chem. **2**, 106–111 (2010).

[54] A. Aspuru-Guzik, A. D. Dutoi, P. J. Love, and M. Head-Gordon, Science **309**, 1704–1707 (2005).

[55] A. Peruzzo, J. McClean, P. Shadbolt, M.-H. Yung, X.-Q. Zhou, P. J. Love, A. Aspuru-Guzik, and J. L. O'Brien, Nat. Comm. **5**, 1 (2014).

[56] C. Hempel, C. Maier, J. Romero, J. McClean, T. Monz, H. Shen, P. Jurcevic, B. P. Lanyon, P. Love, R. Babbush, A. Aspuru-Guzik, R. Blatt, and C. F. Roos, Phys. Rev. X **8**, 3 (2018).

[57] A. Kandala, A. Mezzacapo, K. Temme, M. Takita, M. Brink, J. M. Chow, and J. M. Gambetta, Nature **549**, 242–246 (2017).

[58] J. I. Colless, V. V. Ramasesh, D. Dahlen, M. S. Blok, M. E. Kimchi-Schwartz, J. R. McClean, J. Carter, W. A. de Jong, and I. Siddiqi, Phys. Rev. X **8**, 011021 (2018).

[59] J. Robledo-Moreno, M. Motta, H. Haas, A. Javadi-Abhari, P. Jurcevic, W. Kirby, S. Martiel, K. Sharma, S. Sharma, T. Shirakawa, I. Sitdikov, R.-Y. Sun, K. J. Sung, M. Takita, M. C. Tran, S. Yunoki, and A. Mezzacapo, Sci. Adv. **11**, eadu9991 (2025).

[60] Y. Cao, J. Romero, J. P. Olson, M. Degroote, P. D. Johnson, M. Kieferová, I. D. Kivlichan, T. Menke, B. Peropadre, N. P. D. Sawaya, S. Sim, L. Veis, and A. Aspuru-Guzik, Chem. Rev. **119**, 10856–10915 (2019).

[61] I. Kassal, S. P. Jordan, P. J. Love, M. Mohseni, and A. Aspuru-Guzik, Proc. Natl. Acad. Sci. **105**, 18681 (2008).

[62] N. P. D. Sawaya, T. Menke, T. H. Kyaw, S. Johri, A. Aspuru-Guzik, and G. G. Guerreschi, npj Quantum Inf. **6**, 49 (2020).

[63] P. J. Ollitrault, G. Mazzola, and I. Tavernelli, Phys. Rev. Lett. **125**, 26 (2020).

[64] P. J. Ollitrault, A. Miessen, and I. Tavernelli, Acc. Chem. Res. **54**, 4229 (2021).

[65] F. H. da Jornada, M. Lostaglio, S. Pallister, B. Şahinoğlu, and K. I. Seetharam, A comprehensive framework to simulate real-time chemical dynamics on a fault-tolerant quantum computer (2025), arXiv:2504.06348 .

[66] D. Motlagh, R. A. Lang, P. Jain, J. A. Campos-Gonzalez-Angulo, W. Maxwell, T. Zeng, A. Aspuru-Guzik, and J. M. Arrazola, Quantum Sci. Technol. 10.1088/2058-9565/ae0828 (2025).

[67] A. G. Fowler, M. Mariantoni, J. M. Martinis, and A. N. Cleland, Phys. Rev. A **86**, 032324 (2012).

[68] A. Katabarwa, K. Gratsea, A. Caesura, and P. D. Johnson, PRX Quantum **5**, 020101 (2024).

[69] J. D. Weidman, M. Sajjan, C. Mikolas, Z. J. Stewart, J. Pollanen, S. Kais, and A. K. Wilson, Cell Rep. Phys. Sci. **5**, 102105 (2024).

[70] R. Blatt and C. F. Roos, Nat. Phys. **8**, 277 (2012).

[71] A. Aspuru-Guzik and P. Walther, Nat. Phys. **8**, 285 (2012).

[72] I. Bloch, J. Dalibard, and S. Nascimbène, Nat. Phys. **8**, 267 (2012).

[73] J. W. Britton, B. C. Sawyer, A. C. Keith, C.-C. J. Wang, J. K. Freericks, H. Uys, M. J. Biercuk, and J. J. Bollinger, Nature **484**, 489 (2012).

[74] J. Zhang, G. Pagano, P. W. Hess, A. Kyprianidis, P. Becker, H. Kaplan, A. V. Gorshkov, Z.-X. Gong, and C. Monroe, Nature **551**, 601 (2017).

[75] J. Argüello-Luengo, A. González-Tudela, T. Shi, P. Zoller, and J. I. Cirac, Nature **574**, 215 (2019).

[76] C. Sparrow, E. Martín-López, N. Maraviglia, A. Neville, C. Harrold, J. Carolan, Y. N. Joglekar, T. Hashimoto, N. Matsuda, J. L. O'Brien, D. P. Tew, and A. Laing, Nature **557**, 660 (2018).

[77] W. Chen, J. Gan, J.-N. Zhang, D. Matuskevich, and K. Kim, Chinese Phys. B **30**, 060311 (2021).

[78] J. Huh, G. G. Guerreschi, B. Peropadre, J. R. McClean, and A. Aspuru-Guzik, Nat. Photon. **9**, 615 (2015).

[79] C. S. Wang, J. C. Curtis, B. J. Lester, Y. Zhang, Y. Y. Gao, J. Freeze, V. S. Batista, P. H. Vaccaro, I. L. Chuang, L. Frunzio, L. Jiang, S. M. Girvin, and R. J. Schoelkopf, Phys. Rev. X **10**, 2 (2020).

[80] H. Jnane, N. P. D. Sawaya, B. Peropadre, A. Aspuru-Guzik, R. Garcia-Patron, and J. Huh, ACS Photonics **8**, 2007 (2021).

[81] G.-X. Wang, Y.-K. Wu, R. Yao, W.-Q. Lian, Z.-J. Cheng, Y.-L. Xu, C. Zhang, Y. Jiang, Y.-Z. Xu, B.-X. Qi, P.-Y. Hou, Z.-C. Zhou, L. He, and L.-M. Duan, Phys. Rev. A **109**, 062402 (2024).

[82] V. So, M. D. Suganthi, A. Menon, M. Zhu, R. Zhuravel, H. Pu, P. G. Wolynes, J. N. Onuchic, and G. Pagano, Sci. Adv. **10**, eads8011 (2024).

[83] K. Sun, M. Kang, H. Nuomin, G. Schwartz, D. N. Beratan, K. R. Brown, and J. Kim, Nat. Commun. **16**, 4042 (2025).

[84] A. Blais, R.-S. Huang, A. Wallraff, S. M. Girvin, and R. J. Schoelkopf, Phys. Rev. A **69**, 062320 (2004).

[85] A. Blais, S. M. Girvin, and W. D. Oliver, Nat. Phys. **16**, 247 (2020).

[86] A. Blais, A. L. Grimsmo, S. M. Girvin, and A. Wallraff, Rev. Mod. Phys. **93**, 025005 (2021).

[87] D. Leibfried, D. M. Meekhof, C. Monroe, B. E. King, W. M. Itano, and D. J. Wineland, J. Mod. Opt. **44**, 2485 (1997).

[88] D. J. Wineland, C. Monroe, W. M. Itano, D. Leibfried, B. E. King, and D. M. Meekhof, J. Res. Natl. Inst. Stand. Technol. **103**, 259 (1998).

[89] K. Mølmer and A. Sørensen, Phys. Rev. Lett. **82**, 1835–1838 (1999).

[90] D. Leibfried, R. Blatt, C. Monroe, and D. Wineland, Rev. Mod. Phys. **75**, 281 (2003).

[91] P. J. Lee, K.-A. Brickman, L. Deslauriers, P. C. Haljan, L.-M. Duan, and C. Monroe, J. Opt. B: Quantum Semiclass. Opt. **7**, S371 (2005).

[92] B. B. Blinov, D. Leibfried, C. Monroe, and D. J. Wineland, Quantum Inf. Process. **3**, 45 (2004).

[93] T. Ruster, C. T. Schmiegelow, H. Kaufmann, C. Warschburger, F. Schmidt-Kaler, and U. G. Poschinger, Appl. Phys. B **122**, 254 (2016).

[94] D. M. Lucas, B. C. Keitch, J. P. Home, G. Imreh, M. J. McDonnell, D. N. Stacey, D. J. Szwer, and A. M. Steane, A long-lived memory qubit on a low-decoherence quantum bus (2007), arXiv:0710.4421 .

[95] D. T. C. Allcock, W. C. Campbell, J. Chiaverini, I. L. Chuang, E. R. Hudson, I. D. Moore, A. Ransford, C. Roman, J. M. Sage, and D. J. Wineland, Appl. Phys. Lett. **119**, 214002 (2021).

[96] D. Leibfried, C. Roos, P. Barton, H. Rohde, S. Gulde, A. B. Mundt, G. Reymond, M. Lederbauer, F. Schmidt-Kaler, J. Eschner, and R. Blatt, AIP Conf. Proc. **551**, 130 (2001).

[97] P. A. Barton, C. J. S. Donald, D. M. Lucas, D. A. Stevens, A. M. Steane, and D. N. Stacey, Phys. Rev. A **62**, 032503 (2000).

[98] G. Breit and I. I. Rabi, Phys. Rev. **38**, 2082 (1931).

[99] V. G. Matsos, C. H. Valahu, M. J. Millican, T. Navickas, X. C. Kolesnikow, M. J. Biercuk, and T. R. Tan, Nat. Phys. 10.1038/s41567-025-03002-8 (2025).

[100] D. Leibfried, D. M. Meekhof, B. E. King, C. Monroe, W. M. Itano, and D. J. Wineland, Phys. Rev. Lett. **77**, 4281 (1996).

[101] S. Stenholm, Rev. Mod. Phys. **58**, 699 (1986).

[102] C. N. Cohen-Tannoudji and W. D. Phillips, Phys. Today **43**, 33 (1990).

[103] J. I. Cirac, R. Blatt, P. Zoller, and W. D. Phillips, Phys. Rev. A **46**, 2668 (1992).

[104] A. Serafini, A. Retzker, and M. B. Plenio, New J. Phys. **11**, 023007 (2009).

[105] C. H. Valahu, V. C. Olaya-Agudelo, R. J. MacDonell, T. Navickas, A. D. Rao, M. J. Millican, J. B. Pérez-Sánchez, J. Yuen-Zhou, M. J. Biercuk, C. Hempel, T. R. Tan, and I. Kassal, Nat. Chem. **15**, 1503 (2023).

[106] R. J. MacDonell, T. Navickas, T. F. Wohlers-Reichel, C. H. Valahu, A. D. Rao, M. J. Millican, M. A. Currington, M. J. Biercuk, T. R. Tan, C. Hempel, and I. Kassal, Chem. Sci. **14**, 9439 (2023).

[107] J. Whitlow, Z. Jia, Y. Wang, C. Fang, J. Kim, and K. R. Brown, Nat. Chem. **15**, 1509 (2023).

[108] C. F. Roos, New J. Phys. **10**, 013002 (2008).

[109] G. Kirchmair, J. Benhelm, F. Zähringer, R. Gerritsma, C. F. Roos, and R. Blatt, New J. Phys. **11**, 023002 (2009).

[110] J. Larson, E. Sjöqvist, and P. Öhberg, *Conical Intersections in Physics* (Springer Cham, 2020).

[111] W. Domcke and D. R. Yarkony, Annu. Rev. Phys. Chem. **63**, 325 (2012).

[112] M. V. Berry, Proc. R. Soc. Lond. A **392**, 47 (1984).

[113] H. C. Longuet-Higgins, U. Öpik, M. H. L. Pryce, and R. A. Sack, Proc. R. Soc. Lond. A **244**, 1 (1958).

[114] C. A. Mead and D. G. Truhlar, J. Chem. Phys. **70**, 2284 (1979).

[115] J. Schön and H. Köppel, J. Chem. Phys. **103**, 9292 (1995).

[116] C. A. Mead, J. Chem. Phys. **72**, 3839 (1980).

[117] B. Lepetit and A. Kuppermann, Chem. Phys. Lett. **166**, 581 (1990).

[118] S. C. Althorpe, J. Chem. Phys. **124**, 084105 (2006).

[119] S. C. Althorpe, T. Stecher, and F. Bouakline, J. Chem. Phys. **129**, 214117 (2008).

[120] B. Kendrick, Phys. Rev. Lett. **79**, 2431 (1997).

[121] B. E. Applegate, T. A. Barckholtz, and T. A. Miller, Chem. Soc. Rev. **32**, 38 (2003).

[122] R. Englman, J. Chem. Phys. **144**, 024103 (2016).

[123] D. Yuan, Y. Guan, W. Chen, H. Zhao, S. Yu, C. Luo, Y. Tan, T. Xie, X. Wang, Z. Sun, D. H. Zhang, and X. Yang, Science **362**, 1289 (2018).

[124] D. Yuan, Y. Huang, W. Chen, H. Zhao, S. Yu, C. Luo, Y. Tan, S. Wang, X. Wang, Z. Sun, and X. Yang, Nat. Commun. **11**, 3640 (2020).

[125] J. A. Cina and V. Romero-Rochin, J. Chem. Phys. **93**, 3844 (1990).

[126] J. A. Cina, Phys. Rev. Lett. **66**, 1146 (1991).

[127] J. A. Cina, J. T. J. Smith, and V. Romero-Rochin, Adv. in Chem. Phys. **83**, 1 (1993).

[128] A. H. Castro Neto, F. Guinea, N. M. R. Peres, K. S. Novoselov, and A. K. Geim, Rev. Mod. Phys. **81**, 109 (2009).

[129] Y. Ran, F. Wang, H. Zhai, A. Vishwanath, and D.-H. Lee, Phys. Rev. B **79**, 014505 (2009).

[130] E. Rashba, Sov. Phys.-Solid State **1**, 368 (1959).

[131] G. Dresselhaus, Phys. Rev. **100**, 580 (1955).

[132] J. A. Cina, Annu. Rev. Phys. Chem. **59**, 319 (2008).

[133] R. Blatt and C. F. Roos, Nat. Phys. **8**, 277 (2012).

[134] S. McArdle, S. Endo, A. Aspuru-Guzik, S. C. Benjamin, and X. Yuan, Rev. Mod. Phys. **92**, 015003 (2020).

[135] J. D. Gorman, B. Hemmerling, E. Megidish, S. A. Moeller, P. Schindler, M. Sarovar, and H. Haeffner, Phys. Rev. X **8**, 011038 (2018).

[136] L. Duca, T. Li, M. Reitter, I. Bloch, M. Schleier-Smith, and U. Schneider, Science **347**, 288 (2015).

[137] C. D. Brown, S.-W. Chang, M. N. Schwarz, T.-H. Leung, V. Kozii, A. Avdoshkin, J. E. Moore, and D. Stamper-Kurn, Science **377**, 1319 (2022).

[138] F. M. Gambetta, C. Zhang, M. Hennrich, I. Lesanovsky, and W. Li, Phys. Rev. Lett. **126**, 233404 (2021).

[139] T. Dereli, Y. Gül, P. Forn-Díaz, and O. E. Müstecaplıoğlu, Phys. Rev. A **85**, 053841 (2012).

[140] J. Larson, Phys. Rev. A **78**, 033833 (2008).

[141] C. S. Wang, N. E. Frattini, B. J. Chapman, S. Puri, S. M. Girvin, M. H. Devoret, and R. J. Schoelkopf, Phys. Rev. X **13**, 011008 (2023).

[142] I. B. Bersuker, Chem. Rev. **101**, 1067 (2001).

[143] C. Monroe, D. M. Meekhof, B. E. King, and D. J. Wineland, Science **272**, 1131 (1996).

[144] J. Mizrahi, B. Neyenhuis, K. G. Johnson, W. C. Campbell, C. Senko, D. Hayes, and C. Monroe, Appl. Phys. B **114**, 45 (2013).

[145] R. Gerritsma, G. Kirchmair, F. Zähringer, E. Solano, R. Blatt, and C. F. Roos, Nature **463**, 68 (2010).

[146] K. G. Johnson, B. Neyenhuis, J. Mizrahi, J. D. Wong-Campos, and C. Monroe, Phys. Rev. Lett. **115**, 213001 (2015).

[147] C. Flühmann and J. P. Home, Phys. Rev. Lett. **125**, 043602 (2020).

[148] Z. Jia, Y. Wang, B. Zhang, J. Whitlow, C. Fang, J. Kim, and K. R. Brown, Phys. Rev. Lett. **129**, 103602 (2022).

[149] D. Hayes, S. T. Flammia, and M. J. Biercuk, New J. Phys. **16**, 083027 (2014).

[150] M. Brownnutt, M. Kumph, P. Rabl, and R. Blatt, Rev. Mod. Phys. **87**, 1419 (2015).

[151] D. Kienzler, C. Flühmann, V. Negnevitsky, H.-Y. Lo, M. Marinelli, D. Nadlinger, and J. P. Home, Phys. Rev. Lett. **116**, 140402 (2016).

[152] C. Monroe, D. M. Meekhof, B. E. King, S. R. Jefferts, W. M. Itano, D. J. Wineland, and P. Gould, Phys. Rev. Lett. **75**, 4011 (1995).

[153] L. Riesebos, B. Bondurant, and K. R. Brown, IEEE Micro **41**, 5 (2021).

[154] A. Kühl and W. Domcke, J. Chem. Phys. **116**, 263 (2002).

[155] G. Katz, R. Kosloff, and M. A. Ratner, Isr. J. Chem. **44**, 53 (2004).

[156] D. Gelman, G. Katz, R. Kosloff, and M. A. Ratner, J. Chem. Phys. **123**, 134112 (2005).

[157] L. Chen, M. F. Gelin, V. Y. Chernyak, W. Domcke, and Y. Zhao, Faraday Discuss. **194**, 61 (2016).

[158] H.-G. Duan and M. Thorwart, J. Phys. Chem. Lett. **7**, 382 (2016).

[159] A. Miessen, P. J. Ollitrault, and I. Tavernelli, Phys. Rev. Res. **3**, 043212 (2021).

[160] J. Lee, D. W. Berry, C. Gidney, W. J. Huggins, J. R. McClean, N. Wiebe, and R. Babbush, PRX Quantum **2**, 030305 (2021).

[161] A. Miessen, P. J. Ollitrault, F. Tacchino, and I. Tavernelli, Nat. Comput. Sci. **3**, 25 (2023).

[162] H. Wang, S. Ashhab, and F. Nori, Phys. Rev. A **83**, 062317 (2011).

[163] R. Sweke, I. Sinayskiy, D. Bernard, and F. Petruccione, Phys. Rev. A **91**, 062308 (2015).

[164] S.-J. Wei, D. Ruan, and G.-L. Long, Sci. Rep. **6**, 30727 (2016).

[165] A. W. Schlimgen, K. Head-Marsden, L. M. Sager, P. Narang, and D. A. Mazziotti, Phys. Rev. Lett. **127**, 270503 (2021).

[166] C. H. Tseng, S. Somaroo, Y. Sharf, E. Knill, R. Laflamme, T. F. Havel, and D. G. Cory, Phys. Rev. A **62**, 032309 (2000).

[167] J. D. Guimarães, J. Lim, M. I. Vasilevskiy, S. F. Huelga, and M. B. Plenio, PRX Quantum **4**, 040329 (2023).

[168] J. Leppäkangas, N. Vogt, K. R. Fratus, K. Bark, J. A. Vaitkus, P. Stadler, J.-M. Reiner, S. Zanker, and M. Marthaler, Phys. Rev. A **108**, 062424 (2023).

[169] P. Stadler, M. Lodi, A. Khedri, R. Reiner, K. Bark, N. Vogt, M. Marthaler, and J. Leppäkangas, Phys. Rev. A **111**, 022614 (2025).

[170] C. S. Wang, N. E. Frattini, B. J. Chapman, S. Puri, S. M. Girvin, M. H. Devoret, and R. J. Schoelkopf, Phys. Rev. X **13**, 011008 (2023).

[171] S. Mostame, P. Rebentrost, A. Eisfeld, A. J. Kerman, D. I. Tsomokos, and A. Aspuru-Guzik, New J. Phys. **14**, 105013 (2012).

[172] A. Lemmer, C. Cormick, D. Tamascelli, T. Schaetz, S. F. Huelga, and M. B. Plenio, New J. Phys. **20**, 073002 (2018).

[173] C. W. Kim, J. M. Nichol, A. N. Jordan, and I. Franco, PRX Quantum **3**, 040308 (2022).

[174] D. J. Gorman, B. Hemmerling, E. Megidish, S. A. Moeller, P. Schindler, M. Sarovar, and H. Haeffner, Phys. Rev. X **8**, 011038 (2018).

[175] V. May and O. Kühn, *Charge and energy transfer dynamics in molecular systems*, 3rd ed. (Wiley-VCH, 2011).

[176] G. Lindblad, Commun. Math. Phys. **48**, 119 (1976).

[177] I. Talukdar, D. J. Gorman, N. Daniilidis, P. Schindler, S. Ebadi, H. Kaufmann, T. Zhang, and H. Häffner, Phys. Rev. A **93**, 043415 (2016).

[178] V. Jarlaud, P. Hrmo, M. K. Joshi, and R. C. Thompson, J. Phys. B: At. Mol. Opt. Phys. **54**, 015501 (2020).

[179] R. Schneider, W. Domcke, and H. Köppel, J. Chem. Phys. **92**, 1045 (1990).

[180] R. Schneider and W. Domcke, Chem. Phys. Lett. **159**, 61 (1989).

[181] G. Stock and W. Domcke, J. Chem. Phys. **93**, 5496 (1990).

[182] D. Leibfried, B. DeMarco, V. Meyer, D. Lucas, M. Barrett, J. Britton, W. M. Itano, B. Jelenković, C. Langer, T. Rosenband, and D. J. Wineland, Nature **422**, 412 (2003).

[183] C. J. Ballance, T. P. Harty, N. M. Linke, M. A. Sepiol, and D. M. Lucas, Phys. Rev. Lett. **117**, 060504 (2016).

[184] A. Kastler, J. Phys. Radium **11**, 255 (1950).

[185] J. T. Barreiro, M. Müller, P. Schindler, D. Nigg, T. Monz, M. Chwalla, M. Hennrich, C. F. Roos, P. Zoller, and R. Blatt, Nature **470**, 486–491 (2011).

[186] W. Itano, J. Bergquist, J. Bollinger, J. Gilligan, D. Heinzen, F. Moore, M. Raizen, and D. Wineland, Vistas Astron. **37**, 169 (1993).

[187] I. Marzoli, J. I. Cirac, R. Blatt, and P. Zoller, Phys. Rev. A **49**, 2771 (1994).

[188] A. J. Rasmusson, I. Jung, F. G. Schroer, A. Kyprianidis, and P. Richerme, J. Phys. B: At. Mol. Opt. Phys. **57**, 225002 (2024).

[189] C. Hempel, *PhD thesis: Digital quantum simulation, Schrödinger cat state spectroscopy and setting up a linear ion trap* (Leopold-Franzens University of Innsbruck, 2014).

[190] C. D. Bruzewicz, J. M. Sage, and J. Chiaverini, Phys. Rev. A **91**, 041402 (2015).

[191] Q. A. Turchette, Kielpinski, B. E. King, D. Leibfried, D. M. Meekhof, C. J. Myatt, M. A. Rowe, C. A. Sackett, C. S. Wood, W. M. Itano, C. Monroe, and D. J. Wineland, Phys. Rev. A **61**, 063418 (2000).

[192] D. J. Larson, J. C. Bergquist, J. J. Bollinger, W. M. Itano, and D. J. Wineland, Phys. Rev. Lett. **57**, 70 (1986).

[193] A. Chenu, M. Beau, J. Cao, and A. d. Campo, Phys. Rev. Lett. **118**, 140403 (2017).

[194] B. Gu and I. Franco, J. Chem. Phys. **151**, 0141091 (2019).

[195] J. Li, M. A. Sillanpää, G. S. Paraoanu, and P. J. Hakonen, J. Phys. Conf. Ser. **400**, 042039 (2012).

[196] J. Li, G. S. Paraoanu, K. Cicak, F. Altomare, J. I. Park, R. W. Simmonds, M. A. Sillanpää, and P. J. Hakonen, Phys. Rev. B **84**, 104527 (2011).

[197] W. Yang, W.-L. Ma, and R.-B. Liu, Rep. Prog. Phys. **80**, 016001 (2016).

[198] D. F. V. James, Appl. Phys. B **66**, 181 (1998).

[199] T. R. Tan, T. Navickas, C. Valahu, J. Jee, A. Rao, M. Millican, and M. Biercuk, in *2023 Joint Conference of the European Frequency and Time Forum and IEEE International Frequency Control Symposium (EFTF/IFCS)* (2023) pp. 1–2.

[200] E. Gershgoren, Z. Wang, S. Ruhman, J. Vala, and R. Kosloff, J. Chem. Phys. **118**, 3660 (2003).

[201] C. H. Baldwin, B. J. Bjork, M. Foss-Feig, J. P. Gaebler, D. Hayes, M. G. Kokish, C. Langer, J. A. Sedlacek, D. Stack, and G. Vittorini, Phys. Rev. A **103**, 012603 (2021).

[202] W. J. Karplus and W. W. Soroka, *Analog Methods: Computation and Simulation*, 2nd ed. (Mcgraw Hill Book Company, 1956).

[203] J. I. Costa-Filho, R. B. B. Lima, R. R. Paiva, P. M. Soares, W. A. M. Morgado, R. L. Franco, and D. O. Soares-Pinto, Phys. Rev. A **95**, 052126 (2017).

[204] L. S. Cederbaum, H. Köppel, and W. Domcke, Int. J. Quantum Chem. **20**, 251 (1981).

[205] M. D. E. Forbes, ACS Cent. Sci. **1**, 354–363 (2015).

[206] M. Bonfanti, G. F. Tantardini, K. H. Hughes, R. Martinazzo, and I. Burghardt, J. Phys. Chem. A **116**, 11406 (2012).

[207] A. V. Haeften, C. Ash, and G. Worth, J. Chem. Phys. **159**, 194114 (2023).

[208] S. McArdle, S. Endo, A. Aspuru-Guzik, S. C. Benjamin, and X. Yuan, Rev. Mod. Phys. **92**, 015003 (2020).

[209] B. Bauer, S. Bravyi, M. Motta, and G. K.-L. Chan, Chem. Rev. **120**, 12685–12717 (2020).

[210] Y. Nam, J.-S. Chen, N. C. Pisenti, K. Wright, C. Delaney, D. Maslov, K. R. Brown, S. Allen, J. M. Amini, J. Apisdorf, K. M. Beck, A. Blinov, V. Chaplin, M. Chmielewski, C. Collins, S. Debnath, K. M. Hudek, A. M. Ducore, M. Keesan, S. M. Kreikemeier,

J. Mizrahi, P. Solomon, M. Williams, J. D. Wong-Campos, D. Moehring, C. Monroe, and J. Kim, npj Quantum Inf. **6**, 1 (2020).

[211] N. P. D. Sawaya and J. Huh, J. Phys. Chem. Lett. **10**, 3586–3591 (2019).

[212] E. Crane, K. C. Smith, T. Tomesh, A. Eickbusch, J. M. Martyn, S. Kühn, L. Funcke, M. A. DeMarco, I. L. Chuang, N. Wiebe, A. Schuckert, and S. M. Girvin, Hybrid oscillator-qubit quantum processors: Simulating fermions, bosons, and gauge fields (2024), arXiv:2409.03747 .

[213] M. Kang, H. Nuomin, S. N. Chowdhury, J. L. Yuly, K. Sun, J. Whitlow, J. Valdiviezo, Z. Zhang, P. Zhang, D. N. Beratan, and K. R. Brown, Nat. Rev. Chem. **8**, 340–358 (2024).

[214] V. C. Olaya-Agudelo, B. Stewart, C. H. Valahu, R. J. MacDonell, M. J. Millican, V. G. Matsos, F. Scuccimarra, T. R. Tan, and I. Kassal, Phys. Rev. Res. **7**, 023215 (2025).

[215] Y. Shen, Y. Lu, K. Zhang, J. Zhang, S. Zhang, J. Huh, and K. Kim, Chem. Sci. **9**, 836–840 (2018).

[216] J.-K. Ha and R. J. MacDonell, Analog quantum simulation of coupled electron-nuclear dynamics in molecules (2024), arXiv:2409.04427 .

[217] C. Woywod and W. Domcke, Chem. Phys. **162**, 349 (1992).

[218] C. Cattarius, G. A. Worth, H.-D. Meyer, and L. S. Cederbaum, J. Chem. Phys. **115**, 2088 (2001).

[219] I. G. Ryabinkin, L. Joubert-Doriol, and A. F. Izmaylov, J. Chem. Phys. **140**, 214116 (2014).

[220] C. Woywod, W. Domcke, A. L. Sobolewski, and H.-J. Werner, J. Chem. Phys. **100**, 1400 (1994).

[221] A. Kühl and W. Domcke, J. Chem. Phys. **116**, 263 (2002).

[222] S. Olmschenk, K. C. Younge, D. L. Moehring, D. N. Matsukevich, P. Maunz, and C. Monroe, Phys. Rev. A **76**, 5 (2007).

[223] C. Henkel, S. Pötting, and M. Wilkens, App. Phys. B **69**, 379–387 (1999).

[224] C. H. Valahu, T. Navickas, M. J. Biercuk, and T. R. Tan, PRX Quantum **5**, 040337 (2024).

[225] P. H. Leung and K. R. Brown, Phys. Rev. A **98**, 032318 (2018).

[226] A. R. Milne, C. L. Edmunds, C. Hempel, F. Roy, S. Mavadia, and M. J. Biercuk, Phys. Rev. Appl. **13**, 024022 (2020).

[227] R. T. Sutherland and R. Srinivas, Phys. Rev. A **104**, 032609 (2021).

[228] Y. Liu, S. Singh, K. C. Smith, E. Crane, J. M. Martyn, A. Eickbusch, A. Schuckert, R. D. Li, J. Sinanan-Singh, M. B. Soley, T. Tsunoda, I. L. Chuang, N. Wiebe, and S. M. Girvin, Hybrid oscillator-qubit quantum processors: Instruction set architectures, abstract machine models, and applications (2024), arXiv:2407.10381 .

[229] F. Gatti, ed., *Molecular Quantum Dynamics: From Theory to Applications*, 1st ed. (Springer Berlin, Heidelberg, 2014).

[230] B. F. E. Curchod and A. J. Orr-Ewing, J. Phys. Chem. A. **128**, 6613 (2024).

[231] C. S. J. Ponseca, P. Chábera, J. Uhlig, P. Persson, and V. Sundström, Chem. Rev. **117**, 10940 (2017).

[232] B. F. E. Curchod and T. J. Martínez, Chem. Rev. **118**, 3305 (2018).

[233] T. R. Nelson, A. J. White, J. A. Bjorgaard, A. E. Sifain, Y. Zhang, B. Nebgen, S. Fernandez-Alberti, D. Mozyrsky, A. E. Roitberg, and S. Tretiak, Chem. Rev. **120**, 2215 (2020).

[234] L. L. E. Cigrang, B. F. E. Curchod, R. A. Ingle, A. Kelly, J. R. Mannouch, D. Accomasso, A. Alijah, M. Barbatti, W. Chebbi, N. Došlić, E. C. Eklund, S. Fernandez-Alberti, A. Freibert, L. González, G. Granucci, F. J. Hernández, J. Hernández-Rodríguez, A. Jain, J. Janoš, I. Kassal, A. Kirrander, Z. Lan, H. R. Larsson, D. Lauvergnat, B. Le Dé, Y. Lee, N. T. Maitra, S. K. Min, D. Peláez, D. Picconi, Z. Qiu, U. Raucci, P. Robertson, E. Sangiogo Gil, M. Sapunar, P. Schürger, P. Sinnott, S. Tretiak, A. Tikku, P. Vindel-Zandbergen, G. A. Worth, F. Agostini, S. Gómez, L. M. Ibele, and A. Prlj, J. Phys. Chem. A. **129**, 7023 (2025).

[235] R. Crespo-Otero and M. Barbatti, Chem. Rev. **118**, 7026 (2018).

[236] T. Navickas, R. J. MacDonell, C. H. Valahu, V. C. Olaya-Agudelo, F. Scuccimarra, M. J. Millican, V. G. Matsos, H. L. Nourse, A. D. Rao, M. J. Biercuk, C. Hempel, I. Kassal, and T. R. Tan, JACS **147**, 23566 (2025).

[237] A. M. Childs and T. Li, Quantum Inf. Comput. **17**, 10.26421/qic17.11-12 (2017).

[238] R. Cleve and C. Wang, Efficient quantum algorithms for simulating Lindblad evolution (2016), arXiv:1612.09512 .

[239] X. Li and C. Wang, in *50th International Colloquium on Automata, Languages, and Programming (ICALP 2023)*, Vol. 261 (Schloss Dagstuhl – Leibniz-Zentrum für Informatik, Dagstuhl, Germany, 2023).

[240] N. Suri, J. Barreto, S. Hadfield, N. Wiebe, F. Wudarski, and J. Marshall, Quantum **7**, 1002 (2023).

[241] Z. Ding, X. Li, and L. Lin, PRX Quantum **5**, 020332 (2024).

[242] M. Pocrnic, D. Segal, and N. Wiebe, J. Phys. A: Math. Theor. **58**, 305302 (2025).

[243] Z. Davoudi, N. M. Linke, and G. Pagano, Phys. Rev. Res. **3**, 043072 (2021).

[244] E. Crane, K. C. Smith, T. Tomesh, A. Eickbusch, J. M. Martyn, S. Kühn, L. Funcke, M. A. DeMarco, I. L. Chuang, N. Wiebe, A. Schuckert, and S. M. Girvin, Hybrid oscillator-qubit quantum processors: Simulating fermions, bosons, and gauge fields (2024), arXiv:2409.03747 .

[245] S. Kumar, N. N. Hegade, A.-M. Visuri, B. A. Bhargava, J. F. R. Hernandez, E. Solano, F. Albarrán-Arriagada, and G. A. Barrios, npj Quantum Inf. **11**, 43 (2025).

[246] E. Chiari, W. Makhlouf, L. Pepe, E. Koridon, J. Klein, B. Senjean, B. Lasorne, and S. Yalouz, Phys. Rev. A **112**, 052433 (2025).

[247] N. Moll, P. Barkoutsos, L. S. Bishop, J. M. Chow, A. Cross, D. J. Egger, S. Filipp, A. Fuhrer, J. M. Gambetta, M. Ganzhorn, A. Kandala, A. Mezzacapo, P. Müller, W. Riess, G. Salis, J. Smolin, I. Tavernelli, and K. Temme, Quantum Sci. Technol. **3**, 030503 (2018).

[248] A. W. Cross, L. S. Bishop, S. Sheldon, P. D. Nation, and J. M. Gambetta, Phys. Rev. A **100**, 032328 (2019).

[249] R. Blume-Kohout and K. C. Young, Quantum **4**, 362 (2020).

[250] C. H. Baldwin, K. Mayer, N. C. Brown, C. Ryan-Anderson, and D. Hayes, Quantum **6**, 707 (2022).

[251] D. A. Lidar and T. A. Brun, eds., *Quantum Error Correction* (Cambridge University Press, 2013).

[252] B. M. Terhal, Rev. Mod. Phys. **87**, 307 (2015).

[253] S. M. Girvin, SciPost Phys. Lect. Notes , 70 (2023).

[254] V. V. Albert and P. Faist, The Error Correction Zoo (2025).

[255] G. C. Schatz and M. A. Ratner, *Quantum Mechanics in Chemistry*, Dover Books on Chemistry (Dover Publications, Mineola, NY, 2002).

[256] D. Leibfried, B. DeMarco, V. Meyer, D. Lucas, M. Barrett, J. Britton, W. M. Itano, B. Jelenković, C. Langer, T. Rosenband, and D. J. Wineland, Nature **422**, 412 (2003).

[257] B. Mischuck and K. Mølmer, Phys. Rev. A **87**, 022341 (2013).

[258] S. Krastanov, V. V. Albert, C. Shen, C.-L. Zou, R. W. Heeres, B. Vlastakis, R. J. Schoelkopf, and L. Jiang, Phys. Rev. A **92**, 040303 (2015).

[259] Y. Liu, J. Sinanan-Singh, M. T. Kearney, G. Mintzer, and I. L. Chuang, Phys. Rev. A **104**, 032605 (2021).

[260] A. Eickbusch, V. Sivak, A. Z. Ding, S. S. Elder, S. R. Jha, J. Venkatraman, B. Royer, S. M. Girvin, R. J. Schoelkopf, and M. H. Devoret, Nat. Phys. **18**, 1464 (2022).

[261] N. Schlosser, G. Reymond, I. Protsenko, and P. Grangier, Nature **411**, 1024 (2001).

[262] Y. R. P. Sortais, H. Marion, C. Tuchendler, A. M. Lance, M. Lamare, P. Fournet, C. Armellin, R. Mercier, G. Messin, A. Browaeys, and P. Grangier, Phys. Rev. A **75**, 013406 (2007).

[263] A. M. Kaufman, B. J. Lester, and C. A. Regal, Phys. Rev. X **2**, 041014 (2012).

[264] A. L. Shaw, P. Scholl, R. Finkelstein, R. B.-S. Tsai, J. Choi, and M. Endres, Science **388**, 845 (2025).

[265] K. Park, P. Marek, and R. Filip, New J. Phys. **20**, 053022 (2018).

[266] K. Park and R. Filip, Npj Quantum Inf. **10**, 25 (2024).

[267] A. C. C. de Albornoz, R. G. C. nas, M. Schäfer, N. E. Frattini, B. Allen, D. G. A. Cabral, P. E. Videla, P. Khazaei, E. Geva, V. S. Batista, and M. H. Devoret, Oscillatory dissipative tunneling in an asymmetric double-well potential (2024), arXiv:2409.13113 .

[268] T. Chalermpusitarak, K. Schwennicke, I. Kassal, and T. R. Tan, Programmable generation of arbitrary continuous-variable anharmonicities and nonlinear couplings (2025), arXiv:2511.22286 .

[269] G. H. Low and I. L. Chuang, Quantum **3**, 163 (2019).

[270] A. Gilyén, Y. Su, G. H. Low, and N. Wiebe, in *Proceedings of the 51st Annual ACM SIGACT Symposium on Theory of Computing*, STOC 2019 (Association for Computing Machinery, New York, NY, USA, 2019) p. 193–204.

[271] J. M. Martyn, Z. M. Rossi, A. K. Tan, and I. L. Chuang, PRX Quantum **2**, 040203 (2021).

[272] A. M. Childs, Y. Su, M. C. Tran, N. Wiebe, and S. Zhu, Phys. Rev. X **11**, 011020 (2021).

[273] A. M. Childs and Y. Su, Phys. Rev. Lett. **123**, 050503 (2019).

[274] J. L. Bosse, A. M. Childs, C. Derby, F. M. Gambetta, A. Montanaro, and R. A. Santos, Nat. Commun. **16**, 2673 (2025).

[275] A. M. Childs, D. Maslov, Y. Nam, N. J. Ross, and Y. Su, Proc. Natl. Acad. Sci. U.S.A. **115**, 9456 (2018).

[276] M. E. S. Morales, P. C. S. Costa, G. Pantaleoni, D. K. Burgarth, Y. R. Sanders, and D. W. Berry, Quantum Inf. Comput. **25**, 1–35 (2025).

[277] A. Cowtan, S. Dilkes, R. Duncan, W. Simmons, and S. Sivarajah, Electron. Proc. Theor. Comput. Sci. **318**, 213–228 (2020).

[278] J. van de Wetering, New J. Phys. **23**, 043015 (2021).

[279] E. Bäumer and S. Woerner, Phys. Rev. Res. **7**, 023120 (2025).

[280] L. Seidner, G. Stock, A. L. Sobolewski, and W. Domcke, J. Chem. Phys. **96**, 5298 (1992).

[281] P. Hauke, F. M. Cucchietti, L. Tagliacozzo, I. Deutsch, and M. Lewenstein, Rep. Prog. Phys. **75**, 082401 (2012).

[282] M. Sarovar, J. Zhang, and L. Zeng, EPJ Quantum Technol. **4**, 1 (2017).

[283] M. Heyl, P. Hauke, and P. Zoller, Sci. Adv. **5**, eaau8342 (2019).

[284] R. Trivedi, A. Franco Rubio, and J. I. Cirac, Nat. Commun. **15**, 6507 (2024).

[285] V. Kashyap, G. Styliaris, S. Mouradian, J. I. Cirac, and R. Trivedi, Phys. Rev. X **15**, 021017 (2025).

[286] D. Litinski, Quantum **3**, 205 (2019).

[287] W. Cai, Y. Ma, W. Wang, C.-L. Zou, and L. Sun, Fundam. Res. **1**, 50 (2021).

[288] A. J. Brady, A. Eickbusch, S. Singh, J. Wu, and Q. Zhuang, Prog. Quantum Electron. **93**, 100496 (2024).

[289] N. Lambert, E. Giguère, P. Menczel, B. Li, P. Hopf, G. Suárez, M. Gali, J. Lishman, R. Gadhvi, R. Agarwal, A. Galicia, N. Shammah, P. Nation, J. R. Johansson, S. Ahmed, S. Cross, A. Pitchford, and F. Nori, QuTiP 5: The Quantum Toolbox in Python (2024), arXiv:2412.04705 .

[290] C. Developers, *Cirq* (Zenodo, 2025).

[291] P. M. Krasilnikov, Biophys. **59**, 189 (2014).

[292] L. Slocombe, M. Sacchi, and J. Al-Khalili, Commun. Phys. **5**, 109 (2022).

[293] N. Friis, O. Marty, C. Maier, C. Hempel, M. Holzäpfel, P. Jurcevic, M. B. Plenio, M. Huber, C. Roos, R. Blatt, and B. Lanyon, Phys. Rev. X **8**, 021012 (2018).

[294] N. M. Sundaresan, Y. Liu, D. Sadri, L. J. Szőcs, D. L. Underwood, M. Malekakhlagh, H. E. Türeci, and A. A. Houck, Phys. Rev. X **5**, 021035 (2015).